Managing Coastal Aquifers in Selected Pacific SIDS

Amir Jazayeri, Adrian D. Werner, Peter Sinclair, Andreas Antoniou and Mary Hingst

Flinders University
NATIONAL CENTRE FOR GROUNDWATER RESEARCH AND TRAINING
Pacific Community
Communauté du Pacifique
UNDP
gef

January 2024

Managing Coastal Aquifers in Selected Pacific SIDS

Amir Jazayeri[1]
Adrian D. Werner[1]
Peter Sinclair[2]
Andreas Antoniou[2]
Mary Hingst[2]

[1]Flinders University
[2]Pacific Community (SPC)

JANUARY 2024

Front cover photo: Infiltration gallery construction at Padua Senior Secondary School – Kiritimati Atoll (Kiribati), 2022; Photo by: Ioannatu Tiriata (WSD Sanitation Superintendent)

Executive Summary

The lenses of atoll islands are the primary source of freshwater for numerous communities within Small Island Developing States (SIDS). Extracting freshwater from atoll lenses requires specialised techniques because the lenses are thin, and seawater is easily drawn into traditional, vertical pumping wells. Although various methods of groundwater pumping are employed on atoll islands, infiltration galleries, also known as "skimming wells", have proven to be the most effective in supplying larger populations. Infiltration galleries enable the distribution of pumping over a broader area, thereby helping to mitigate saltwater ingress into pumping wells. They are used on several Pacific atoll islands, including Bonriki, Buota and Kiritimati Islands (Kiribati), Kwajalein Island (Marshall Islands), and Lifuka Island (Tonga).

Infiltration galleries consist of perforated (slotted) pipe placed horizontally within an excavated trench. The pipe is surrounded by a gravel pack to exclude fine material from clogging the well screen and entering well, and to enhance the connection between the pipe and the aquifer. The gravel pack may or may not be surrounded by a geofabric to separate gravel packs from the finer, parent sediment. A plastic liner may also be placed above the gravel pack to separate the overlying fine material from the gravel pack. On Aitutaki Island (Cook Islands), EcoBloc prefabricated modules have been installed instead of traditional slotted pipe to avoid the need for gravel, which is challenging to source on many atoll islands. Horizontal conduits (or rectangular-prism EcoBloc modules) can be laid in straight lines or as branched networks. Each gallery is connected to one or two collector wells from which the groundwater is extracted.

The design of existing infiltration galleries has primarily depended on fairly rudimentary calculations and insights derived from past endeavours rather than systematic analysis using numerical modelling that captures the main controlling factors. The present study is the first attempt to examine the key design elements of infiltration galleries, evaluating the hydraulics and influence of individual components on performance (i.e., the allowable pumping rate and the salinity of extracted water) of the gallery and the response of the freshwater lens to pumping. The effects of infiltration gallery operation (i.e., rate of pumping) is also considered.

This report describes the outcomes of four components of conceptual and numerical modelling work, including: (1) Literature review of gallery design (including the information provided by infiltration gallery operators); (2) Development of conceptual models for infiltration galleries installed in atoll islands; (3) Implementation of conceptual models in groundwater flow-only models (i.e., models that neglect water density effects) and density-dependent models (i.e., models that simulate freshwater-saltwater interactions); (4) Development and analysis of modelling scenarios to explore the effects of modifications to the base case parameters.

The initial part of this investigation sought to collate aquifer hydraulic properties of atoll islands and details of infiltration gallery designs employed across the Pacific. The information provided by infiltration gallery operators during the *Pacific Groundwater Gallery Knowledge Exchange* (PGGKE) workshop on Kiritimati Atoll (Kiribati) in November 2023, are also provided. The literature review documented a wide range of information, including the hydrogeological properties of atoll islands and infiltration gallery designs and performance. The latter included data on the layout, depth, length and diameter of pipes, slot characteristics, filter/exclusion layer details, abstraction well/sump specifications, pumping rates, the salinity of extracted water, and a host of other information.

The study utilised the literature review results to formulate three-dimensional conceptual models as precursors to the development of numerical models. Geometric symmetry boundaries were used to limit the scale of conceptual and numerical models (149.5 m x 409 m x 50 m for the base case model), considering the high numerical burden of density-dependent groundwater simulation. These adopted a dual-aquifer system typical of Pacific atoll islands, encompassing Holocene sediments and Pleistocene limestone. The aquifer properties of these models aligned with reported values for atoll islands as obtained from the literature review and PGGKE workshop, while also considering the specific conditions encountered on Kiritimati Atoll (Kiribati). For example, the base-case conceptual model assumed a net recharge rate of 400 mm/y (approximately 40% of annual rainfall), as determined from previous investigations of Kiritimati Atoll. Key parameters of the base case were varied to produce several alternative conceptual models to assess a range of conditions as encountered in other Pacific atoll islands.

Numerical model development was undertaken in two stages, including freshwater-only models (density-independent) and freshwater-saltwater interaction models (density-dependent). Freshwater-only flow models adopted steady-state conditions, whereas freshwater-saltwater interaction models considered transient conditions, albeit the stresses applied to transient models (pumping, recharge, sea level) were constant (in time). The former involved application of MODFLOW to examine the hydraulics of the different infiltration gallery components without the complication of density effects. Two different approaches to representing flow in the pipe were tested: (a) implicit representation of the pipe using a high hydraulic conductivity region (high-*K* approach), and (b) explicit representation of the pipe using the MODFLOW-CFP code that has been developed specifically for groundwater-flow/pipe-flow applications. The MODFLOW results were interrogated using the MODPATH code to show groundwater pathways via particle-tracking analysis.

Density-dependent simulations developed in the second stage of modelling used the SEAWAT code (Guo and Langevin, 2002), which combined MODFLOW (groundwater flow) and MT3D (solute transport) to capture the freshwater and saltwater dynamics, including the effects of salinity on the water density that are critical for the creation of buoyant freshwater lenses. These models represented horizontal pipes using the implicit approach (high-*K*) because MODFLOW-CFP does not have density-dependent capabilities and SEAWAT cannot simulate pipes explicitly.

The study utilised a base case (Case B) in MODFLOW, MODFLOW-CFP, MODPATH and SEAWAT models, involving a straight horizontal slotted pipe aligned parallel to the shoreline. Twelve additional modelling scenarios (Cases 1 to 12) were explored in SEAWAT simulations to assess the influence (e.g., on the freshwater lens and the salinity of the produced water) of changing various design parameters and hydrogeological conditions. Modifications to the base case involved changes to the: pumping rate (Cases 1 and 2), hydraulic conductivity of Holocene sediments (Case 3), thickness of Holocene sediments (Case 4), slotted pipe characteristics (Cases 5, 7 and 8), filter/exclusion layer (Case 6), well configurations (Case 9), and the infiltration gallery layout (Cases 10, 11 and 12). We anticipate further scenarios following feedback from SPC on the results described in this report.

The findings of the modelling analysis validate novel aspects of the methodology and offer new insights into infiltration gallery performance. For example, consistency observed in the results obtained from implicit (MODFLOW) and explicit (MODFLOW-CFP) representations of the horizontal pipe indicates that the high-*K* approach is a viable and effective method for simulating the pipe in SEAWAT. The results of particle tracking for the base case model (Case B) using MODPATH showed the locations of 80 groundwater particles ~15 years prior to entering the pipe. This revealed a capture zone for the slotted pipe extending approximately 52 m both landward and seaward of the pipe (i.e., perpendicular to the pipe's axis). Furthermore, the pipe can capture water from around 25 m beyond its end over the 15-year period of analysis. Pumping-induced drawdown likely occurs over larger distances than capture zones, although drawdown was rather small. Capture zones would likely extend further in models run for longer times. Particle-tracking results underscore the requirement for buffer zones around infiltration galleries to restrict land-use activities and safeguard against pollution from anthropogenic contaminants. The results also highlight the need for offset distances between galleries where several of these are installed.

The results of SEAWAT modelling cases were processed to assess: (a) the elevation of specific salinity (isochlor) contours beneath, and at both ends of, the horizontal pipe as an indicator of localised up-coning, (b) the groundwater salinity in the aquifer immediately below the horizontal pipe, (c) the total volume of freshwater within the model domain, given as an equivalent average freshwater lens thickness (i.e., the ratio of the volume of freshwater stored in the aquifer to the surface area of the aquifer), (d) the concentration of the extracted water, and (e) the drawdown in both the extracted well and the aquifer. Key findings include:

1. Pumping in Case B caused up-coning that resulted in the 0.05-salinity contour rising by 1.24 m from its initial position of 9.32 m below MSL (prior to pumping). The extracted water had a relative salinity of 0.0109, which equates to approximately 1094 μS/cm if recharge water is taken to be 500 μS/cm and seawater is presumed to be 55,000 μS/cm. Measurements of produced-water salinity on Kiritimati Atoll are around 1200-1400 μS/cm, providing supporting evidence that the model offers a reasonable representation of atoll island conditions. Drawdown in the aquifer (water table drop due to pumping) at the beginning of the pipe where it connects to the abstraction well was 68 mm, while drawdown in the abstraction well was 96 mm. The average freshwater lens thickness (defined by cells containing groundwater < 0.01 relative salinity) reduced from 9.23 m in the absence of pumping to 8.30 m with the introduction of the infiltration gallery. If the latter thickness of fresh groundwater was removed from the aquifer, it would fill a container (of the same surface area as the aquifer) to 2.49 m.

2. Reducing the extraction rate (by 50%) in Case 1 relative to Case B: (a) reduced the occurrence of up-coning (0.05-salinity contour was further below mean sea level by ~11%), (b) lowered the salinity of extracted water (by ~51%) to 533 μS/cm, (c) reduced aquifer drawdown (by ~53%), (d) reduced drawdown in the abstraction well (by ~52%), and (e) led to a larger average freshwater lens thickness (by ~8%). The near-linear relationship between pumping and the salinity of extracted water offers a useful rule-of-thumb, at least for the conditions represented in the model, for moderating the produced water salinity by manipulating the rate of extraction.

3. Increasing the slotted pipe length from 100 m (Case B) to 200 m (Case 7) produced similar types of effects as reducing the extraction rate (Case 1), although differing in the magnitude of changes. In comparison to Case B, the 0.05-salinity was ~9% deeper (below mean sea level), the extracted water salinity reduced by ~50% (to 544 μS/cm), the drawdown in the aquifer and abstraction well decreased by ~50% and ~49%, respectively, and the average freshwater lens thickness increased by ~7%. This option requires higher construction costs (longer trench and pipe), and likely allows for fewer infiltration galleries within the relative restricted spaces available on atoll islands for gallery construction. Thus, trade-offs between the gallery length and the pumping rate should be assessed in designing infiltration gallery networks to optimise construction and operation costs, and the volume of fresh groundwater storage.

4. The utilisation of a branched-pipe infiltration gallery (Case 12) showed relatively minor changes in the infiltration gallery performance (e.g., ~0.4% deeper 0.05-salinity, ~7% and ~8% reductions in the drawdown in the aquifer and abstraction well (respectively), and ~0.2% increase in the equivalent average freshwater thickness in the aquifer). The salinity of the produced water was slightly higher (by ~1.5%) in Case 12 (1110 μS/cm) relative to that of Case B. This option required 48 m of additional pipe relative to Case B, compared to 100 m of additional pipe in Case 7 (above). This option therefore produced mixed results in terms of the performance of the gallery. Thus, the return on investment is reduced relative to simply lengthening the horizontal pipe. The usefulness of branched galleries will depend on the specific geometry of lenses in each case. Although branched galleries allow for extraction from a larger area than individual pipes, perhaps requiring fewer abstraction wells and therefore lower operation and maintenance costs, they require prior analysis to ensure that benefits are realised in their construction, especially considered the mixed results observed in the case presented here.

5. Installing the pipe in a Holocene layer that was 50% thicker (10 m in Case B and 15 m in Case 4) enhanced the performance of the infiltration gallery in terms of the depth to 0.05-salinity (~28% deeper) and the extracted water salinity (~35% reduction; 713 μS/cm) compared to Case B. The freshwater lens was ~32% thicker in Case 4 because the Holocene-Pleistocene discontinuity was 5 m deeper. This increase in the lens thickness is less than the increase in the Holocene layer thickness because saltwater invaded more of the deeper Holocene of Case 4. Counterintuitively, the drawdown in

the aquifer and abstraction well increased by ~15% and ~10%, respectively. This occurred because the Holocene sediments were assigned a lower hydraulic conductivity relative to the underlying Pleistocene sediments, and therefore a thicker Holocene layer creates a lower overall transmissivity (causing higher drawdown). This highlights the importance of developing a reasonable understanding of layering within atoll island sediments in designing infiltration galleries and predicting their performance prior to construction investments.

6. Installing infiltration galleries in a Holocene layer with lower hydraulic conductivity (Case 3) resulted in a modest improvement in infiltration gallery performance, evidenced by a ~1.3% greater depth to the 0.05-salinity contour, a ~3% reduction in extracted water salinity, and a ~5% increase in the average freshwater lens thickness compared to Case B. However, the drawdown in both the abstraction well and the aquifer increased by ~77% and ~66% compared to Case B, respectively. Again, higher drawdown is expected in aquifers of lower transmissivity (resulting from the lower hydraulic conductivity of the Holocene layer). This demonstrates the need for aquifer testing to assess sediment hydraulic properties before installing infiltration galleries, particularly as the depth of installation needs to account for the drawdown (and tidal fluctuations in the water table), which depend on the aquifer properties.

7. Altering the slotted pipe conductance in Case 5 (~50% reduction compared to Case B) did not lead to significant changes in the infiltration gallery performance.

8. Case 11 involved simulating a gallery installed perpendicular, and 200 m from, the shoreline with otherwise the same design as a gallery installed parallel to the shoreline and 204.5 m from it (Case B). The model demonstrated a ~3% lower drawdown in the well and a ~6% lower drawdown in the aquifer. However, up-coning occurred to a greater extent in Case 11, whereby the depth to the 0.05-salinity contour was reduced by 80% relative to Case B. This caused the produced water salinity to rise to 1274 μS/cm, which is 16% higher than that of Case B, and the lens thickness was lower by ~5%. This suggests that installing infiltration galleries perpendicular to the shoreline may not achieve comparable performance to those that are parallel to the shoreline. Evaluation of galleries placed at a variety of distances (and orientations) from the shoreline might reveal other trends, but in lieu of those, it appears that galleries placed parallel to the shoreline are preferred.

9. Case 10 adopted an infiltration gallery that was closer to the shoreline (50 m) relative to Case B (204.5 m). This led to the 0.05-salinity contours reaching the base of the infiltration gallery, and in fact, intercepting the water table. The rise in saltwater was reflected in a thinner freshwater lens, which reduced in thickness by ~38% relative to Case B. The salinity of produced water was non-potable, being 5910 μS/cm (440% increase compared to Case B). The drawdown in the abstraction well and aquifer was higher than Case B by ~72% and ~94%, respectively. This shows the importance of

decisions related to the placement of infiltration galleries relative to the shoreline (and other saltwater bodies, such as those that are often found under low-lying land).

10. Utilising geofabric instead of a plastic layer (Case 6) or reducing the pipe diameter (Case 8) produced only minimal impacts on the performance of the infiltration gallery. Specifically, the depth to the 0.05-salinity contour and the average thickness of the freshwater lens remained largely unchanged compared to Case B. Slight reductions in the salinity of the extracted water (~0.5%) were observed in both Cases 6 and 8 relative to Case B. These findings suggest that the geofabric lining and plastic exclusion layer have minimal influence on the infiltration gallery performance, at least where the geofabric is not clogged.

11. The adoption of two wells instead of a central well (Case 9) resulted in relatively minor changes in the performance of the infiltration gallery and the condition of the lens.

12. Case 2 (50% increase in the pumping rate) produced a substantial negative impact on the performance of the infiltration gallery compared to Case B. The 0.05-salinity contour rose significantly (i.e., the depth reduced by ~82%), the average thickness of the freshwater lens decreased (by ~8%), and the salinity of the extracted water rose to 2500 μS/cm (an increase of ~129%). This borders on the limit of potable water. The drawdown in both the abstraction well and aquifer increased by approximately 57% and 62%, respectively, relative to Case B. This result demonstrates that the salinity of the produced water and the pumping rate are not linearly related (50% increase in pumping leads to 129% increase in salinity). Managing the extraction from infiltration galleries thus requires long-term and regular observations of the salinity, pumping rate, drawdown and conditions of the lens, given the nonlinear behaviour that is demonstrated here.

The current study has gathered valuable data on infiltration galleries across the Pacific and represents the first attempt at simulating infiltration galleries in 3D using a grid resolution that affords novel observations of up-coning and other density-dependent processes. While the current results offer helpful guidance on infiltration gallery design elements, there are several research questions that remain, including the effects of tides and smaller-scale heterogeneities on infiltration gallery performance. Intermittent pumping effects are also likely to change the conditions within the gallery and lens, relative to the constant pumping that was assumed in our analysis. Developing a modelling case study of a carefully instrumented infiltration gallery would assist the wider international community in understanding the main processes affecting their performance under field conditions.

Table of Contents

Executive Summary .... **i**
Table of Contents .... **vii**
List of Figures .... **ix**
List of Tables .... **xii**
1. Introduction **1**
1.1 Background 1
1.2 Objectives 3
2. Literature Review **4**
2.1 Background 4
2.2 Natural system characteristics of atoll islands 6
2.2.1 Aquifer hydraulic properties 6
2.2.2 Recharge and evapotranspiration 7
2.3 Description of infiltration gallery components 9
2.3.1 Infiltration gallery layouts 9
2.3.2 Engineering components 11
2.4 Infiltration gallery case studies 15
2.4.1 Technical reports and published literature 15
3. Information provided by Pacific Island Operators **19**
4. Conceptual Model **25**
4.1 Hydrogeological characteristics of atoll islands 25
4.1.1 Aquifer hydraulic parameters 25
4.2 Infiltration gallery layout 26
4.3 Infiltration gallery parameters 28
4.3.1 Plastic/geofabric layer and gravel pack 28
4.3.2 Slotted pipes 29
4.3.3 Hydraulic conductivity along slotted pipes 33
5. Model Design Elements **36**
5.1 Overview of modelling strategy 36
5.2 Modelling codes 37
5.3 Model domain 38
5.4 Boundary conditions 43
5.5 Initial conditions 44
5.6 Incorporating the screen (slots) in the models 44
5.7 Incorporating the gravel pack and plastic/geofabric layer in models 47
5.8 Incorporating horizontal slotted pipe in MODFLOW and SEAWAT models 51
5.9 Incorporating horizontal slotted pipe in a MODFLOW-CFP model 51
5.10 Incorporating of abstraction well/sump into models 53
6. Modelling Scenarios **54**
6.1 Base case model for MODFLOW, MODFLOW-CFP, MODPATH and SEAWAT 54

6.2 Overview of modelling scenarios in variable-density SEAWAT simulations 55
7. Results **58**
7.1 Freshwater-only simulations 58
7.1.1 MODFLOW 58
7.1.2 MODFLOW-CFP 60
7.1.3 MODPATH 63
7.2 SEAWAT variable-density simulations 65
7.2.1 Steady-state simulations prior to installation of the infiltration gallery (Case 0) 65
7.2.2 Case B 70
7.2.3 Cases 1 to 12 75
7.2.4 Comparing the performance of simulated infiltration galleries 82
7.2.5 Discussion of other effects on infiltration gallery performance 86
8. Conclusions and Recommendations **88**
9. Acknowledgements **91**
10. References **92**
11. Appendices **99**
Appendix A – MODFLOW results utilising the equivalent hydraulic conductivity approach 99
Appendix B – Summary of model scenarios 101
Appendix C – Concentration distribution for Cases B to 12 103
Appendix D – Head distribution for Cases B to 12 116

List of Figures

Figure 1. Key hydrogeological characteristics and design elements of a typical infiltration gallery installed in an atoll island. 5
Figure 2. Infiltration gallery layout in Kiritimati Atoll, Kiribati (information on the infiltration gallery layout provided during the PGGKE workshop). 9
Figure 3. Infiltration gallery layout in Lifuka Island, Tonga (information on the infiltration gallery layout provided during the PGGKE workshop). 10
Figure 4. Infiltration gallery layout in West Island, Cocos (Keeling) Islands (infiltration gallery layout taken from Falkland, 1999). 10
Figure 5. Infiltration gallery layout in Bonriki Island, Kiribati (infiltration gallery layout taken from Bosserelle et al., 2015). 11
Figure 6. Schematic representation of: (a) cross-section of an infiltration gallery, with (b) a plastic layer positioned atop the gravel pack, or (c) a geofabric layer surrounding the gravel pack (after Falkland, 2011). 13
Figure 7. Pacific Groundwater Gallery Knowledge Exchange (PGGKE) workshop, Kiritimati Atoll (Kiribati), 1-8 November 2023 (photo provided by SPC). 19
Figure 8. Conceptual diagrams of infiltration gallery layouts in Pacific atoll islands, including: (a) a single horizontal slotted pipe parallel to the shoreline, (b) a single horizontal pipe perpendicular to the shoreline, and (c) a horizontal, branched slotted pipe network that combines (a) and (b). WT refers to the water table, and MSL indicates mean sea level. 27
Figure 9. Slotted-pipe configuration for radial-slot arrangements. 30
Figure 10. Model development sequence. 36
Figure 11. Plan view of a series of infiltration galleries aligned parallel to the shoreline. The red-dashed line delineates the region utilised in simulating the base case model (Case B). 38
Figure 12. Numerical model domain and boundary conditions for a single slotted pipe aligned parallel to the shoreline, in accordance with the conceptual diagram in Figure 8a. The ocean occurs on the vertical back face of the domain at a depth of h_b, while the other vertical faces are no flow boundaries. "Sump" refers to the abstraction well. 39
Figure 13. Numerical model domain and boundary conditions for a single slotted pipe positioned perpendicular to the shoreline, in accordance with the conceptual diagram in Figure 8b. The ocean occurs on the vertical right face of the domain at a depth of h_b, while the other vertical faces are no flow boundaries. "Sump" refers to the abstraction well. 40
Figure 14. Numerical model domain and boundary conditions for a branched slotted pipe, in accordance with the conceptual diagram in Figure 8c. The ocean occurs on the vertical back face of the domain at a depth of h_b, while the other vertical faces are no flow boundaries. "Sump" refers to the abstraction well. 41
Figure 15. Discretisation of the base case model (Case B; see Section 6.1), where the slotted pipe is aligned parallel to the shoreline, showing (a) plan view (x-y), (b) side view (y-z), and (c) 3D model schematic showing the abstraction well/sump and the slotted, horizontal pipe and gravel pack. In (a), the centreline of the horizontal pipe (Case B) is located between (x, y) = (0.5 m, 204.5

m) to (100.5 m, 204.5 m), while in (b), the centre of the pipe (Case B) occurs at (*y*, *z*) = (204.5 m, 48.28 m). 42
Figure 16. Side view of (a) an infiltration gallery, and (b) its representation within a rectilinear conceptual model. 45
Figure 17. Cross-section of the horizontal pipe of an infiltration gallery, showing the representation of the pipe in a model cell ("Screen" refers to the pipe wall): (a) conceptual model, (b) assignment of parameters to the pipe conceptual model, (c) integrated representation of the pipe bore and screen in the numerical model. 46
Figure 18. The actual (dashed circle) and modelled (square) cross-section of the pipe, where D_o is the outer diameter of the pipe and L'_p is one-quarter of the pipe perimeter. 46
Figure 19. Representation of the gravel pack and overlying plastic sheet in numerical models, showing: (a) conceptual model, and (b) numerical implementation. Cells are labelled with the respective hydraulic conductivity parameters. 48
Figure 20. Cross-section of the horizontal pipe of an infiltration gallery, showing the representation of the gravel pack and geofabric layer in a model cell ("Screen" refers to the pipe wall): (a) conceptual model, (b) assignment of parameters to the gravel pack-geofabric conceptual model, and (c) integrated representation of the gravel pack and geofabric layer in the numerical model. 49
Figure 21. Cross-section of the horizontal pipe of an infiltration gallery, showing the representation of the pipe, gravel pack and geofabric layer in a model cell ("Screen" refers to the pipe wall): (a) conceptual model, (b) assignment of K_y values (hydraulic conductivities in the *y*-direction) of infiltration gallery components: pipe, gravel pack and geofabric), and (c) assignment of K_z values (hydraulic conductivities in the *z*-direction of infiltration gallery components: pipe, gravel pack and geofabric). 50
Figure 22. Schematic representation of pipe nodes and segments in MODFLOW-CFP: (a) plan view, and (b) front view, illustrating the configuration for the base case model (Case B; see Section 6.1). 52
Figure 23. Plan view of a series of infiltration galleries aligned parallel to the shoreline with abstraction wells at either end of each gallery. The red-dashed line delineates the region utilised in simulating Case 9. 56
Figure 24. Plan view of a series of infiltration galleries aligned perpendicular to the shoreline. The red-dashed line delineates the region utilised in simulating Case 10. 57
Figure 25. Plan view of a series of branched infiltration galleries, comprising pipes that are both parallel and perpendicular to the shoreline. The red-dashed line delineates the region utilised in simulating Case 12. 57
Figure 26. Head distribution for Case B obtained from the MODFLOW (freshwater-only) model. Black lines show the head contours, while the blue line indicates the water table. White arrows depict flow directions (arrows are shown for only a portion of the model cells). 59
Figure 27. Head distribution for Case B derived from the MODFLOW-CFP (freshwater-only) model. Black lines show the head contours, while the blue line indicates the water table. White arrows depict flow directions (arrows are shown for only a portion of the model cells). 62

Figure 28. The capture zone of an infiltration gallery after ~15 years, obtained through backward-tracking of 80 particles in Case B. Particle paths are represented in 2D planes, as: (a) horizontal plane passing through the middle of the pipe (0.22 m below MSL), (b) cross-section passing through the middle of the pipe (y = 204.5 m), and (c) cross-section passing through the middle of the abstraction well (x = 0.25 m). 64
Figure 29. 3D representation of particle paths showing the capture zone (after ~15 years) for the infiltration gallery of Case B. Water density effects are neglected. 65
Figure 30. Salinity distribution under pre-development, steady-state conditions (prior to the installation of an infiltration gallery; Case 0): (a) Side view displaying the concentrations at x = 0.25 m, representing a cross-section passing through the location where the abstraction well occurs in Case B, (b) Front view of the concentration distribution at y = 204.5 m, corresponding to a cross-section passing through the centreline of the horizontal pipe that is simulated in Case B. A relative salinity scale is adopted, where C = 0 represents freshwater and C = 1 represents seawater. White lines show relative salinity contours, while the light-blue line indicates the water table. 67
Figure 31. Head distributions from Case 0, representing steady-state, pre-development conditions. Black lines show the head contours, while the light-blue line indicates the water table. White arrows depict flow directions (arrows are shown for only a portion of the model cells). Heads are shown in 2D planes that pass through the centre line of the horizontal well and/or the infiltration gallery. 69
Figure 32. Relative solute concentration (C = 0 for freshwater and C = 1 for seawater) for Case B. White lines show the isochlor contours, while the blue line indicates the water table. 71
Figure 33. Head distribution for Case B. Black lines show the head contours, while the blue line indicates the water table. White arrows depict flow directions (arrows are shown for only a portion of the model cells). Heads are shown in 2D planes that pass through the centre line of the horizontal well and/or the infiltration gallery. 74

List of Tables

Table 1. Ranges of parameter values used in atoll island numerical modelling studies (Werner et al., 2017). 7

Table 2. Engineering attributes of the infiltration gallery and island hydrogeological properties that influence the salinity and rate of freshwater extraction, and measurements needed to evaluate the infiltration gallery performance. 14

Table 3. Key parameters for infiltration galleries across eight sites drawn from technical reports and published literature. 15

Table 4. Details on the aquifer and infiltration galleries collected during the PGGKE workshop. 20

Table 5. Pacific islands with infiltration galleries in coral sands (T. Falkland, personal communication during the PGGKE workshop, 1-8 November 2023). 24

Table 6. Aquifer hydraulic properties used in this study 25

Table 7. Properties of slotted pipe (DEPS, 2023) adopted in numerical models of the current study. 31

Table 8. The hydraulic properties of the slotted PVC pipes (150 PN9 UPVC and 100 PN9 UPVC), characterised as per Table 7, determined by Barrash et al.'s (2006) and Bayer-Raich et al.'s (2022) methods. 33

Table 9. Summary of parameter values for calculating K_{ep} and resulting K_{ep} values used in models. 47

Table 10. Summary of parameter values for calculating K_{ep} and K_{eg}, and the resulting values used in the base model (Case B). 51

Table 11. Summary of parameter values used in the base case model (Case B). 54

Table 12. Key observation from the MODFLOW-CFP and MODFLOW models. 61

Table 13. Freshwater lens thickness and water table elevation at the landward boundary (i.e., y = 0 m) and halfway between the shoreline and the landward boundary (i.e., y = 204.5 m, corresponding to the location of the horizontal pipe in Case B). 68

Table 14. Depths to different salinity contours at the position of the abstraction well and the water level in the abstraction well (i.e., x = 0.25 m and y = 204.5 m). Percentage changes (i.e., for Case B) are relative to values for the aquifer before installation of the gallery (Case 0). 72

Table 15. Elevation of salinity contours at the beginning of the pipe where it connects to the abstraction well (i.e., x = 0.5 m and y = 204.5 m for all cases, except Case 9 where the pipe starts at x = 100.5 m and y = 204.5 m). Note that the horizontal pipe ranges from 0.295 to 0.145 m below MSL, and so larger values indicate that salinity contours are below the pipe. The background colour of each cell indicates the cell value, where smaller values are red and larger values are green. 76

Table 16. Freshwater volume in the aquifer and the mean freshwater lens thickness before and after installation of an infiltration gallery. The freshwater volume was calculated for cells with concentrations less than or equal to 0.01 ($C \leq 0.01$). Background colours reflect cell values where red values are larger and green values smaller (in magnitude). 77

Table 17. Salinity of extracted water and within the horizontal pipe at its beginning and end points. Background colours are indicative of cell values, where red indicates larger values and green shows smaller ones. 79
Table 18. Drawdown at the abstraction well, beginning and end of the pipe. The background colour of each cell indicates the cell value, where red identifies larger values and green smaller ones. 81
Table 19. Heads in the slotted, horizontal pipe, as well as head losses along the pipe and between the pipe and the abstraction well. Background colours reflect cell values. 82
Table 20. Results of key performance indicators (PI) from modelling scenarios, taken relative to the base case model (Case B). The cell shading of green-to-red represents a sliding scale between “better” to “worse” conditions in the listed case relative to Case B. 83

1. Introduction

1.1 Background

The extraction of freshwater from aquifers containing both freshwater and saltwater requires specialised techniques. The higher density of more saline water often leads to an increase in salinity with depth below the land surface (e.g., Abarca et al., 2007; Werner et al., 2016). Alternatively, saline groundwater may overly fresher groundwater, but this creates potentially unstable conditions from the perspective of buoyancy forces and requires special conditions for freshwater to persist in these situations (e.g., Knight et al., 2018; America et al., 2020; Pauloo et al., 2021; Solorzano-Rivas et al., 2021). Freshwater pumping from mixed-salinity aquifers is engineered to avoid saltwater entry to the well, which commonly occurs in the form of up-coning plumes (Jakovovic et al., 2016). Up-coning is a localised phenomenon in which the freshwater-saltwater interface beneath a well shifts vertically upwards towards the lower part of the well screen. This movement can lead to an increase in the salt concentration of the pumped water, potentially making it unfit for use (Werner et al., 2009). Measures to avoid up-coning are essential to sustain the extraction of freshwater from atoll islands, because fresh groundwater floats above seawater taking the shape of thin freshwater lenses in atoll island aquifers.

The size and extent of freshwater lenses in atoll islands are controlled by several factors (Werner et al., 2017). These include rates of recharge and groundwater pumping, geological layering (e.g., the thickness of Holocene sediments and depth to the Holocene-Pleistocene discontinuity; Ayers and Vacher, 1986), tidal effects (including the tidal amplitude and the shoreline geomorphology), the timing and scale of episodic overtopping events, aquifer hydraulic properties, island topography, and the distribution and rates of evapotranspiration (Falkland, 1991; Werner et al., 2017; Post et al., 2018). These need to be considered in the design and management of infrastructure for extracting freshwater groundwater from atoll islands.

Several methods are employed on atoll islands to access the freshwater contained in lenses, including dug wells, conventional vertical boreholes, and infiltration galleries (also known as "skimming wells") (Falkland, 2011). Dug wells are a practical choice in regions with low freshwater demands. Conventional vertical boreholes may be suitable for moderate extraction rates; however, they are susceptible to saltwater up-coning in low-lying islands (Falkland, 2011). Infiltration galleries allow pumping to be distributed over a wider area, helping to mitigate saltwater up-coning (Falkland, 2011). Infiltration galleries have proven to be effective in allowing for higher rates of freshwater extraction (than vertical wells) in several Pacific atoll islands, including Tarawa and Kiritimati Atolls (Kiribati) (Falkland and Woodroffe, 1997; White and Falkland, 2010), Kwajalein Island (Marshall Islands) (Hunt, 1996), and Lifuka Island (Tonga) (Sinclair et al., 2014; NJS, 2023). Typical construction involves laying perforated (i.e., slotted) pipe horizontally (or slightly inclined) in an excavated trench. The pipe is surrounded by permeable materials such as gravel to enhance the connection between the pipe and the aquifer and to exclude fine sediment from entering the pipe and/or clogging the pipe slots (Falkland, 1996). Horizontal pipes are laid as either single pipes or branched pipe networks that are connected to one or two collector wells per infiltration gallery (e.g., Falkland, 1996). A collector well serves as an extraction point, a sump to accommodate the pump intake, and an access point for any pipe maintenance or water sampling needs. The extracted water may be fed directly into a distribution network, which often includes storage tanks to balance daily fluctuations in demand. The water may be treated to remove pathogens, odours and colour before being delivered to the island's residents (White and Falkland, 2010).

Although there are several examples of constructed infiltration galleries, their design has thus far relied on basic engineering calculations and experience gained from previous attempts. The current study aims to explore key aspects of infiltration gallery design, assess the influence of different design components on the infiltration gallery performance, and examine in a general sense the impact of infiltration gallery operation on freshwater lenses in atoll islands. This report encompasses the outcomes of three major activities within this project:

Activity 1 - Literature review of gallery design, including the information provided by operators.

Activity 2 - Development of conceptual models for infiltration galleries installed in atoll islands, and implementation of these into groundwater flow-only models (i.e., models that neglect water density effects)

Activity 3 - Development of density-dependent groundwater models to assess freshwater-saltwater interactions under infiltration gallery operation.

The report begins with a literature review of aquifer hydraulic properties of atoll islands and infiltration gallery designs used in islands across the Pacific (Section 2), drawing on published, publicly available literature as well as references provided by the Pacific Community (SPC). Section 3 provides a summary of the findings during the *Pacific Groundwater Gallery Knowledge Exchange* (PGGKE) workshop held in Kiritimati Atoll, Kiribati that was attended by team members from Flinders University and SPC. Section 4 details the hydrogeological conceptual models that apply to installed infiltration galleries in the Pacific, and that will be adopted in numerical models. Conceptual models include hydraulic properties of atoll island aquifers and infiltration gallery parameters including slotted pipes, gravel packs and any filters/exclusion layers (i.e., geofabric/plastic) that are used. These components need to be parameterised in groundwater models so that infiltration gallery performance is properly simulated. Section 5 outlines the model construction and modelling strategy employed for both freshwater-only and freshwater-saltwater models in this study. Section 6 describes the base case model utilised in both freshwater-only and variable-density models. Additionally, it details various modelling scenarios employed to assess the impacts of different infiltration gallery designs on their performance (e.g., in terms of salinity) and their influence on freshwater lenses. Section 7 presents the results of freshwater-only models, explores various freshwater-saltwater modelling scenarios, and provides interpretations of the modelling outcomes. Finally, Section 8 describes the conclusions and recommendations derived from this study.

1.2 Objectives

This study aims to investigate the effects of different infiltration gallery designs on their performance in terms of the salinity of supply and influence on the freshwater lenses of typical atoll islands. To achieve this, 3D groundwater flow models will be generated and used to simulate flow and transport. These simulations will examine the effectiveness of different choices for the main components of infiltration galleries in terms of the freshwater provided to island residents and the condition of the freshwater resource. Engagement between SPC and Flinders University staff to devise the final set of modelling scenarios, following reviews of preliminary results, is an important aspect of the project methodology.

2. Literature Review

2.1 Background

Bennett (1970) suggests that open trenches utilised as infiltration galleries in early efforts to extract freshwater from Pacific atoll islands might be among the oldest methods of groundwater extraction, given their simplicity. However, buried conduits have proven to be more effective than open trenches in sourcing fresh groundwater from atoll islands, primarily due to the reduced risk of contamination (Falkland, 1991; SOPAC, 2007). Figure 1 provides a conceptual schematic of a typical infiltration gallery (or “skimming well”) constructed in an atoll island, showing the principal engineering components and key hydrogeological characteristics. These include the perforated horizontal pipe and the abstraction well within which a pump (or pump intake) is installed. Filter and exclusion materials are used in the form of a gravel pack, geofabric and/or plastic liners. These enhance the connection between the well and the aquifer and exclude fine materials from entering the well or clogging the well slots. Relevant characteristics of the natural system include the depth to the Thurber discontinuity, which is the geological transition between Holocene and Pleistocene sediments, also known as the Holocene-Pleistocene unconformity. Others include the hydraulic properties of Holocene and Pleistocene sediments, depth to the water table, depth to the freshwater-saltwater interface, recharge and evapotranspiration, amongst a wider array of controlling processes (e.g., tides, soil properties, vegetation cover, etc.).

The primary purpose of infiltration galleries is to distribute the extraction of freshwater over larger areas than occurs when a traditional vertical well is used (UNEP, 1998). This is intended to limit localised depression (i.e., drawdown) of the groundwater levels and the accompanying saltwater up-coning, resulting in extracted water of lower salinity (UNEP, 1998). Saltwater up-coning is the vertical rise of saltwater towards a pumping well, and is a complex, density-dependent process that depends on the natural properties of the aquifer, the construction and operation of pumping infrastructure, and factors affecting the dispersive mixing between freshwater and saltwater (e.g., Reilly and Goodman, 1987). These include tides, evapotranspiration and other natural forces acting on the aquifer, plus the design of the infiltration gallery. Together, these affect the gallery’s performance in terms of the allowable pumping rate and the salinity of extracted water (Post et al., 2018; Werner et al., 2017), as well as the long-term sustainability of the island’s freshwater lens, including its thickness and the volume of stored freshwater.

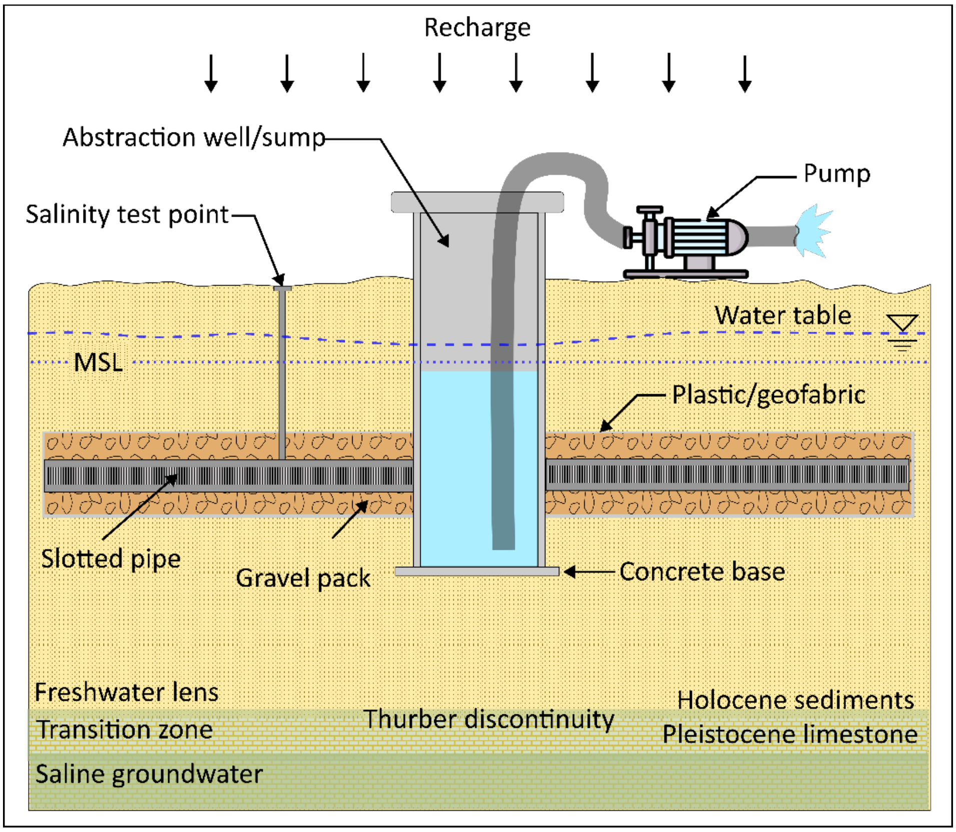

Figure 1. Key hydrogeological characteristics and design elements of a typical infiltration gallery installed in an atoll island.

It is challenging to conceptualise and quantify the full gamut of hydrogeological complexities that affect the design and performance of infiltration galleries. The few previous attempts to build groundwater models for studying infiltration galleries have omitted several key controlling factors. Thus, designs draw to a large part on prior experience, which is documented mainly within construction plans and industry reports (e.g., Falkland, 1999) with limited research into the components of an infiltration gallery that might affect its performance.

The sections that follow review the key natural system characteristics of atoll islands and the components of infiltration galleries that are expected to influence their performance in extracting fresh groundwater from atoll islands in the Pacific. The information in this section in drawn from a wide range of publicly available literature, along with references provided by SPC. The current review draws heavily on previous references on atoll island hydrogeology by Custodio and Bruggeman (1987), Falkland (1991) and Werner et al. (2017).

2.2 Natural system characteristics of atoll islands

2.2.1 Aquifer hydraulic properties

Most atoll island aquifers are treated as a two-layer system, comprising poorly consolidated Holocene sediments deposited over a Pleistocene limestone reef formation (Ayers and Vacher 1986; White and Falkland, 2010). The Thurber discontinuity separates the two formations and is a key factor controlling the thickness of freshwater lenses in atoll environments (Ayers and Vacher, 1986; Anthony, 2004; Buddemeier and Oberdorfer, 2004). The freshwater zone is typically constrained to the Holocene sediments, which usually have lower permeability than the underly Pleistocene limestone. The transition zone (representing the region of mixing between freshwater and seawater) is often predominantly situated within the higher Pleistocene limestone, at least for larger islands (Falkland et al., 2003).

The Holocene sequence typically comprises loose coral sands, and coral and shell fragments, creating mostly unconsolidated sediments to a depth of approximately 10-20 m below ground level, with the lower portion of this zone typically composed of sands with cemented layers. There is often a reef-flat plate comprising semi-permeable reef rock that forms within the Holocene aquifer across part of the island (Maréchal et al., 2022). The Pleistocene sequence is generally treated as weathered limestone, consisting of calcified coral with significant porosity in the form of karst conduits and fractures (Bourrouilh-Le Jan, 1998; Genthon et al., 2008). The Pleistocene limestone may be further divided (vertically) due to differences in aquifer properties with depth (e.g., Alam et al., 2002; Bosserelle et al., 2015). This led some modelling studies of atoll islands to adopt hydraulic properties for the Pleistocene limestone that vary with depth (e.g., Bosserelle et al., 2015; Jazayeri et al., 2019). However, evidence to support this approach is limited in field studies of atoll hydrogeology.

The parameter values utilised in previous numerical studies of atoll islands are detailed in Table 2 of Werner et al. (2017). Table 1 summarises these, thereby providing ranges for key model inputs. These include the horizontal and vertical hydraulic conductivity (K_x [LT^{-1}] and K_z [LT^{-1}], respectively), porosity (n [-]), longitudinal dispersivity (α_L [L]) and horizontal and vertical transverse dispersivities (α_T [L] and α_V [L], respectively), specific yield (S_Y [-]), and the recharge rate (R [LT^{-1}]). The values for K_x, K_z and n differ between Holocene and Pleistocene sediments.

Table 1. Ranges of parameter values used in atoll island numerical modelling studies (Werner et al., 2017).

Parameter		**Range**
Thickness of Holocene sediments, d (m)		5-50
Horizontal hydraulic conductivity, K_x (m/d)	Holocene sediments	15-80
	Pleistocene limestone	173-5000
Anisotropy ratio (vertical to horizontal hydraulic conductivity; K_z/K_x), (-)	Holocene sediments	1:1 to 1:10
	Pleistocene limestone	1:1 to 1:100
Porosity, n (-)	Holocene sediments	0.2-0.25
	Pleistocene limestone	0.01-0.3
Specific yield, Sy (-)		0.15-0.30
Longitudinal dispersivity, α_L (m)		0.02-50
Vertical transverse dispersivity, α_V (m)		0.01-1
Horizontal transverse dispersivity, α_T (m)		0.001-1
Recharge rate, R (mm/y)		200-2920

2.2.2 Recharge and evapotranspiration

The occurrence of freshwater lenses in atoll islands depends on temporal and spatial patterns of recharge, which are the consequence of rainfall and evapotranspiration, where the latter may include soil water (unsaturated zone) evapotranspiration, groundwater evapotranspiration and interception losses. Interception is the capture and evaporation of rainfall within the vegetation canopy and may be substantial in some atoll island settings (Alam and Falkland, 1997; Alam et al., 2002).

Where groundwater evapotranspiration is neglected in estimates of recharge, the "gross" recharge is obtained, whereas the "net" recharge is estimated when both groundwater and soil water evapotranspiration are accounted for. A water balance analysis of the unsaturated zone (the region between the land surface and the upper boundary of the saturated zone or water table) can be undertaken to estimate either gross or net recharge rates. A basic water balance equation is often used to achieve this, as described by Alam et al. (2002):

$$R = P - E \pm \Delta V \tag{1}$$

where R [LT^{-1}] is recharge (net), P [LT^{-1}] is rainfall, E [LT^{-1}] is the actual evapotranspiration from both soil water and groundwater stores and including interception losses (thus R is net recharge), and ΔV [LT^{-1}] is the change in the unsaturated zone storage (per unit land area). The actual evapotranspiration is distinct from "potential" evapotranspiration, which represents the upper bound to evapotranspiration that might occur from constantly wet surfaces. For atoll islands, the ΔV term is often disregarded due to shallow water tables and the limited storage of the unsaturated zone and considering that ΔV averaged over time likely exhibits only small changes. Climate records, vegetation cover, vegetation water use, and root-depth information are typically required to apply Equation (1), including the breakdown of transpiration, evaporation and interception components of evapotranspiration (Falkland, 1992; Post et al., 2018).

An estimate of the capillary rise from the water table into the unsaturated zone (for use by non-phreatophyte vegetation) may be needed in estimating *E*, at least where capillary rise supports water uptake by vegetation. Whether this occurs or not on atoll islands is rarely studied, and is likely associated with two opposing processes: (1) the shallow water table conditions of most atoll islands provide opportunities for groundwater uptake by vegetation (either uptake by phreatophytes or capillary rise from the water table into the unsaturated zone), and (2) the small capillary fringe expected in coarse atoll island sediments is a limiting factor for the transpiration of groundwater by vegetation that require unsaturated conditions for water uptake to occur.

Where groundwater evapotranspiration is neglected in gross recharge estimates, the evapotranspiration of groundwater (E_g [LT^{-1}]) needs to be considered separately to that of the unsaturated zone. MODFLOW-based models adopt a groundwater evapotranspiration function within the EVT package (e.g., Harbaugh, 2005), whereby E_g depends on the depth of the water table below the land surface. The potential evapotranspiration is realised when the water table reaches the land surface, while E_g is lower for larger water table depths below the land surface, becoming zero for water tables below a given 'extinction depth'.

Prior numerical modelling studies of atoll islands have employed a broad range of recharge values due mainly to the wide range of climate conditions, spanning 200 to 2920 mm/y, as documented by Werner et al. (2017).

In studies that attempt to simulate the groundwater salinity of atoll islands, the chloride of recharge needs to be estimated if simulated salinities are compared to corresponding field measurements. Either the total dissolved solids (TDS) or the concentration of chloride may be used as measures of salinity. Chloride is adopted as a surrogate for the salinity of recharge because of its conservative properties. Post et al. (2018) accounted for the evapo-concentration of rainfall salts by adopting a total dissolved solids (TDS) for recharge of 310 to 450 mg/L for recharge ranging from >1200 mm/y to <600 mm/y, respectively. This was found to best reproduce shallow groundwater salinities.

If one assumes that the recharge salinity reflects the evapo-concentration of atmospheric salt deposition (from both dry and wet deposition; Bresciani et al., 2014), then the recharge salinity can be estimated from a classical chloride mass balance approach, as:

$$T_r = \frac{PT_p}{R} \tag{2}$$

where T_r [ML^{-3}] is the TDS of recharge, T_p [ML^{-3}] represents the total atmospheric deposition of salt given as the mean TDS of bulk rainfall samples, while *P* (rainfall) and *R* (recharge) are defined previously. Approximating the bulk salinity of rainfall (T_p) on atoll islands is challenging due to high variability in salt spray (Falkland and Brunel, 1993). Assuming that the salt deposition on Kiritimati Island falls in the range 10-100 mg/L (chloride concentration), and the mean rainfall is 1000 mm/y, a recharge of 400 mm/y will be accompanied by recharge chloride values of 25-250 mg/L. These equate to rainfall TDS values of 45-450 mg/L (using a ratio of 1.8 for TDS/chloride concentration). The range of rainfall salt deposition values adopted here were taken from values for islands that are not atolls (i.e., Naranjo et al., 2015; Bryan et al., 2016) because of a lack of relevant measurements on atolls. Nevertheless, the TDS for recharge adopted by Post et al. (2018) from shallow groundwater measurements at least falls within reasonable bounds. Given the lower rainfall of Kiritimati Atoll relative to Tarawa Atoll, recharge salinities are likely to be higher on average than those adopted by Post et al. (2018).

2.3 Description of infiltration gallery components

2.3.1 Infiltration gallery layouts

Various infiltration gallery layouts have been implemented in Pacific islands. The infiltration gallery is often placed approximately parallel to the shoreline, as occurs in Kiritimati Atoll (Kiribati; Figure 2), Lifuka Island (Tonga; Figure 3), West Island, (Cocos (Keeling) Islands; Figure 4), Nanumea and Vaitupu Atolls (Tuvalu), and Bonriki Island (Kiribati; Figure 5). Although the Cocos (Keeling) Islands are located in the Indian Ocean, they are incorporated into this report because the information on the infiltration galleries installed in those islands offer valuable insights to comparable atoll settings in the Pacific.

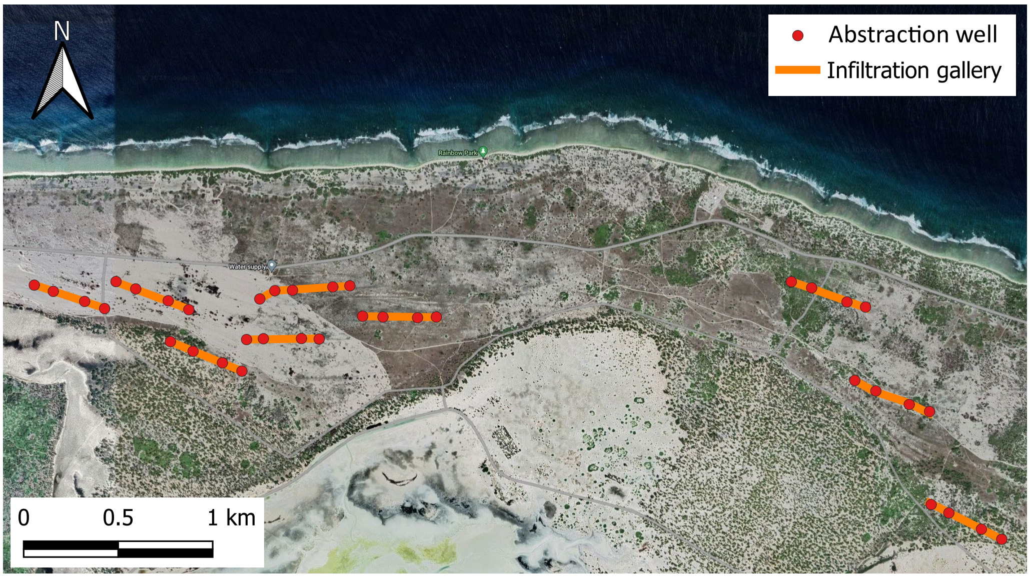

Figure 2. Infiltration gallery layout in Kiritimati Atoll, Kiribati (information on the infiltration gallery layout provided during the PGGKE workshop).

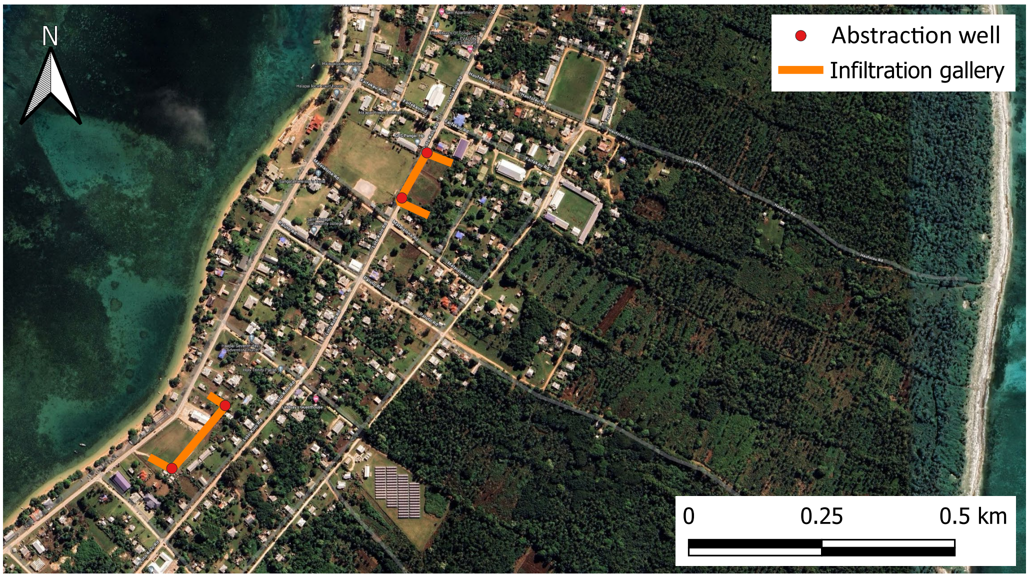

Figure 3. Infiltration gallery layout in Lifuka Island, Tonga (information on the infiltration gallery layout provided during the PGGKE workshop).

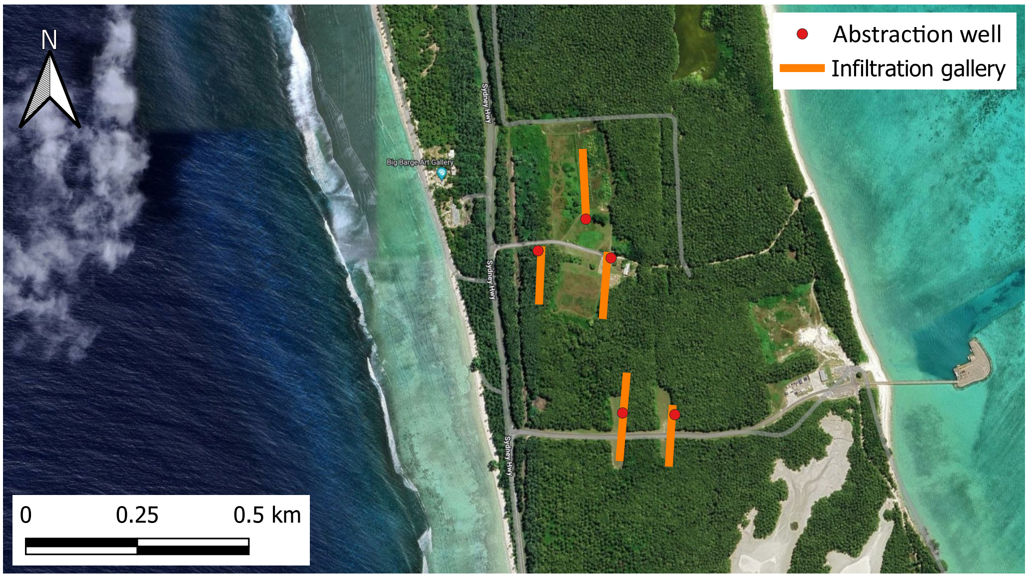

Figure 4. Infiltration gallery layout in West Island, Cocos (Keeling) Islands (infiltration gallery layout taken from Falkland, 1999).

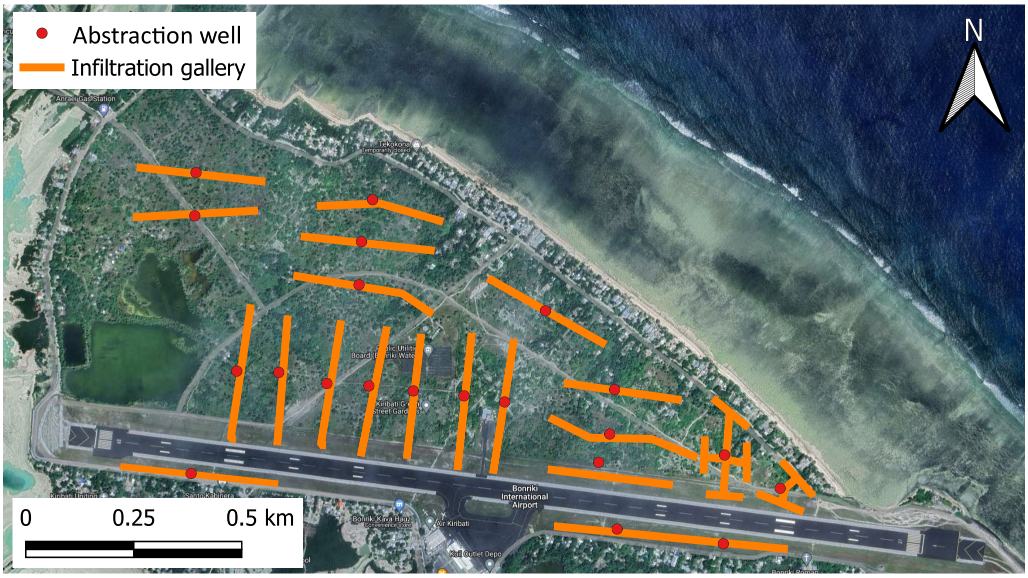

Figure 5. Infiltration gallery layout in Bonriki Island, Kiribati (infiltration gallery layout taken from Bosserelle et al., 2015).

Infiltration galleries have also been constructed almost perpendicular to the shoreline, although mainly in larger atoll islands where the gallery can be placed away from the island's shorelines. In Bonriki Island, infiltration galleries have been installed in a variety of oblique angles with the shoreline in a network that also includes both single-pipe and branched-pipe networks (Figure 5).

Infiltration gallery layouts also differ in the position of the abstraction well, which may be placed centrally or at one or both ends of the horizontal pipe, as evident in Figures 2 to 5.

2.3.2 Engineering components

Here, the main engineering components of infiltration galleries are outlined, with a focus on those that were considered in the modelling analysis that follows. These represent the engineering attributes thought to be of greatest importance for the design, construction and operation of infiltration galleries.

Figure 6 presents a conceptual illustration and key dimensional attributes of an infiltration gallery installed in an atoll island. Design elements that are omitted from Figure 6 include: depth to the Thurber discontinuity (see Figure 1), the width of the freshwater-saltwater mixing zone (i.e., a sharp transition zone is shown whereas a mixing zone exists in reality), placement of the infiltration gallery relative to the shoreline and other galleries, natural hydrological characteristics such as recharge, evapotranspiration, surface water bodies and sediment heterogeneities, and other complexities that influence the performance, such as tides, surface flooding (i.e., with seawater or freshwater), anthropogenic threats of surface contamination, transient variability in hydrological forces (e.g., recharge seasonality, etc.), and factors leading to well clogging (e.g., vegetation roots, bacterial growth), amongst others (Custodio and

Bruggeman, 1987; Falkland, 1991). A multitude of other social, cultural and economic considerations are also relevant to the design of infiltration galleries, including land availability, land use activities, energy supply, environmental impacts, etc. (Falkland, 1991) that are not considered in the current review.

Table 2 lists the main characteristics of an infiltration gallery and the surrounding natural hydrogeological system. These are the elements considered to be important for the design and operation of galleries in atoll island settings. That is, the parameters listed in Table 2 need to be quantified for the modelling investigation that follows (Section 4). Many of the performance measures listed in Table 2 are also important, in a more general sense, for managing infiltration gallery operation, serving as indicators of the performance of the system. This is necessary to monitor groundwater conditions, to develop an understanding of salinity versus pumping rates, and to guide gallery maintenance activities. Values for the Table 2 parameters are provided based on literature review in the subsections that follow, and in Section 3 arising from the PGGKE workshop.

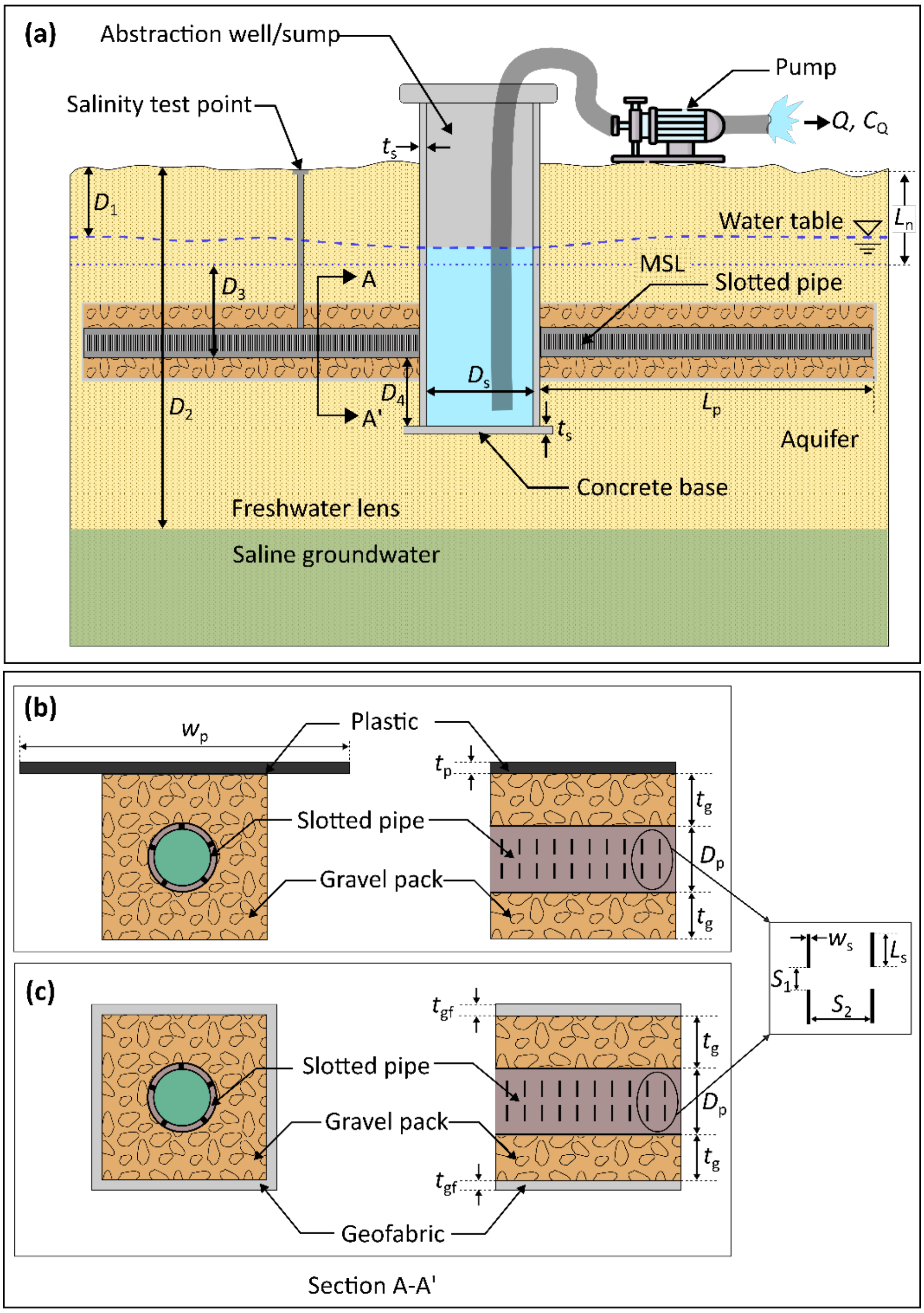

D_1 = Depth of water table
D_2 = Depth of freshwater-saltwater interface
D_3 = Depth of pipe base below MSL
D_4 = Depth of sump base below pipe base
Q = Extraction rate
C_Q = Electrical conductivity of extracted water
D_p = Nominal pipe diameter
D_s = Sump diameter
MSL = Mean sea level
L_n = Land surface elevation above MSL

L_p = Pipe length
L_s = Slot length
S_1 = Slot spacing (circumferential)
S_2 = Slot spacing (longitudinal)
w_s = Slot aperture
t_g = Gravel pack thickness
t_{gf} = Geofabric thickness
t_p = Plastic thickness
t_s = Sump's wall/base thickness
w_p = Plastic width

Figure 6. Schematic representation of: (a) cross-section of an infiltration gallery, with (b) a plastic layer positioned atop the gravel pack, or (c) a geofabric layer surrounding the gravel pack (after Falkland, 2011).

Table 2. Engineering attributes of the infiltration gallery and island hydrogeological properties that influence the salinity and rate of freshwater extraction, and measurements needed to evaluate the infiltration gallery performance.

Component	**Variable**	**Parameter**	**Unit**
Aquifer	R	Recharge	mm/y
	S_y	Specific yield	-
	n	Porosity	-
	K	Hydraulic conductivity (horizontal K_x, vertical K_z)	m/d
	D_1	Depth of water table below ground level	m
	D_2	Depth of freshwater-saltwater interface below ground level	m
	L_n	Land surface elevation (above mean sea level; MSL)	m
Slotted pipe	-	Layout (parallel/perpendicular/network)	-
	D_3	Depth of pipe base below MSL	m
	L_p	Pipe length	m
	D_p	Nominal pipe diameter (i.e., pipe's external diameter)	mm
	L_s	Slot length	mm
	S_1	Slot spacing (circumferential)	mm
	S_2	Slot spacing (longitudinal)	mm
	w_s	Slot aperture	mm
Filter/exclusion layer	t_p	Plastic exclusion layer thickness	mm
	w_p	Plastic exclusion layer width	mm
	t_{gf}	Geofabric thickness	mm
	K_{gf}	Hydraulic conductivity of geofabric	m/d
Gravel pack	t_g	Gravel pack thickness	mm
	K_g	Hydraulic conductivity of gravel pack	m/d
Abstraction well/sump*	D_4	Depth of sump base below pipe base	m
	D_s	Abstraction well diameter or horizontal dimension of non-circular wells	m
	t_s	Abstraction well wall/base thickness	mm
	Q	Average extraction rate	m^3/d
	-	Number of slotted pipes connected to an abstraction well	-
Performance measures	C_Q	Electrical conductivity of extracted water	µS/cm
	-	Drawdown at key locations	m
	-	Interface depth below ground level at key locations	m
	-	Incidences of fail-to-pump**	-

*Presumed to comprise impermeable walls; **Due to insufficient head in the abstraction well.

2.4 Infiltration gallery case studies

2.4.1 Technical reports and published literature

In this section, the values of key parameters applicable to the design of infiltration galleries (as listed in Table 2) are compiled from technical reports and published literature. These include references provided by SPC and based on a review of publicly available documents. Table 3 summarises the values of important parameters related to infiltration galleries from eight sites.

Table 3. Key parameters for infiltration galleries across eight sites drawn from technical reports and published literature.

Reference	Falkland (1996)				Falkland (1999)
Location	Bonriki and Buota Islands (Kiribati)	Aitutaki Island (Cook Islands)	Kwajalein Island (Marshall Islands)	Home Island (Cocos (Keeling) Islands)	Home Island (Cocos (Keeling) Islands)
Water table (D_1)	1-2 m BGL (Bonriki)	n/a	n/a	n/a	1-2 m BGL
Depth of freshwater-saltwater interface	n/a	n/a	n/a	Freshwater lens thickness of up to 11 m	n/a
Orientation relative to the shoreline	Mixed (Bonriki)	Parallel	n/a	n/a	Mixed
Depth of pipe base	n/a	1.25 m BWT	n/a	0.3 m BMSL	0.3 m BMSL
Length of horizontal pipes (L_p)	~85 m to ~313 m	130-140 m	n/a	100 m	~300 m (Home Island Main Lens); 150-200 m (Horticultural Block)
Pipe diameter (D_p) (pipe material)	100 mm (PVC)	800 mm (porous concrete); 225 mm (PVC)	n/a	100 mm (PVC)	100 mm (PVC)
Slot length (L_s)	n/a	200 mm	n/a	n/a	n/a
Slot spacing (S_2)	n/a	100 mm (longitudinal)	n/a	n/a	n/a
Slot aperture (w_s)	n/a	n/a	n/a	n/a	n/a
Filter/exclusion layer	n/a	PVC sheet (1 m wide; 200 mm above top of pipe)	n/a	Polythene sheet (100-200 mm above top of pipe)	Polythene sheet (100-200 mm above top of pipe)

Reference	Falkland (1996)				Falkland (1999)
Location	Bonriki and Buota Islands (Kiribati)	Aitutaki Island (Cook Islands)	Kwajalein Island (Marshall Islands)	Home Island (Cocos (Keeling) Islands)	Home Island (Cocos (Keeling) Islands)
Gravel pack thickness (t_g) (aggregate size)	n/a	200 mm (5-10 mm aggregate)	n/a	100-200 mm	100-200 mm
Abstraction well (number/spacing of wells, well construction)	n/a	Two wells for each original gallery; one well in a new gallery	Small diameter pump wells at ~60 m spacing	1.5 m diameter (concrete); central well	1.5 m diameter (concrete); central well
Depth of sump base	n/a	n/a	n/a	0.3 m BPB	0.5 m BMSL
Extraction rate	Total of 1300 m^3/d for 6900 m combined length of 17 galleries in Bonriki and 6 galleries in Buota (average of 56 m^3/d per gallery or 0.19 m^3/d per metre of gallery)	Total of 480 m^3/d for 140 m original gallery (average of 3.4 m^3/d per metre of gallery); Total of 259 m^3/s for new gallery (average of 2 m^3/d per metre of gallery)	Total of 340 m^3/d for 2120 m combined length of 7 galleries (average of 48 m^3/d per gallery or 0.16 m^3/d per metre of gallery)	Total of 110 m^3/d for 1833 m combined length of 6 galleries (average of 19 m^3/d per gallery or 0.06 m^3/d per metre of gallery)	Total of 6.4-32.5 m^3/d for 3 galleries in Horticultural Block (average 2-11 m^3/d per gallery); Total of 12-82 m^3/d for 2 galleries in Quarantine Station (average of 6-41 m^3/d per gallery)
EC of extracted water	1000 µS/cm (highest EC in 1998-2001; combined water from Bonriki and Buota)	n/a	n/a	1500 µS/cm (as upper salinity criteria)	1500 µS/cm (as upper salinity criteria)
Drawdown	n/a	n/a	n/a	30-50 mm	30-50 mm

n/a – not applicable or unreported; m BMSL = metres below mean sea level; m BWT = metres below water table; m BPB = metres below pipe base.

Table 3. (cont'd)

Reference	Falkland et al. (2003)*	NRW Specialists (2021)	White and Falkland (2004)
Location	Abatao and Tabiteuea Islands (Kiribati)	Kiritimati (Kiribati)	Bonriki Island (Kiribati)
Water table	0.3-2.6 m BGL	n/a	0.7 m above MSL
Depth of freshwater-saltwater interface	5-17 m BGL	n/a	8.8 m to 21 m (freshwater lens thickness)
Orientation relative to the shoreline	Abatao Island (2 parallel galleries, 1 branched); Tabiteuea Island (2 parallel, 3 mixed orientation)	n/a	Mixed orientation
Depth of pipe base	0.4 m BMSL	0.3 m BMSL	0.3 m BMSL
Length of horizontal pipes	250-300 m	200 m	300 m
Pipe diameter (pipe material)	100 mm (PVC)	100 mm (PVC)	100, 150, 225 mm (PVC Class 6)
Slot length (slot type)	80 mm (machine-cut radial slots)	n/a	n/a
Slot spacing	5 slots per pipe circumference; 25 mm spacing (longitudinal)	n/a	n/a
Slot aperture	1-1.25 mm	1 mm	n/a
Filter/exclusion layer	Exclusion layer (polythene membrane)	Exclusion layer (plastic sheet, 2 mm thickness, 600 mm wide)	Exclusion layer (polythene sheet, 100-200 mm above top of pipe)
Gravel pack thickness (aggregate size)	150 mm (6-8 mm diameter "pea" gravel)	150 mm (6-10 mm diameter aggregate)	n/a
Abstraction well (number/spacing of wells, well construction)	1 m diameter fibreglass (central); 8-10 mm wall thickness	1 m diameter fibreglass (central)	1.5 m diameter concrete (central)
Depth of sump base	n/a	0.6 m BMSL	0.6 m BMSL
Extraction rate	25-30 m^3/d (per gallery)	n/a	49.7-139.4 m^3/d (per gallery)
EC of extracted water	n/a	n/a	454-1026 µS/cm (October 2004)
Drawdown	n/a	n/a	2-200 mm

n/a – not applicable or unreported; m BMSL = metres below mean sea level; m BWT = metres below water table; m BPB = metres below pipe base; *Proposed infiltration galleries in Abatao and Tabiteuea Islands.

Table 3 provides values for only a subset of the parameters needed to develop numerical models of operating infiltration galleries, and varying levels of information is provided in each reference. Parameters that are omitted from Table 3 and yet require values to complete the conceptual and numerical models described in Sections 4 and 5 include aquifer properties (recharge, specific yield, porosity, hydraulic conductivity), circumferential slot spacing, and the thickness and hydraulic conductivity of any geofabric used. A more complete understanding of infiltration gallery designs was achieved from the PGGKE workshop, as described in the following section.

3. Information provided by Pacific Island Operators

This section summarises the information provided by infiltration gallery operators and Pacific Island hydrogeologists who attended the *Pacific Groundwater Gallery Knowledge Exchange* (PGGKE) workshop, organised by SPC on Kiritimati Atoll (Kiribati) during 1-8 November 2023. The PGGKE workshop aimed to facilitate the exchange of knowledge regarding infiltration galleries in the Pacific, drawing participation from over 35 attendees representing various Pacific countries and Smal Island Developing States (SIDS), including the Marshall Islands, Tuvalu, Kiribati, Fiji, Cook Islands and Tonga, as well as coastal groundwater researchers from Australia (Figure 7).

Figure 7. Pacific Groundwater Gallery Knowledge Exchange (PGGKE) workshop, Kiritimati Atoll (Kiribati), 1-8 November 2023 (photo provided by SPC).

The Flinders University and SPC team gather details about infiltration galleries constructed (or planned) in Pacific islands during the PGGKE workshop. Table 4 provides details regarding the aquifer and infiltration galleries in Pacific islands gathered during the PGGKE workshop.

Table 4. Details on the aquifer and infiltration galleries collected during the PGGKE workshop.

Island (Country) / Component	Kiritimati (Kiribati)	Lifuka (Tonga)	Aitutaki (Cook Islands)	Nanumea (Tuvalu)	Vaitupu (Tuvalu)	Bonriki (Kiribati)
Island type – atoll, volcanic, etc.	Atoll	Coral island	Atoll (volcanic)	Atoll	Atoll	Atoll
Surface soil type, sand, sandy clay, etc.	Sand	Sand & limestone	Sand & volcanic soils	Sand	Sand	Sand
Long dimension (km)	52	8.11	7.94	10.69	5	4.12
Short dimension (km)	6	0.85	1.11	0.17-0.6	0.85	0.87
Island area (km^2)	388.4	11.4	18.3	3.9	5.6	1.86
Mean annual rainfall (mm/y)	992	1700	1876[1]	500-600[2]	412[1]	2000
Mean potential evapotranspiration (mm/y)	1800	1548[3]	n/a	n/a	n/a	n/a
Max. land surface elevation (m MSL)	2.5 m (avg.), 13 m (max.)	22 m MSL (max.)	119 m MSL (max.)[4]	n/a	n/a	n/a
Maximum tidal range (HAT minus LAT)[5] (m)	1.032	1.567	0.478	2.330	2.330	1.342
Main vegetation type	Coconuts & te mao	Coconuts	Coconuts, mango, others	Coconuts	Coconuts	Coconuts
Population of island	7500	3000	1700	512	1800	2000
Population of supply	7500	3000	1700	Drought mostly	Drought mostly	60,000 (supplied by Bonriki & Buota)

n/a – not applicable or unreported.
[1]https://weather-and-climate.com
[2]WBG and ADB (2021)
[3]Sinclair et al. (2014)
[4]Stoddart (1975)
[5]http://www.bom.gov.au/oceanography/projects/spslcmp/tidecalendars.shtml

Table 4 (cont'd) - Aquifer

Island (Country) / Component	Kiritimati (Kiribati)	Lifuka (Tonga)	Aitutaki (Cook Islands)	Nanumea (Tuvalu)	Vaitupu (Tuvalu)	Bonriki (Kiribati)
Typical depth to the water table (m)	2-3	3-5	2-3	2	3	2-3
Thickness of freshwater (m)	5-15	3-9	3-9	n/a	n/a	5-20
Typical water table height above MSL (m)	0.3-0.7	0.3-0.7	2-3	n/a	n/a	0.5-1
Average recharge (% of rainfall)	40	30	28	50	50	35-40
Holocene thickness (m)	10-20	2-19	up to 20	n/a	n/a	10-20
Holocene Hydraulic conductivity (m/d)	5	n/a	n/a	n/a	n/a	5-10
Holocene porosity (-)	0.3	n/a	n/a	n/a	n/a	0.3
Upper Pleistocene hydraulic conductivity (m/d)	500-1000	n/a	Volcanic rock	n/a	n/a	500-1000
Lower Pleistocene hydraulic conductivity (m/d)	n/a	n/a	n/a	n/a	n/a	n/a
Vertical/horizontal anisotropy	n/a	n/a	n/a	n/a	n/a	n/a
Pleistocene porosity (-)	n/a	n/a	n/a	n/a	n/a	n/a
Specific yield (-)	0.3	n/a	n/a	n/a	n/a	0.3

n/a – not applicable or unreported.

Table 4 (cont'd) - Infiltration gallery

Island (Country) / Component	Kiritimati (Kiribati)	Lifuka (Tonga)	Aitutaki (Cook Islands)	Nanumea (Tuvalu)	Vaitupu (Tuvalu)	Bonriki (Kiribati)
Number of operating galleries	13	3	8	n/a	n/a	21 (+6 on Buota)
Number of non-operating galleries	3	n/a	2	n/a	n/a	1
Pipe length per gallery (m)	400-500; plus three smaller galleries each 24 m long; 300 (year 2024)	100-170	50-100	200	200	200-300
Island sustainable yield	2000 m^3/d	20% of recharge	n/a	20% of recharge	20% of recharge	1660 m^3/d
Mean extraction rate per operating gallery (m^3/d)	30-40	30-40	>40	n/a	n/a	50-90
Years of gallery construction	2000, 2017, 2024	1997, 1999	1970s, 2018	2024	2024	1984, 1986, 2005
Average salinity per gallery (µS/cm)	450-1200	800-1500	400-1800	n/a	n/a	800-1000
Maximum salinity per gallery (µS/cm)	4000	2000	6000-8000	n/a	n/a	1500
No. of pump wells per gallery	1 to 3 (mostly 2)	1-2	1	1 (planned)	1 (planned)	1
Energy source and pump type (solar?)	Solar submersible; Wind surface; Petrol surface	Solar surface; Electric (grid) surface; Diesel surface	Electric (grid) surface & submersible	Solar submersible (planned)	Solar submersible (planned)	Electric surface (grid)
Gallery pipe internal diameter (mm)	100; 150 planned for 2024	100	1000 (concrete); 900×900 (EcoBloc); 225 PVC	150 (planned)	150 (planned)	100
Gallery pipe type/wall thickness	PN12	Class 9	50 mm (concrete); PN12 PVC	PN9 Series 1 (6.7 mm)	PN9 Series 1 (6.7 mm)	Class 12
Pipe type	PVC	PVC	Concrete; EcoBloc; PVC	PVC	PVC	PVC
Slot type (longitudinal (Long.), circumference (Circ.))	Long. (year 2000); Circ. (year 2017+)	Circ.	Porous concrete & joins; Long. (PVC)	Circ.	Circ.	Long.
Slot aperture (mm)	6 (year 2000);	2-3	n/a	1	1	2

Island (Country) / Component	Kiritimati (Kiribati)	Lifuka (Tonga)	Aitutaki (Cook Islands)	Nanumea (Tuvalu)	Vaitupu (Tuvalu)	Bonriki (Kiribati)
	0.8 (year 2017+)					
Longitudinal slot spacing (mm)	100 mm long & 100 mm apart Circ..: 10 mm	n/a	n/a	10 mm	10 mm	100 mm
Slots per circumference	Long.: 4 Circ.: 4	n/a	n/a	5	5	4
Depth below MSL to pipe invert (m)	300	300	n/a	450	450	300
Width of gravel pack around pipe (m)	150	150	Concrete pipe: No gravel; PVC: limestone chunks	150	150	150
Geofabric/Exclusion layer	Black plastic top	Black plastic top	PVC & concrete: black plastic top; EcoBloc: geofabric wrap	Geofabric wrap	Geofabric wrap	Black plastic top
Pump well internal diameter	800 mm concrete (year 2000); 1000 mm fibreglass (year 2017); ~400 mm PVC or PE (year 2024).	DN 300 mm Class 12 PVC	800 mm concrete (for PVC bore screen & EcoBloc); 150 mm PVC for concrete bore screen;	450 mm U-PVC DN9	450 mm U-PVC DN9	Fibreglass cylinder (1980s); 1000 mm ID ferro cement cylinder (newer galleries)
Sump depth (m BPB)	0 (year 2000); 0.3 (year 2017); ~1.2 (year 2024)	0.3	0.15	1.8	1.8	0.3 (year 1980s)
Pipe or foot valve depth (m BPB)	0.2	0.2	0.2	0.5	0.5	0.2
Single, straight-pipe galleries (SSP) or branched networks	SSP with 2 pumping wells); year 2024 installs will be SSP with central pumping well	2 U-shaped galleries (pumping wells on corners); 1 SSP with 1	SSP with single pumping well	SSP, central pumping well	SSP, central pumping well	SSP with central pumping well. 2 branched (cross & tee)

Island (Country) / Component	Kiritimati (Kiribati)	Lifuka (Tonga)	Aitutaki (Cook Islands)	Nanumea (Tuvalu)	Vaitupu (Tuvalu)	Bonriki (Kiribati)
		pumping well				
Pipes parallel or perpendicular to the shoreline	Parallel	Parallel	Parallel	Parallel	Parallel	Mixed
Gallery on private or public land?	Public	Public	Private	Public	Private	Private
EC of extracted water (μS/cm)	1200-1400	n/a	n/a	n/a	n/a	n/a

n/a – not applicable or unreported; m BPB = metres below pipe base.

Table 5 presents information, albeit with fewer details relative to Table 4, for other Pacific islands with infiltration galleries that were not extensively discussed during the PGGKE workshop.

Table 5. Pacific islands with infiltration galleries in coral sands (T. Falkland, personal communication during the PGGKE workshop, 1-8 November 2023).

Country	Atoll/Island /State/City	Island/ Freshwater lens	No. of galleries	Type of pipe	Length of pipe (m)	No. of pump wells per gallery	Comments
Federated States of Micronesia	Chuuk State	Piis- Paneu	1	100 mm (slotted PVC)	40	2	-
Kiribati	North Tarawa	Taborio	1	100 mm (slotted PVC)	100	1	-
	Outer islands	n/a	n/a	100 mm (slotted PVC)	n/a	1	-
Marshall Islands	Majuro city	Laura	6	100 mm (slotted PVC)	75 - 90	1	-
	Kwajalein Atoll	Kwajalein	7	Various	90-950	n/a	Hunt and Peterson (1980)
		Roi-Namur	3	n/a	One pipe 900, two pipes 90	n/a	Gingerich (1996)

n/a – not applicable or unreported.

4. Conceptual Model

A conceptual hydrogeological model describes the key features of a groundwater system of relevance to the movement of groundwater and water-borne constituents where this is relevant. Conceptual models are necessary precursors to the construction of groundwater models because they outline the geometry, hydraulic properties and stresses of the system, linking those to sources of information. Here, we describe conceptual models of infiltration galleries in Pacific islands, with a general focus on the conditions encountered on Kiritimati Island (Kiribati). The sources of the chosen parameter ranges are given in the preceding sections.

4.1 Hydrogeological characteristics of atoll islands

4.1.1 Aquifer hydraulic parameters

The current study adopts a two-layer representation (Holocene and Pleistocene layers) of the island geology. Any layering of hydraulic properties within the Pleistocene sediments is neglected, as is the existence of a reef-flat plate in the Holocene layer.

A base case simulation is defined that is meant to reflect typical atoll island parameters, with values that tend towards those encountered on Kiritimati Atoll, at least where parameters are known. The conceptual models adopted here are not meant to simulate a particular geographical location, and rather, are meant to offer general guidance on infiltration gallery design, operation and interactions with the host aquifer. Table 6 lists the aquifer hydraulic properties adopted within the modelling base case (Case B) of the current study. These were taken from the review of atoll islands by Werner et al. (2017).

Table 6. Aquifer hydraulic properties used in this study.

Layer		Thickness (m)	K_x (m/d)	K_z/K_x (-)	n (-)	S_y (-)	α_L (m)	α_V (m)	α_T (m)
Holocene sediment	Range	5-50	15-80	1:1 to 1:10	0.2-0.25	0.15-0.3	0.02-50	0.01-1	0.001-1
	Base case	10*	10	1:10	0.3	0.3	0.1	0.001	0.005
Pleistocene limestone	Range	n/a	173-5000	1:1 to 1:100	0.01-0.3	0.15-0.3	0.02-50	0.01-1	0.001-1
	Base case	40	500	1:10	0.3	0.3	0.1	0.001	0.005

*Depth of unconformity (*d*) is assumed to be 10 m below the land surface.

The base case scenario of the current study adopts a recharge rate (R) of 400 mm/y, equivalent to 40% of the mean annual rainfall 1000 mm/y that was assumed for Kiritimati Atoll (White et al., 2007). This aligns with the recharge ranges reported by Werner et al. (2017), and the value arising from recharge analyses by Falkland (1992). The recharge value of 400 mm/y is lower than the mid-value from atoll island investigations from across the Pacific (see Table 1) because Kiritimati Atoll has a lower rainfall than most other Pacific islands where infiltration galleries have been installed. However, the ratio of recharge-to-rainfall of 40% is higher than the value recommended by Falkland and Woodroffe (1997) of 10-25%, likely because regions where infiltration galleries are installed have been largely cleared of coconut trees, thereby increasing the recharge in those areas (Morrison and Woodroffe, 2009).

In simulations involving freshwater-saltwater interactions, recharge occurs at a salt concentration of zero for simplicity. Values of the groundwater salinity from the model can easily be corrected through simple mixing equations where the simulated salinity is increased to account for a higher recharge salinity (accounting for the evapo-concentration of the rainwater salinity) than the model value of zero. Taking the seawater TDS as 35,000 mg/L, we can determine the groundwater TDS in the model from:

$$T_g = T_r + C(T_s - T_r) \tag{3}$$

Here, T_g is the TDS of the groundwater (in the model), T_s is the TDS of seawater, T_r is the TDS of recharge, and C [-] is the model-based relative salinity, where $C = 1$ ($T_g = T_s = 35{,}000$ mg/L) represents seawater and $C = 0$ ($T_g = T_r$) is the recharge salinity. The conversion of model salinities to field salinities (TDS) using Equation (3) is necessary to assess whether saltwater-freshwater mixing in the model is a reasonable reproduction of the conditions in atoll island infiltration galleries, particularly on Kiritimati Atoll.

The most challenging part of applying Equation (3) is the approximation of the recharge salinity (T_r), which requires an assessment of the evapo-concentration of rainfall salts (see Section 2.2.2). In comparing model salinities to those of Kiritimati Island, we tested T_r values ranging from 300 to 500 mg/L. The upper limit adopted here is higher than the range (45-450 mg/L) estimated in Section 2.2.2, and is also higher than the upper bound (450 mg/L) suggested by Post et al. (2018) for Bonriki Island. The choice of 500 mg/L as the upper limit accounts for: (a) uncertainties in previous methods of estimating the recharge salinity, (b) the lack rainfall salinity measurements in the Pacific, and (c) the lower rainfall of Kiritimati Atoll relative to Bonriki Island.

4.2 Infiltration gallery layout

The infiltration gallery layouts (single pipes that are parallel or perpendicular to the shoreline, and branched pipes) are visually represented in cross-sectional schematics in Figure 8. All three layouts were considered in numerical simulations of infiltration gallery performance. In Figure 8a, the abstraction well is located centrally within the infiltration gallery, whereas the abstraction well is positioned at the end of infiltration galleries in Figures 8b and 8c. The abstraction well is installed at various locations within the known infiltration galleries of the Pacific, including some cases where two abstraction wells are used (e.g., one at each end of the horizontal pipe; Kiritimati Atoll).

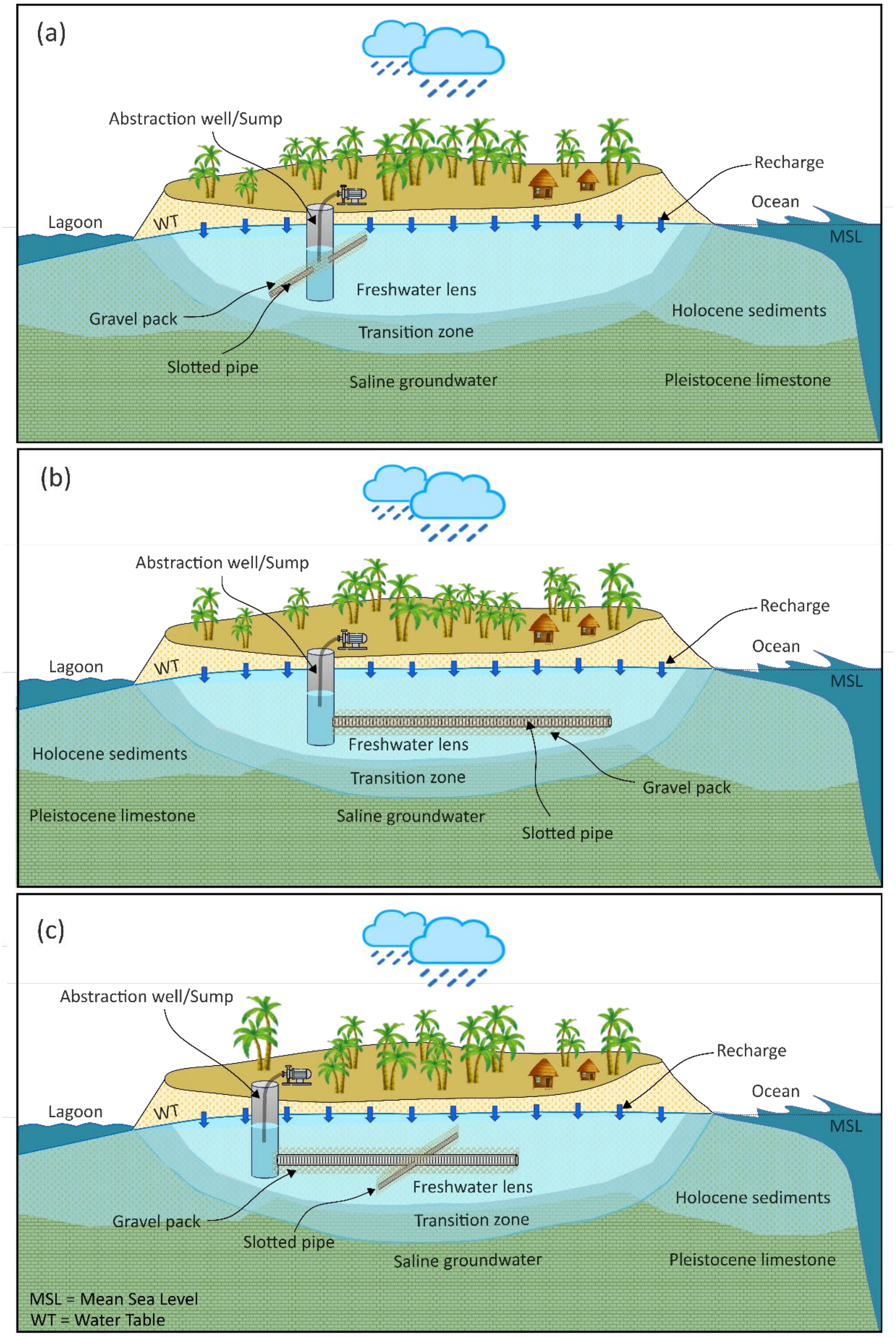

Figure 8. Conceptual diagrams of infiltration gallery layouts in Pacific atoll islands, including: (a) a single horizontal slotted pipe parallel to the shoreline, (b) a single horizontal pipe perpendicular to the shoreline, and (c) a horizontal, branched slotted pipe network that combines (a) and (b). WT refers to the water table, and MSL indicates mean sea level.

4.3 Infiltration gallery parameters

In this section, the hydraulic conductivity (K) values and dimensions of the components of the infiltration gallery (i.e., plastic/geofabric layer, gravel pack and slotted pipe) are characterised based on literature sources. The model parameters for each component are then incorporated into the groundwater models to facilitate the simulation and analysis of infiltration galleries.

4.3.1 Plastic/geofabric layer and gravel pack

The method of construction of some infiltration galleries in the Pacific has included the placement of a plastic sheet above the top of the gravel pack to exclude overlying, fine material from mixing with the gravel pack (Figure 6b). In this way, the plastic sheet acts as an exclusion layer. Materials commonly employed in construction and building projects (builder's plastic) are used, with typical thickness of 2 to 3 mm (https://protectivefilm.com.au). The intention is to avoid fine sediment reaching the pipe, where it can block the pipe slots and/or enter the pipe causing the extracted water to carry suspended sediment. Plastic layers overlying the gravel pack are employed in the construction of infiltration galleries on Kiritimati Atoll, Lifuka Island, Aitutaki Island and Bonriki Island (see "Infiltration gallery" in Table 4). The plastic sheet is assumed to have a thickness of 3 mm and width of is 1 m (t_p and w_p, respectively; see Figure 6b) in the current study. The impermeable nature of the plastic layer requires a near-zero hydraulic conductivity (K_{pl} [LT^{-1}]) in numerical models. A minute value of 4.9×10^{-8} m/d was selected for K_{pl} in numerical models that was chosen, after some model testing, to avoid numerical convergence issues.

In some atoll islands, geofabric has been employed as an alternative to the plastic layer (e.g., Aitutaki Island) or is being contemplated for use in the construction of forthcoming infiltration galleries on Nanumea and Vaitupu Atolls (see "Infiltration gallery" in Table 4). Geofabric is a synthetic material used to hold back fine material from mixing with gravel packs and reaching the pipe (Figure 6c), thereby preventing clogging of the pipe slots. The thickness of geofabric (t_g) used in infiltration gallery designs was presumed to range from 0.5 to 3 mm (https://industrialplastics.com.au/geotextile/), while the hydraulic conductivity (K_{gf} [LT^{-1}]) typically falls in the range 122 m/d to 321 m/d (www.water-pollutionsolutions.com), as obtained from laboratory measurements by the manufacturer using standard methods (e.g., ASTM D4491/D4491M-22; https://www.astm.org/d4491_d4491m-22.html). In this study, a value of 265 m/d was chosen for K_{gf}, and while t_g was set to 3 mm.

Various approaches can be employed to estimate the hydraulic conductivity of the gravel pack (K_g [LT^{-1}]). For example, K_g can be inferred from the grain-size distribution. As gravel is often sorted prior to its use in infiltration gallery installations, information on grain sizes ought to be available. The Kozeny-Carman equation (Bear, 1972) is a common approach for approximating the hydraulic conductivity from the grain-size distribution, also requiring the porosity and the properties of the fluid (water in this case). The Kozeny-Carman equation is (Bear, 1972):

$$K_g = \frac{\rho g n^3 d_m^2}{180\mu(1-n)^2} \quad (4)$$

where μ [$ML^{-1}T^{-1}$] is the freshwater dynamic viscosity (typically 10^{-3} Pa.s) and g [LT^{-2}] is gravity (9.8 m/s^2). Porosity (n) can be determined from rudimentary laboratory testing, including the water saturation method (Fetter, 2001), with typical values for gravel being 0.24 to 0.44 (Morris and Johnson, 1967). The mean grain size (d_m [L]) can be calculated from a grain-size distribution if this is known, as: $\log_2 d_m = (\log_2 d_{16} + \log_2 d_{50} + \log_2 d_{84})/3$, where d_{84}, d_{50} and d_{16} are grain diameters (obtained from the grain-size distribution) at which 84%, 50% and 16% (respectively) of the sample's mass comprises finer particles. Otherwise, an approximate value of d_m for the gravel pack can be adopted in lieu of particle-size analysis.

In the absence of grain-size data for gravel pack material used in the Pacific, Domenico and Schwartz (1990) provide typical values for gravel of 26 m/d to 2592 m/d. In this study, a value of 2592 m/d was selected for K_g, which falls at the upper end of expected values because gravels used on atoll islands are generally large-grained, typically ranging from 6 mm to 10 mm (see "Infiltration gallery" in Table 4). Applying the Kozeny-Carman equation (Equation 4) to the specified grain size range and porosity within the range of 0.24 to 0.44 yields a hydraulic conductivity (K_g) ranging from 4050 to 127,800 m/d.

4.3.2 Slotted pipes

The inflow of water into slotted pipes is influenced by the nature of the slots. Research into the flow through slotted pipes refers to the hydraulic conductivity (K_{sp} [LT^{-1}]) and porosity (n_s [-]) of the pipe wall. As these parameters are more commonly applied to the flow in natural porous media, some explanation of their application to the flow through slotted pipe walls is needed. K_{sp} has a similar meaning to the hydraulic conductivity of soils, representing the coefficient of proportionality between the head drop across the pipe wall and the rate of flow through a unit area of slotted pipe wall. n_s is simply the ratio of the void area (i.e., the surface area of slots) to a unit area of slotted pipe wall.

The perforations of slotted pipe may be orientated in various ways relative to the longitudinal axis of the pipe. The most common slot orientation is perpendicular to the pipe longitudinal axis, as shown in Figure 9 ("radial slots"). Alternatively, the slots may be parallel to the pipe's longitudinal axis ("longitudinal slots). A variety of other slot types are available within commercial slotted-pipe options, including ribbed agricultural pipe, etc.

Values of K_{sp} can be obtained using laboratory testing and/or theoretical analysis of the hydraulics of flow through the slots. The latter requires knowledge of the geometric configuration of the slots. One common slotted-pipe configuration is illustrated in Figure 9, which shows a series of slits of width (slot aperture) w_s [L] and slot length L_s [L]. The pipe has an outer diameter of D_o [L], an inner diameter (or "nominal bore") of D_i [L], and thus a wall thickness of $(D_o - D_i)/2$ (= t_w [L]). Considering for the purposes of illustration a pipe in its traditional vertical orientation, each slit is vertically offset from the next (slot longitudinal spacing) by a distance of S_2 [L], over which the casing is intact. A total of N_s slots are arranged uniformly around the circumference of the pipe, each separated by a radial spacing of S_1 [L], as shown in Figure 6.

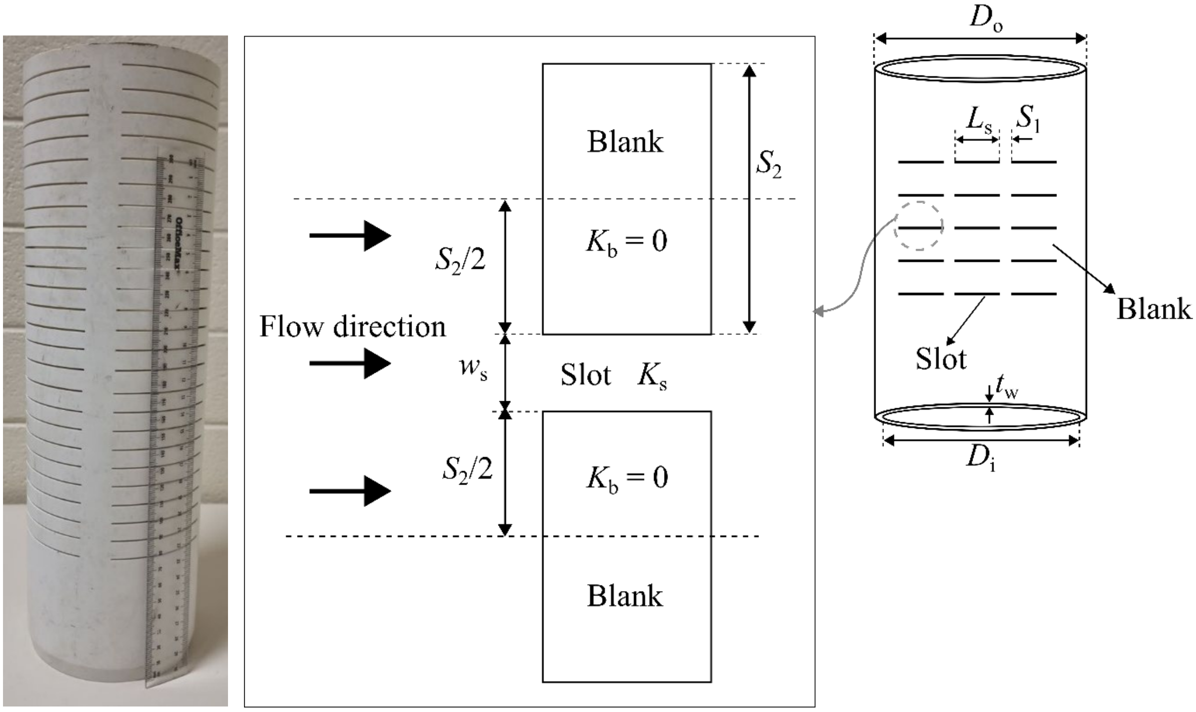

Figure 9. Slotted-pipe configuration for radial-slot arrangements.

Slotted pipes of type 150 PN9 UPVC and 100 PN9 UPVC (DEPS, 2023) were adopted for the modelling analysis described in the subsequent section as these types of pipes are commonly utilised in infiltration galleries in the Pacific (see "Infiltration gallery" in Table 4). The properties of these, as documented by the manufacturer, are provided in Table 7. A calculation of the pipe wall porosity (n_p) is provided, calculated as the slotted area of pipe wall ($w_s L_s N_s$) divided by the corresponding pipe wall area containing the slots ($\pi D_o(w_s + S_2)$).

Table 7. Properties of slotted pipe (DEPS, 2023) adopted in numerical models of the current study.

Parameter	Pipe type:	
	150 PN9	**100 PN9**
Outer diameter of PVC pipe, D_o (mm)	160.25	114.3
Inner diameter of PVC pipe, D_i (mm)	146.85	104.6
Wall thickness of PVC pipe, t_w (mm)	6.7	4.85
Slot length, L_s (mm)	50	50
Slot opening width (aperture), w_s (mm)	0.8	0.8
Slot longitudinal spacing, S_2 (mm)	10	10
Number of slots within the circumferences of the pipe, N_s (-)	4	4
Pipe wall porosity*, n_p (%)	2.94	4.13

*Calculated as $\left((w_s L_s N_S)/\left(\pi D_o \left(w_s + S_2\right)\right)\right) \times 100$.

In previous studies (e.g., Barrash et al., 2006), the flow through pipe slots is treated as analogous to flow through fractured media. The flow through an individual slot is obtained using equations for flow through a fracture between two smooth parallel plates, employing formulae such as that presented by Witherspoon et al. (1980), as:

$$K_s = \frac{w_s^2 \rho g}{12\mu} \tag{5}$$

Equation (5) is a precursor to the so-called cubic law (Zimmerman and Bodvarsson, 1994), which is obtained by multiplying by w_s to obtain the slot transmissivity. Each slot and the blank space between it can be considered as two layers in a parallel stratified media, allowing the equivalent hydraulic conductivity (K_{eq} [LT^{-1}]) to be calculated using the following formula (e.g., Wiener, 1912):

$$K_{eq} = \left(\frac{\sum_{i=1}^{N} t_i K_i}{\sum_{i=1}^{N} t_i} \right) \tag{6}$$

where, N [-] is the number of layers (here, N = 3 and the layers are solid casing, slot, pipe casing; Figure 9), t [L] and K [LT^{-1}] are the thickness and hydraulic conductivity of each layer (respectively), with the subscript i indicating the specific layer number. Utilising Equation (6) for a slot with the thickness of w_s (i.e., slot aperture width) and hydraulic conductivity of K_s (calculated by Equation (5)) and two impermeable blanks with hydraulic conductivity of zero (K_{bl} = 0 m/s) and the thickness of $S_2/2$ each side of the slot aperture (Figure 9), yields an equivalent hydraulic conductivity for the combination of slot and blank (K_{sb}) of:

$$K_{\mathrm{sb}} = \left(\frac{K_{\mathrm{b}}\frac{S_2}{2} + K_{\mathrm{s}} w_{\mathrm{s}} + K_{\mathrm{b}}\frac{S_2}{2}}{\frac{S_2}{2} + w_{\mathrm{s}} + \frac{S_2}{2}} \right) = \frac{K_{\mathrm{s}} w_{\mathrm{s}}}{w_{\mathrm{s}} + S_2} \tag{7}$$

The hydraulic conductivity of slotted pipe (K_{sp}) then can be calculated by upscaling K_{sb} by the ratio of circumference of screen slot to circumference of the pipe (e.g., Snow, 1968; Moench, 1984) as:

$$K_{\mathrm{sp}} = \left(\frac{K_{\mathrm{s}} w_{\mathrm{s}}}{w_{\mathrm{s}} + S_2} \right) \left(\frac{N_{\mathrm{s}} L_{\mathrm{s}}}{\pi D_{\mathrm{o}}} \right) \tag{8}$$

More recently, Bayer-Raich et al. (2022) conducted an in-depth analysis of well screen head loss using numerical models. Their study involved the coupling of Darcy's law, applied to the aquifer and filter/gravel pack, with turbulent flow within the well and through the screen at the sub-millimetre scale. This investigation encompassed four different well screen types, including louver, slotted, bridge and wire wrap screens. The outcome of their research has led to the development of a new empirical formulation for quantifying screen head loss. According to numerical simulations conducted by Bayer-Raich et al. (2022), the screen head loss (S_{sc} [L]) can be calculated as follows:

$$S_{\mathrm{sc}} = \frac{1}{2g} \left(\frac{v_{\mathrm{sc}}}{C_0} \right)^2 + B_0 \frac{v_{\mathrm{sc}}}{K_{\mathrm{g}}} \tag{9}$$

where C_0 [-] and B_0 [L] are constant values obtained using the least-square method on the numerical results. Bayer-Raich et al. (2022) found a single constant value for C_0 equal to 0.135, which is applicable for all screen types. However, the values for B_0 vary for different screen types as B_0 = 0.66 mm (wire warp), B_0 = 4.27 mm (louver), B_0 = 2.25 mm (bridge), B_0 = 1.14 mm (slotted). These values of C_0 and B_0 have been found to effectively replicate the screen head loss observed in Bayer-Raich et al.'s (2022) numerical experiment. In Equation (9), the variable v_{sc} [LT^{-1}] represents screen entrance velocity or average water velocity through well screen, which is defined as:

$$v_{\mathrm{sc}} = \frac{Q_{\mathrm{p}}}{\pi D_{\mathrm{o}} n_{\mathrm{p}}} \tag{10}$$

where Q_p [L^{2}T^{-1}] is the pumping rate per screen unit length (= Q/L_p, here, Q [L^{3}T^{-1}] is the pumping rate and L_p [L] is the screen pipe length) and n_p is the pipe wall porosity, calculated as $\left(w_{\mathrm{s}} L_{\mathrm{s}} N_{\mathrm{s}}\right) / \left(\pi D_{\mathrm{o}} \left(w_{\mathrm{s}} + S_2\right)\right)$.

By employing B_0 = 1.14 mm (for slotted) in Equation (9) and calculating head loss through the slotted pipe (S_{sc}), one can estimate the surrogate hydraulic conductivity (K_{sp}) and conductance (C_{sp} [L^{2}T^{-1}]) of the slotted pipe using Darcy's law as follows:

$$K_{\mathrm{sp}} = \frac{v_{\mathrm{sc}} t_{\mathrm{w}}}{S_{\mathrm{sc}}} \tag{11}$$

$$C_{\mathrm{sp}} = \frac{Q_{\mathrm{p}}}{S_{\mathrm{sc}}} \tag{12}$$

Based on the parameters outlined in Table 7, the hydraulic properties of the slotted PVC pipes have been calculated using Barrash et al.'s (2006) and Bayer-Raich et al.'s (2022) methods and are summarised in Table 8.

Table 8. The hydraulic properties of the slotted PVC pipes (150 PN9 UPVC and 100 PN9 UPVC), characterised as per Table 7, determined by Barrash et al.'s (2006) and Bayer-Raich et al.'s (2022) methods.

Method	**Equations**	**K_{sp} (m/d)**	
		150 PN9	**100 PN9**
Barrash et al. (2006)	(5)*and (8)	1220	1710
Bayer-Raich et al. (2022)	(9)**, (10)*** and (11)	15,060	10,902

*In Equation (5), it is assumed that ρ = 1000 kg/m^3, g = 9.81 m/s^2 and μ = 10^{-3} Pa.s.
**In Equation (9), it is assumed that K_{g} = 2592 m/d, C_0 = 0.135 and B_0 = 1.14 mm (for slotted pipe).
***In Equation (10), $Q_{\mathrm{p}} = Q/L_{\mathrm{p}}$, where it is assumed that Q = 20 m^3/d and L_{p} = 100 m.

In this study, the Bayer-Raich et al.'s (2022) method was chosen to calculate the hydraulic conductivity of the slotted pipe (K_{sp}), and a value of 15,060 m/d was employed as the K_{sp} value in the base case model (see Section "6. Modelling Scenarios").

4.3.3 Hydraulic conductivity along slotted pipes

The horizontal slotted pipe can be implicitly simulated in the groundwater model using a method known as the high-*K* approach. This approach is designed to represent the limited resistance to flow within the slotted pipe, instead of attempting to simulate pipe flow explicitly (requiring application of nonlinear equations that are more challenging to solve than Darcy's Law) in the groundwater model. This is achieved in part, by assigning a very high hydraulic conductivity to the slotted pipe region in the model. The high-*K* approach has been successfully applied in previous studies to represent surface water bodies (e.g., Jazayeri et al., 2021) and flow in karst aquifers (e.g., Kuniansky, 2016).

To estimate the equivalent hydraulic conductivity (K_{p}) along the slotted pipe in the groundwater model, Darcy's law can be applied. The head loss and average velocity within the slotted pipe are first obtained from classical pipe hydraulics theory (adopted to account for the effects of slots on flow in the pipe). That is, the head loss in the slotted pipe (h_{l} [L]) can be calculated using the Darcy-Weisbach formula (e.g., White, 2016) as:

$$h_{\mathrm{l}} = f_{\mathrm{s}} \frac{L_{\mathrm{p}}}{D_{\mathrm{i}}} \frac{v_{\mathrm{p}}^2}{2g} \tag{13}$$

where v_p [LT^{-1}] is the average velocity within the pipe and f_s [-] is a friction factor related to the hydraulic shear force along the internal pipe wall. Siwon (1987) developed a relation to estimate f_s for a slotted PVC pipe as:

$$f_{\mathrm{s}} = f_{\mathrm{p}} + f_{\mathrm{a}} \tag{14}$$

where f_p [-] and f_a [-] are friction factors for perforations and for unslotted pipe, respectively. f_p can be calculated as $0.0106 \times n_p^{0.413}$. Here, n_p is the pipe wall porosity. f_a is given by Altshul and Kishelev (1975) as:

$$f_{\mathrm{a}} = 0.11\left(\frac{68}{Re} + \varepsilon\right)^{0.25} \tag{15}$$

with $\varepsilon = \varepsilon_{\mathrm{s}} + 0.282 n_{\mathrm{p}}^{2.4}$ for $Re > 3400$. Re [-] is Reynolds number ($= \rho v_p D_i / \mu$), and ε_s [-] is the relative roughness of the pipe without perforations. If the perforation density is less than 1%, the porosity term (n_p) in calculating ε is dropped. A more accurate function for finding f_a is given by Chen (1979) and Ouyang and Aziz (1996) as:

$$\frac{1}{\sqrt{f_{\mathrm{a}}}} = -2\log\left[\frac{\varepsilon}{3.7065} - \frac{5.0452}{Re}\log\left(\frac{\varepsilon^{1.1098}}{2.8257} + \frac{7}{Re^{0.8981}}\right)\right] \tag{16}$$

Siwon's (1987) uses the following equation to calculate the head loss through the perforated pipe (h_l) as:

$$h_l = \left(\frac{f_{\mathrm{s}}}{D_{\mathrm{i}}}\frac{\rho v_{\mathrm{p}}^2}{2} + \frac{2}{D_{\mathrm{i}}}\beta v_{\mathrm{p}}^2 (1+\eta)\frac{n_{\mathrm{p}} v_{\mathrm{s}}}{v_{\mathrm{p}}}\right)\rho g L_{\mathrm{p}} \tag{17}$$

where v_s [-] is the mean velocity through slots (i.e., flow rate (Q) divided by the total slot aperture area). $\beta(1+\eta)$ can be calculated from the following equation (Clemo, 2006):

$$\beta(1+\eta) = 1.05\left[1 + \frac{1.175}{\left(b\frac{v_{\mathrm{p}}^2}{v_{\mathrm{s}}^2} + 1.253\right)^2}\right] \tag{18}$$

and b [-] is (Clemo, 2006),

$$b = \frac{10}{\left(10^3 n_{\mathrm{p}}\right)^{4.2}} + \frac{4}{10^7} \tag{19}$$

By calculating h_l using Equation (17), the equivalent hydraulic conductivity along the slotted pipe (K_p) can be calculated by Darcy's law as follows:

$$K_{\mathrm{p}} = \frac{v_{\mathrm{p}} L_{\mathrm{p}}}{h_{\mathrm{l}}} \tag{20}$$

Based on the properties of the slotted pipe for 150 PN9 outlined in Table 7, the value of K_p for the base case model was calculated using Equations (14) to (20) as 3.5×10^8 m/d, assuming Q = 20 m^3/d, L_p = 100 m and $\varepsilon_s = 1.02 \times 10^{-5}$, where the latter is the relative roughness for unslotted PVC pipe, calculated as the ratio of the surface roughness of unslotted PVC (= 1.5×10^{-3} mm; https://www.pipeflow.com/pipe-pressure-drop-calculations/pipe-roughness) to the internal diameter of the pipe.

5. Model Design Elements

5.1 Overview of modelling strategy

The modelling strategy undertaken in this study is summarised in Figure 10. The background data is provided in Sections 2 and 3, while Section 4 describes relevant conceptual model elements. The current section describes the conversion of the conceptual model into numerical representations within groundwater models.

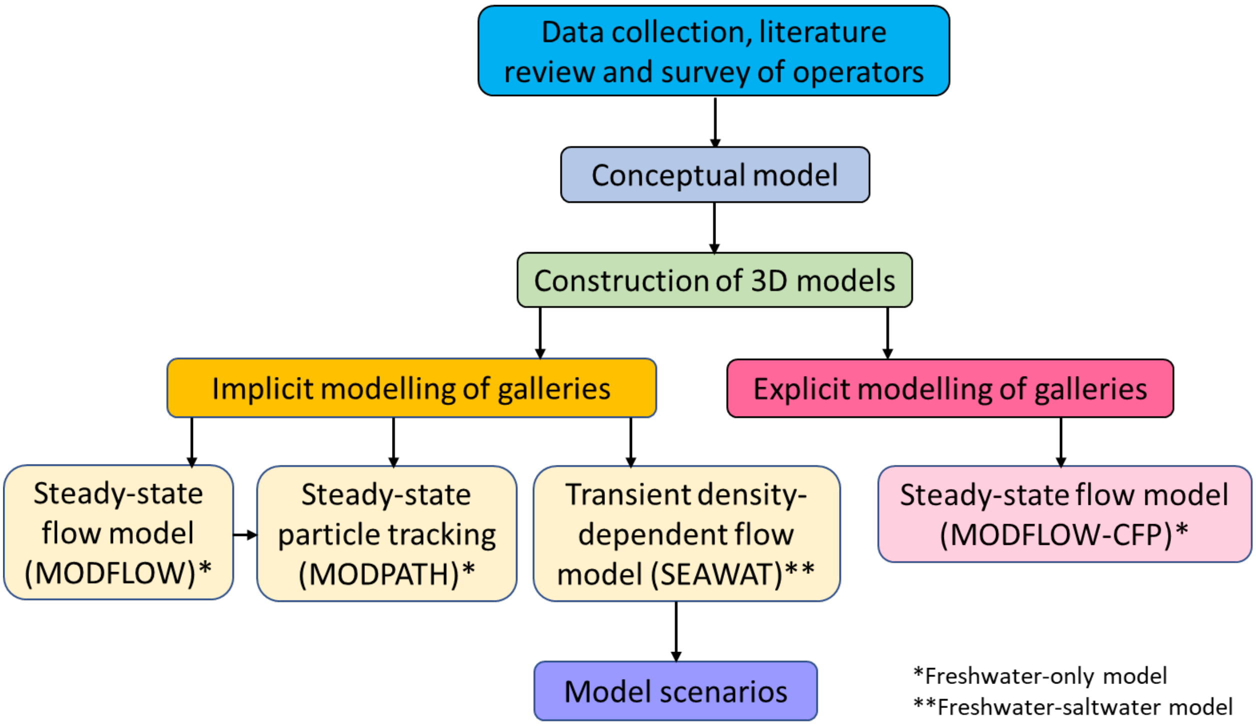

Figure 10. Model development sequence.

Steady-state simulations of density-independent flow (saltwater was neglected) were undertaken to evaluate the hydraulic behaviour of the various components of infiltration galleries using models that were faster to run and avoided the complications of density effects. These simulations encompassed both implicit (MODFLOW) and explicit (MODFLOW-CFP) approaches for simulating infiltration galleries, along with particle tracking.

Transient simulations were adopted in simulating density-dependent flow conditions, partly because SEAWAT is not able to obtain a steady-state result when density effects are considered, but also, it was useful to observe the timing of changes from the initial conditions (prior to construction of infiltration galleries) caused by pumping. Model scenarios explore the effects of changing hydrogeological parameters and infiltration gallery components on the salinity of the produced water and the condition of the lens.

5.2 Modelling codes

In the initial phase of this study, the numerical modelling code MODFLOW (Harbaugh, 2005) was employed to investigate the flow dynamics within an ideal atoll aquifer that included an infiltration gallery, comprising a single horizontally slotted pipe aligned parallel to the shoreline. The pipe was connected to a single abstraction well, as shown in Figure 8a. MODFLOW, developed by the USGS (United States Geological Survey), is recognised as the industry-standard code for simulating groundwater flow. The current study uses MODFLOW-2005 v.1.12.00 (Harbaugh, 2005). The slotted pipe and abstraction well were represented implicitly in MODFLOW using high hydraulic conductivity zones (high-*K* approach).

To allow for visualisation and analysis of the groundwater flow field and the zone of influence around the infiltration gallery, MODPATH (Version 7; Pollock, 2016) was used to post-process MODFLOW results. MODPATH is a particle-tracking code that calculates the pathways of groundwater flow, as determined from the specific fluxes of MODFLOW that are converted to velocities by assigning porosity values in MODPATH.

The accuracy of the high-*K* approach used in MODFLOW for horizontal pipes and the pumping well was examined by simulating the horizontal pipe explicitly in MODFLOW-CFP (Shoemaker et al., 2007). MODFLOW-CFP (Conduit-Flow Process) can simulate the flow in pipes (including both laminar and turbulent flow) and the connection between the pipe and the surrounding porous media. This is achieved by coupling the conventional groundwater flow equation of MODFLOW with specific formulations designed for a one-dimensional discrete network of cylindrical pipes. This method allows for the representation of the non-linear equations that govern flow in pipes rather than approximating the pipes as high-*K* features, as we adopted in MODFLOW (and later, SEAWAT). The more accurate evaluation of pipe-flow dynamics in MODFLOW-CFP is therefore a check on our representation of pipes in MODFLOW.

In the second phase of this study, SEAWAT was employed to investigate freshwater-saltwater interactions within atoll islands affected by pumping from an infiltration gallery. SEAWAT is a density-coupled version of MODFLOW (flow) and MT3DMS (solute transport) designed for simulating three-dimensional, variable-density, saturated groundwater flow and solute transport (Langevin et al., 2007). In SEAWAT, the fluid density is determined as a function of one or more solute species. The code utilises a finite-difference approximation to solve the relevant equations. SEAWAT has been tested and applied extensively in groundwater studies, including saltwater intrusion in coastal aquifers and the behaviour of freshwater lenses in atoll islands (Langevin et al., 2007; Post et al., 2018; Werner et al., 2017).

Given that the current version of MODFLOW-CFP lacks variable-density capability (Xu and Hu, 2017), and SEAWAT does not have pipe-flow simulation capability, the only available option for representing pipes in scenarios involving mixed-density water is to adopt SEAWAT with the pipe represented using the high-*K* approach.

5.3 Model domain

Figure 11 presents a series of infiltration galleries arranged parallel to the shoreline, in plan view. L_p [L] is the slotted pipe length, W_1 [L] is the distance between the pipe and the shoreline, W_2 [L] is half of the landward distance (in the *y*-direction) between two adjacent pipes, and L_1 [L] is half of the lateral distance (in the *x*-direction) between two adjacent pipes. We take advantage of axes of symmetry in this arrangement to reduce the problem to only a portion of this configuration, which includes a single horizontal slotted pipe and half of the abstraction well. The red dashed line in Figure 11 represents the region simulated in the base case model (149.5 m in the *x*-direction by 409 m in the *y*-direction; Case B). Assumptions of symmetry allow no-flow boundaries to be employed for the left-hand, right-hand and bottom boundaries of this region in simulations (all four sides of the red rectangle except the shoreline face).

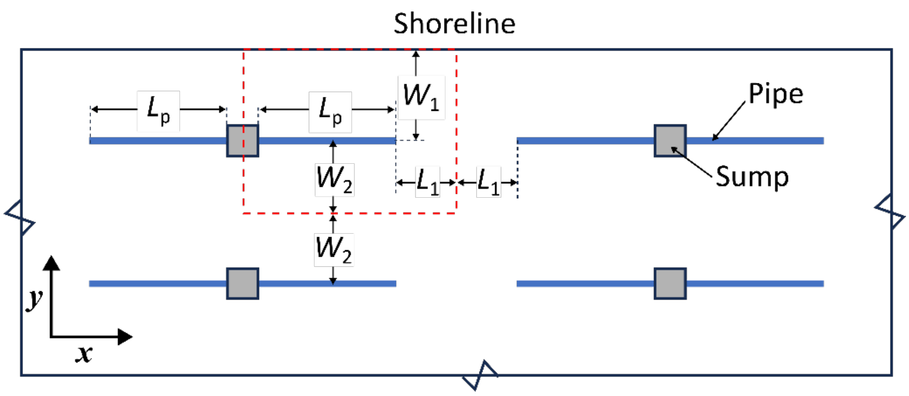

Figure 11. Plan view of a series of infiltration galleries aligned parallel to the shoreline. The red-dashed line delineates the region utilised in simulating the base case model (Case B).

The numerical model domains for three distinct conceptual layouts of horizontal slotted pipes are presented in Figures 12 to 14. The corresponding conceptual models are presented in Figure 8. In Figure 12, the slotted pipe is aligned parallel to the shoreline, while the slotted pipe is perpendicular to the shoreline in Figure 13. Figure 14 shows a branched-pipe configuration.

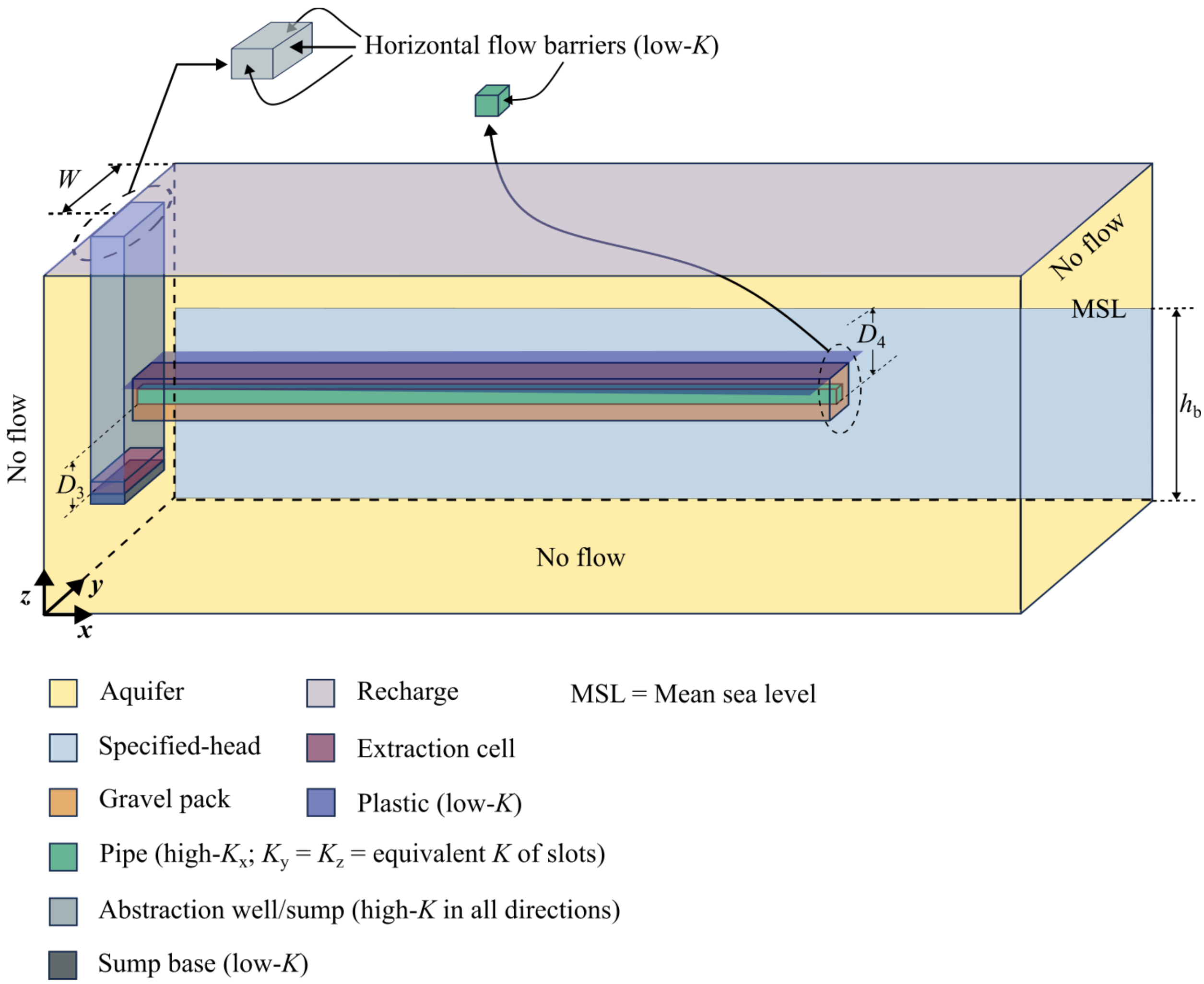

Figure 12. Numerical model domain and boundary conditions for a single slotted pipe aligned parallel to the shoreline, in accordance with the conceptual diagram in Figure 8a. The ocean occurs on the vertical back face of the domain at a depth of h_b, while the other vertical faces are no flow boundaries. "Sump" refers to the abstraction well.

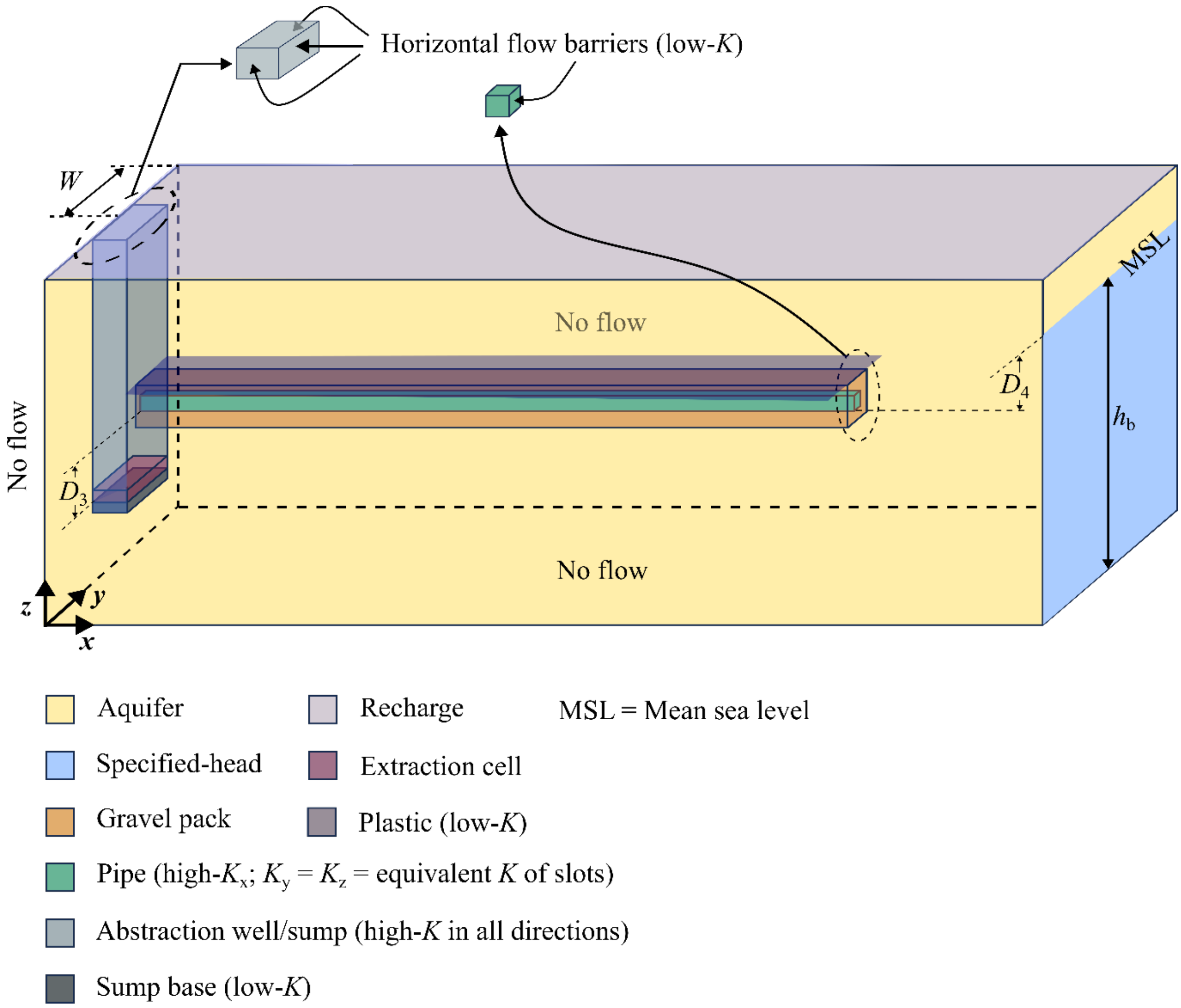

Figure 13. Numerical model domain and boundary conditions for a single slotted pipe positioned perpendicular to the shoreline, in accordance with the conceptual diagram in Figure 8b. The ocean occurs on the vertical right face of the domain at a depth of h_b, while the other vertical faces are no flow boundaries. "Sump" refers to the abstraction well.

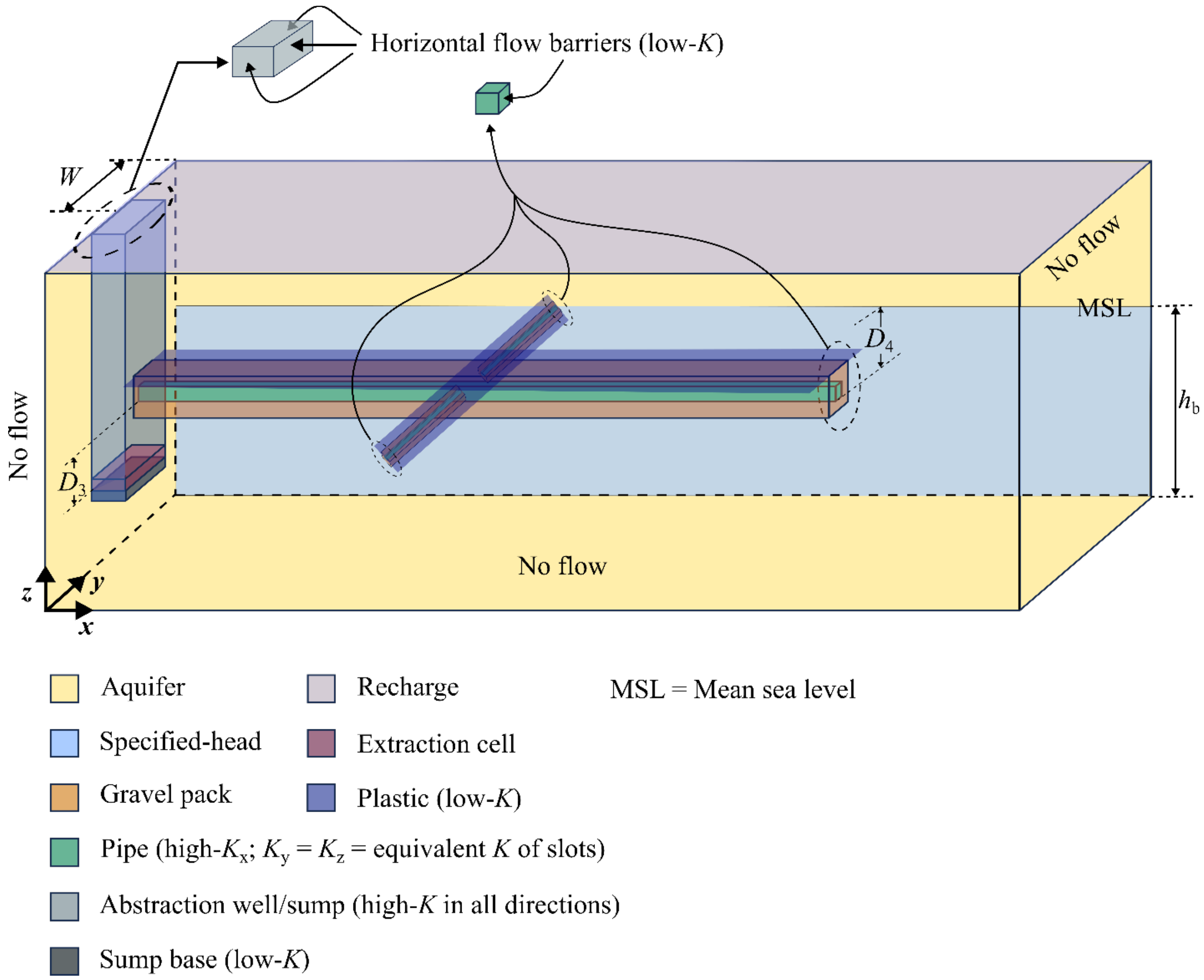

Figure 14. Numerical model domain and boundary conditions for a branched slotted pipe, in accordance with the conceptual diagram in Figure 8c. The ocean occurs on the vertical back face of the domain at a depth of h_b, while the other vertical faces are no flow boundaries. "Sump" refers to the abstraction well.

The model domain is discretised using a rectilinear finite-difference grid. This grid is composed of 114 columns (*NCOL*; in the *x*-direction), 85 rows (*NROW*; in the *y*-direction), and 24 layers (*NLAY*; in the *z*-direction) in the base case model (Case B; see Section 6.1), totalling 232,560 cells. A SEAWAT model with this number of cells is usually associated with long run-times (up to 3 days). The number of columns (*NCOL*), rows (*NROW*) and layers (*NLAY*) are subject to variation in different modelling scenarios (refer to Table B2 in Appendix B for details of each scenario).

The region accommodating the infiltration galley, consisting of the slotted pipe and abstraction well/sump, is assigned the smallest cell sizes. This leads to Δx [L] values ranging from 0.5 to 1 m, Δy [L] values ranging from 0.15 to 0.27 m, and Δz [L] spanning 0.003 to 0.16 m in Case B. Figure 15 visually illustrates the model discretisation for Case B, depicting a single slotted pipe aligned parallel to the shoreline.

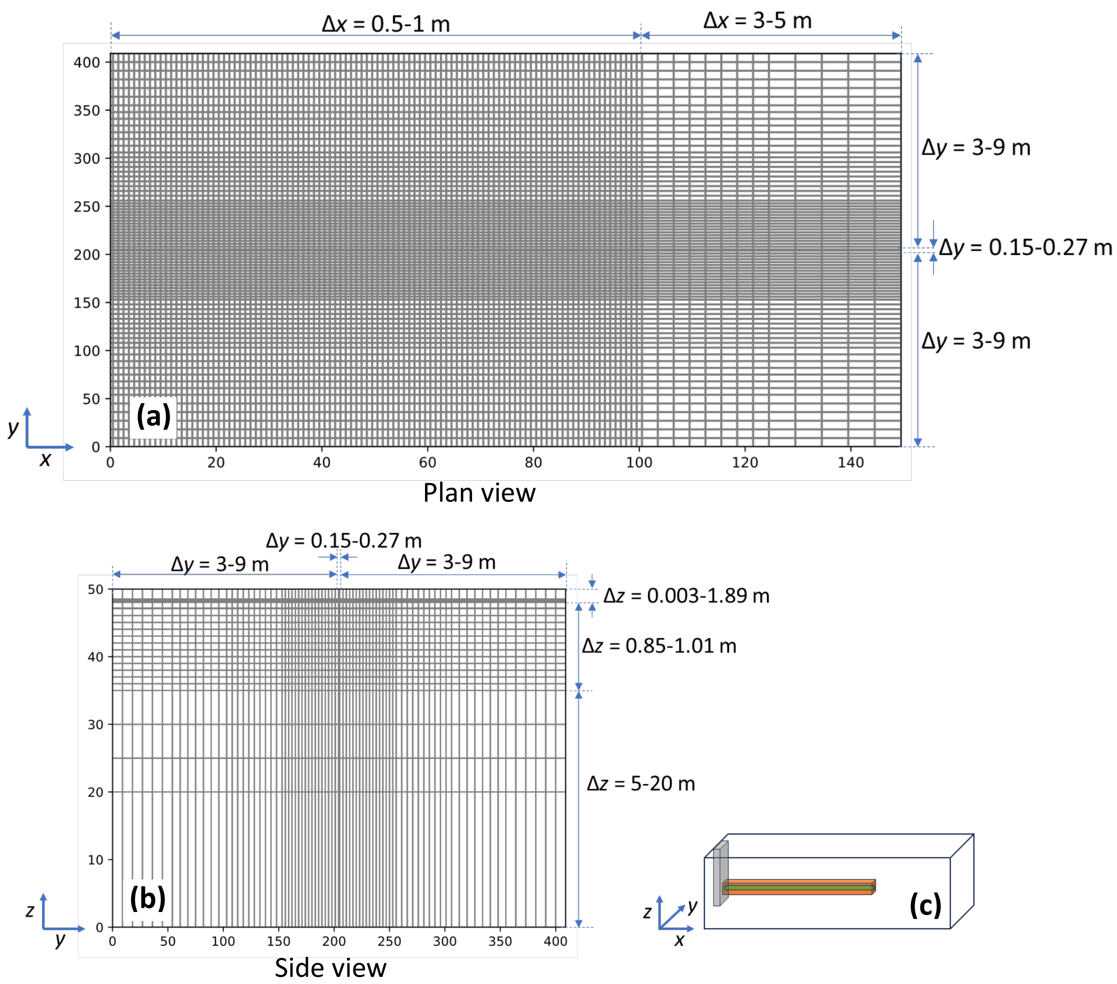

Figure 15. Discretisation of the base case model (Case B; see Section 6.1), where the slotted pipe is aligned parallel to the shoreline, showing (a) plan view (*x*-*y*), (b) side view (*y*-*z*), and (c) 3D model schematic showing the abstraction well/sump and the slotted, horizontal pipe and gravel pack. In (a), the centreline of the horizontal pipe (Case B) is located between (*x*, *y*) = (0.5 m, 204.5 m) to (100.5 m, 204.5 m), while in (b), the centre of the pipe (Case B) occurs at (*y*, *z*) = (204.5 m, 48.28 m).

Freshwater-only models (i.e., MODFLOW and MODFLOW-CFP) adopt a steady-state mode, consisting of one stress period that represents infinite time, thereby providing a result that would arise long into the future with aquifer stresses remaining constant in time. This requires much shorter computation run-times than transient analysis.

SEAWAT models considered transient conditions in both flow and solute transport. This requires establishing the initial conditions for the start of each case. To achieve this, a SEAWAT simulation was carried out without the presence of an infiltration gallery (Case 0). This simulation encompassed one stress period with a duration of 10,000 days (~27.4 years) represented by 1000 time-steps of 10 days duration. The results demonstrated that the duration of 10,000 days for a single stress period was sufficient for the hydraulic head and solute concentration to reach a steady state, as indicated by the total salt mass within the model domain reaching a condition that no longer changed in time. The resultant hydraulic heads and solute concentrations from the steady-state (pre-development) simulation were employed as initial conditions for the simulations involving pumping from an infiltration gallery. Those cases adopted a stress period (i.e., pumping and recharge did not vary over time) of 5,500 days (~15.1 years) comprised of 550 time-steps of 10 days duration. The total salt mass within the model remained stable (in time) by the end of this period, indicating that the models reached steady-state conditions. Models for obtaining initial, predevelopment, steady-state conditions for infiltration gallery simulations required approximately 10 hours to complete each simulation on a 16-core Intel® Core™ i9−129000K processor.

5.4 Boundary conditions

In freshwater-only models (i.e., MODFLOW, MODPATH and MODFLOW-CFP), specified-head cells were employed along one of the vertical faces of the model domain to represent the ocean, as illustrated in Figures 12 to 14 by the light blue coloured region labelled as "Specified-head". The specified-head boundary was set to mean sea level (MSL). In freshwater-only models, density effects were neglected in assigning heads to represent the ocean. Whether this had an effect on the flow field is worth considering in future analyses by comparing to models that adopt depth-dependent heads at the ocean boundary to capture seawater density effects. The other vertical faces of the model domain were set to no-flow boundaries, representing the following axes of symmetry (for the base case model; Figure 12): (a) the left-hand vertical face of the model (*y*-*z* face) bisects the abstraction well such that the stresses either side of this symmetry plane are the same (conceptually), causing the symmetry boundary, (b) the front vertical face of the model (*x*-*z* face) bisects the distance between two parallel galleries , causing a symmetry boundary by assuming that the parallel galleries operate identically, and the effect of the coastal boundary is minimal at the location of this boundary, and (c) the right-hand vertical face of the model domain (*y*-*z* face), which bisects the distance between the ends of two adjacent infiltration galleries, allowing a symmetry boundary on the assumption that the two infiltration galleries operate identically.

In variable-density SEAWAT models, the same boundary conditions as those used in the freshwater-only models were adopted, with the key difference being the assignment of a seawater concentration, C_s [-] (here relative concentration of 1 for seawater and 0 for freshwater (C_f [-]) in SEAWAT models), to the cells with specified-head. The salt concentration of specified-head cells may vary during the simulation depending on the direction of flow into/out of the model. This occurs because seawater enters the model at locations of boundary inflow, while ambient groundwater discharges at locations of boundary outflow (Langevin et al., 2007), leading to changes in salinities at the cells representing the ocean boundary depending on whether flow is to or from the sea. In SEAWAT, the saltwater head (0 m MSL) is converted to equivalent freshwater heads at specified-head boundaries by utilising the initial concentration (i.e., seawater) of the boundary cell. These equivalent freshwater heads remain constant throughout the simulation, regardless of any changes in the concentrations at the boundary due to fresh groundwater discharge (Langevin et al., 2007). This creates a change in the equivalent freshwater head with depth (due to buoyancy) at the ocean boundary, such that the equivalent freshwater head at the Holocene-Pleistocene boundary (-8.5 m MSL) is 0.2125 m MSL and is 1.2125 m MSL at the base of the model (-48.5 m MSL). It follows from this simple calculation, and recognizing the Ghyben-Herzberg relationship, that a head of approximately 0.2125 m MSL is needed for the Holocene sequence to contain only freshwater, at least as an initial estimate.

5.5 Initial conditions

In freshwater-only models (i.e., MODFLOW and MODFLOW-CFP), the initial conditions represent only a starting point for calculations and don't affect the final, steady-state conditions. Using initial conditions that are close to the final steady-state solution can help reduce the computational burden and expedite the convergence of the simulation. The initial heads were therefore set to MSL throughout the model domain. MSL was 1.5 m below ground level (i.e., the top of the model domain) or 48.5 m from the base of the model domain.

A constant saltwater head of 48.5 m and a constant seawater concentration (C_s = 1) were employed as the initial conditions for SEAWAT variable-density models that were used to obtain steady-state conditions prior to the construction of the infiltration gallery. Subsequently, the head and concentration values obtained from these steady-state, pre-development results were employed as initial conditions for the transient SEAWAT simulations that included the infiltration gallery.

5.6 Incorporating the screen (slots) in models

In this study, the numerical model domain was discretised into cells that are rectangular prisms. This required adjustment to model parameters to account for the circular cross section of the slotted pipe. Translation of the circular pipe into the rectilinear model grid is illustrated in the cross-sectional view shown in Figure 16, where the circular pipe is represented in the model using a square cell. The outer boundary of the gravel pack reflects the excavated trench shape, which is usually rectilinear, consistent with the numerical model. In Figure 16, the pipe has an internal diameter of D_i, a wall thickness of t_w, and is surrounded by a gravel pack of thickness t_g. Other components potentially included in this arrangement are the geofabric that may be placed around the gravel and/or a plastic exclusion layer sited above the gravel.

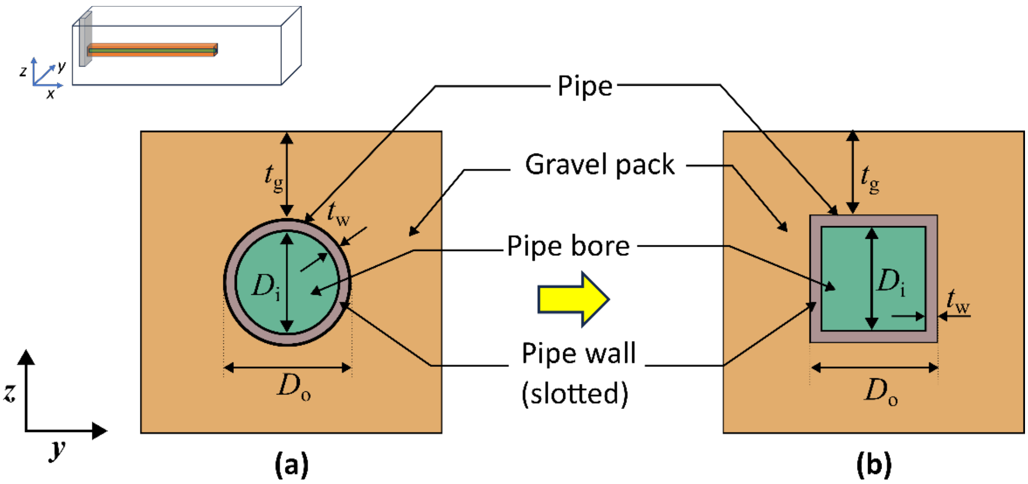

Figure 16. Side view of (a) an infiltration gallery, and (b) its representation within a rectilinear conceptual model.

The simulation of infiltration galleries required the hydraulics of the pipe bore (hollow interior of the pipe), the pipe wall, the gravel pack, and geofabric and/or plastic exclusion layers to be represented in the numerical model. The inclusion of each of these elements required consideration of restrictions to the design and geometry of the model grid. That is, the grids of MODFLOW-based models (including SEAWAT) are limited in terms of differences in the sizes of adjacent model cells; Anderson et al. (2015) recommend that adjacent cells should not vary by more than a factor of 1.5. Following several iterations and a range of model testing simulations, the pipe bore and the wall of the slotted pipe were integrated into a single cell, which had a thickness of $2t_w + D_i$ (equivalent to the external diameter of the pipe (D_o), as shown in Figure 17). The hydraulic conductivity of the integrated-pipe cell in the *y*- and *z*-directions (i.e., perpendicular to the pipe axis, representing flow through the pipe wall perforations) was selected to simulate the connection between the water in the pipe and the gravel pack (K_{ep} [LT^{-1}]), incorporating the hydraulic conductivity of the pipe wall (screen), i.e., K_{sp}. This is illustrated in Figure 17.

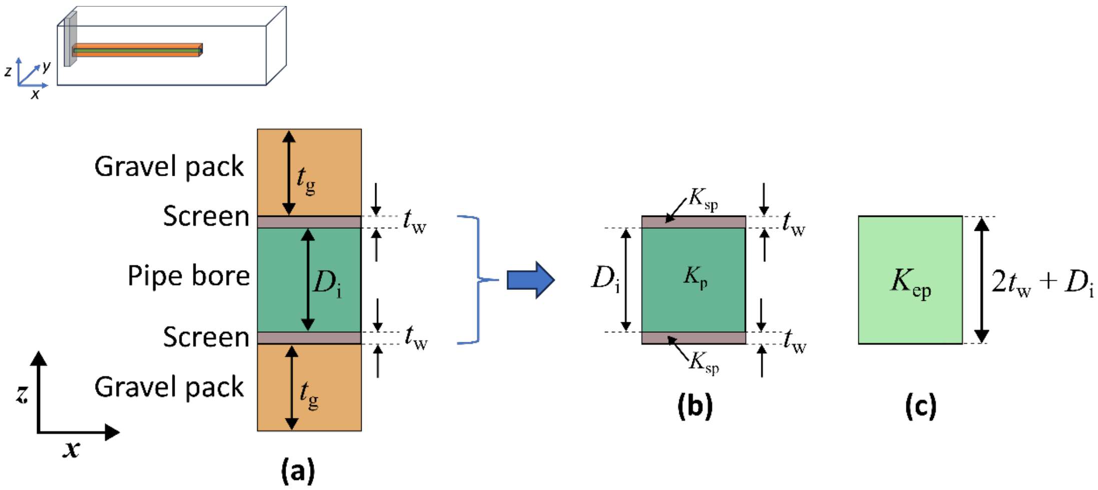

Figure 17. Cross-section of the horizontal pipe of an infiltration gallery, showing the representation of the pipe in a model cell ("Screen" refers to the pipe wall): (a) conceptual model, (b) assignment of parameters to the pipe conceptual model, (c) integrated representation of the pipe bore and screen in the numerical model.

As shown in Figure 17, the combination of screen-pipe-screen (i.e., pipe wall-pipe bore-pipe wall) can be treated as a three-layered, stratified medium for flow in the *y*- and *z*-directions (flow along the pipe axis within the well bore occurs in the *x*-direction). The equivalent hydraulic conductivity of screen-pipe-screen configuration (K_{ep}) can be calculated as (Wiener, 1912):

$$K_{ep} = \frac{2t_w + D_i}{\dfrac{2t_w}{K_{sp}} + \dfrac{D_i}{K_p}} \tag{21}$$

As mentioned previously, the model domain was discretised using rectilinear cells whereas the pipe has a circular shape. This results in a situation where the actual area through which water flows to (and within) the pipe is smaller than the corresponding area in the model grid, as illustrated in Figure 18.

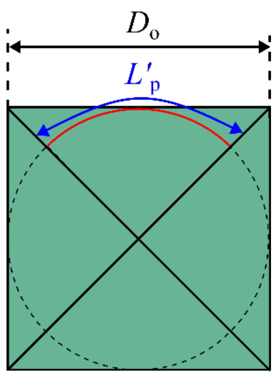

Figure 18. The actual (dashed circle) and modelled (square) cross-section of the pipe, where D_o is the outer diameter of the pipe and L'_p is one-quarter of the pipe perimeter.

The influence of the difference between the circular pipe and the rectilinear cell on groundwater inflow to the pipe can be accounted for by adjusting the effective hydraulic conductivity (K_{ep}) through the ratio of the actual area ($A_{actual} = L'_p \times 1 = \pi D_o/4$, for the unit length of the pipe) through which flow occurs, to the modelled area ($A_{model} = D_o \times 1 = D_o$, for the unit length of the pipe), equal to π/4. Additionally, it is assumed that the head loss from the centroid of the pipe to the internal face of the pipe's wall is negligible. In other words, K_p (Figure 17) is large in the *z*-direction, rendering the term D_i/K_p as essentially zero, allowing it to be omitted from Equation (21). Consequently, the modified K_{ep} in the *z*-directions within cells occupied by the slotted pipe is:

$$K_{ep} = \frac{2t_w + D_i}{\frac{2t_w}{K_{sp}}}\left(\frac{\pi}{4}\right) \tag{22}$$

In this equation, $2t_w + D_i$ corresponds to the outer diameter of the pipe (i.e., D_o in Table 7) and K_{sb} represents the hydraulic conductivity of the slotted pipe wall, which has been calculated by Bayer-Raich et al.'s (2022) method, as specified in Table 8. Equation (22) is also applicable to the value of K_{ep} in the *y*-direction. Parameters utilised for calculating K_{ep} and the resulting K_{ep} values are summarised in Table 9.

Table 9. Summary of parameter values for calculating K_{ep} and resulting K_{ep} values used in models.

Parameter	Value		Remark
	150 PN9	**100 PN9**	
Inner diameter of PVC pipe, D_i (mm)	146.85	104.6	Table 7
Wall thickness of PVC pipe, t_w (mm)	6.7	4.85	
Hydraulic conductivity of slotted, PVC pipe, K_{sb} (m/d)	15,060	10,902	Table 8
Integrated hydraulic conductivity of slotted PVC pipe in the *y*- and *z*-directions, K_{ep} (m/d)	141,452	100,895	Equation (22)

5.7 Incorporating the gravel pack and plastic/geofabric layer in models

The gravel pack around the horizontal pipe was represented explicitly in the models. This was achieved using two additional rows (in the *y*-direction): one each on the left-hand and right-hand sides of the slotted pipe cells, and two additional layers (in the *z*-direction): one above the slotted pipe cells and one below. The additional rows and layers representing the gravel pack were set to the gravel pack thickness t_g. A schematic is provided in Figure 19 to show the discretization of the gravel pack.

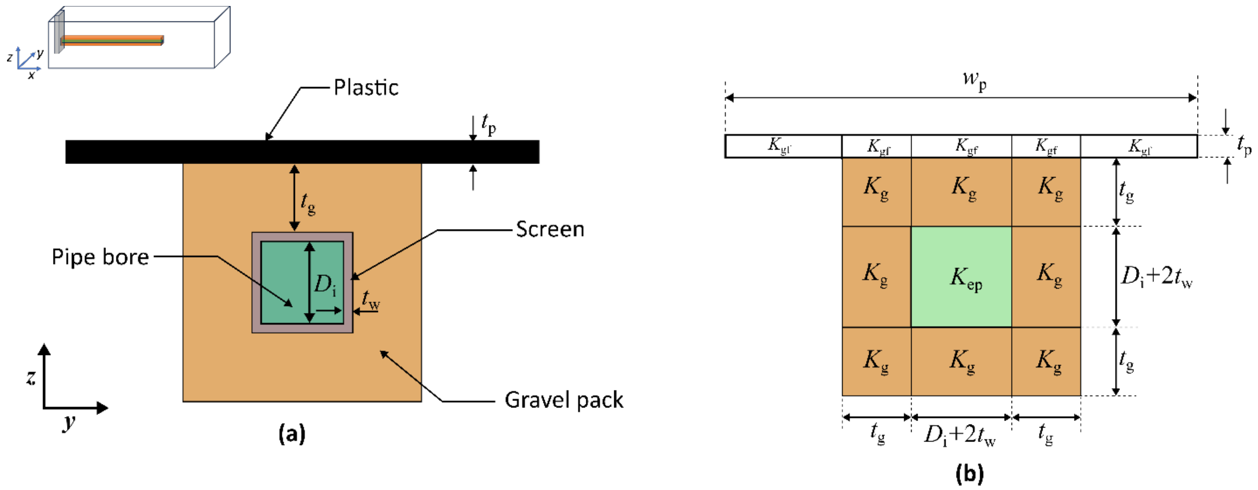

Figure 19. Representation of the gravel pack and overlying plastic sheet in numerical models, showing: (a) conceptual model, and (b) numerical implementation. Cells are labelled with the respective hydraulic conductivity parameters.

In the modelling scenarios incorporating a plastic sheet on top of the gravel pack (as shown in Figure 6b), a single layer with a thickness equal to the plastic sheet thickness (t_p) was added above the gravel pack cells, as shown in Figure 19b. The plastic cells covered a width of w_p (in the y-direction). These plastic cells were defined using an isotropic hydraulic conductivity (K_{pl}) value that was as small as possible (4.9×10^{-8} m/d) without impacting the numerical convergence of MODFLOW.

In the modelling scenarios featuring a gravel pack surrounded by a geofabric layer, as shown in Figure 6c, the conceptual and numerical models were adjusted to incorporate the effect of geofabric on groundwater flow. The thickness of the geofabric layer (t_{gf}) and hydraulic conductivity (K_{gf}) are given in Section 4.3.1. This required representation of the geofabric above, below, and alongside the gravel pack. The geofabric layer was embedded implicitly into the model on the sides of the gravel pack by modifying the gravel pack cells, as shown in Figure 20. This involved widening the cell by t_{gf} and modifying the cell K (K_{eg}) to incorporate flow through the outer layer of geofabric using the following equation for flow through multiple strata placed in series, as (Wiener, 1912):

$$K_{eg} = \frac{t_{gf} + t_g}{\dfrac{t_{gf}}{K_{gf}} + \dfrac{t_g}{K_g}} \tag{23}$$

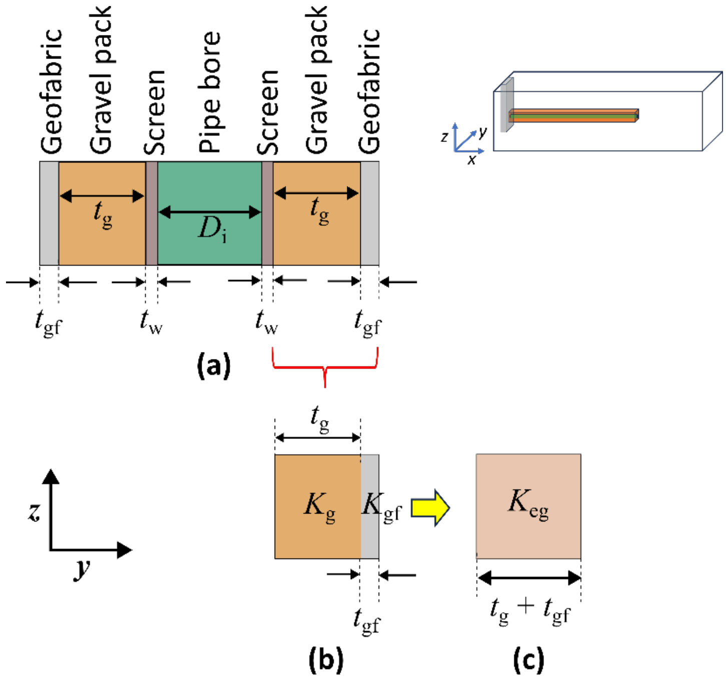

Figure 20. Cross-section of the horizontal pipe of an infiltration gallery, showing the representation of the gravel pack and geofabric layer in a model cell ("Screen" refers to the pipe wall): (a) conceptual model, (b) assignment of parameters to the gravel pack-geofabric conceptual model, and (c) integrated representation of the gravel pack and geofabric layer in the numerical model.

Simple MODFLOW models were built to test that the equivalent hydraulic conductivity approach used to capture multiple gallery components into a single model cell was properly implemented. In one model, five discrete layers with distinct hydraulic conductivity values for each layer were utilised. In another model, three of these five layers were substituted with a single layer having an equivalent hydraulic conductivity that represented several, thinner layers, calculated using Equation (21). The results of the models, including both head and flow data (refer to Appendix A), demonstrate validity in the approach.

Figure 21 summarises the hydraulic conductivities of infiltration gallery components (slotted pipe, gravel pack and geofabric) represented in models.

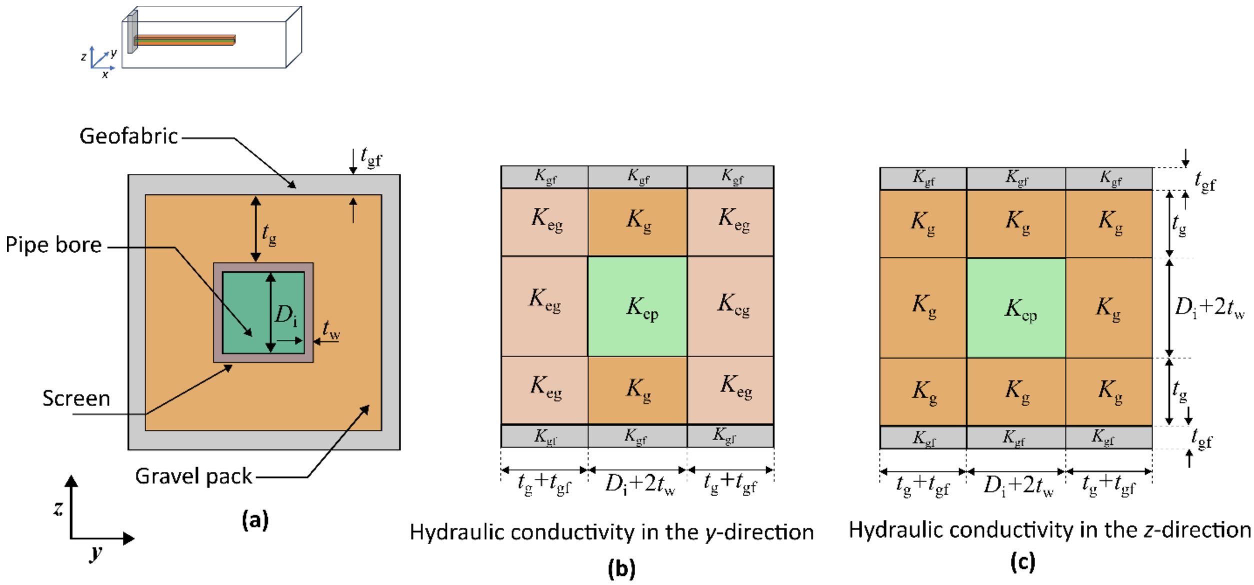

Figure 21. Cross-section of the horizontal pipe of an infiltration gallery, showing the representation of the pipe, gravel pack and geofabric layer in a model cell ("Screen" refers to the pipe wall): (a) conceptual model, (b) assignment of K_y values (hydraulic conductivities in the *y*-direction) of infiltration gallery components: pipe, gravel pack and geofabric), and (c) assignment of K_z values (hydraulic conductivities in the *z*-direction of infiltration gallery components: pipe, gravel pack and geofabric).

The dark-orange cells in Figure 21b are cells representing gravel pack that have gravel pack in the neighbouring cells (on the left and right sides; light-orange cells), and therefore, the hydraulic conductivity in the *y*-direction for those cells simply represents the gravel (K_g). Cells highlighted in light orange in Figure 21b are laterally connected to the geofabric on their left/right side (outer face), and consequently, the hydraulic conductivity for these cells corresponds to the equivalent hydraulic conductivity of the combined gravel pack and geofabric (K_{eg}), as calculated using Equation (23). Since geofabric is explicitly incorporated into the models by adding layers above and below the gravel pack, there is no requirement to combine the hydraulic conductivities of gravel and geofabric in the *z*-direction (as illustrated in Figure 21c). The parameters utilised for calculating K_{ep} and K_{eg}, along with their resultant values are summarised in Table 10.

Table 10. Summary of parameter values for calculating K_{ep} and K_{eg}, and the resulting values used in the base model (Case B).

Parameter	Value
Geofabric thickness, t_{gf} (mm)	3
Gravel pack thickness, t_g (mm)	150
Hydraulic conductivity of gavel pack, K_g (m/d)	2592
Hydraulic conductivity of geofabric, K_{gf} (m/d)	265
Combined hydraulic conductivity of gravel pack and geofabric (Equation 23), K_{eg} (m/d)	2211

5.8 Incorporating horizontal slotted pipe in MODFLOW and SEAWAT models

A high-K approach was applied in the MODFLOW and SEAWAT models to simulate the presence of the slotted pipe. The hydraulic conductivity value along the pipe (in the x-direction) was determined by applying Darcy's law to head losses in the pipe obtaining using pipe-flow equations. Head losses were calculated using Equations (13) to (20) (Section 4.3.3). These adopted a flow rate of Q = 20 m^3/d, a pipe length of L_p = 100 m and a relative roughness for unslotted PVC pipe of $\varepsilon_s = 1.02 \times 10^{-5}$ (see Section 4.3.3). Application of Darcy's Law to the resulting head losses produced K values (in the x-direction) of $K_p = 3.5 \times 10^8$ m/d for 150 PN9 and $K_p = 1.4 \times 10^8$ m/d for 100 PN9 slotted pipes (based on Table 7 and Equations (13) to (20)). These K_p values were used for the high-K implicit representation of pipes in MODFLOW. The ends of the horizontal pipe were closed to flow at one end and connected to the pumping well at the other. The Horizontal Flow Barrier (HFB) Package of MODFLOW was employed to simulate the closed ends of pipes. This HFB package simulates a thin, vertical, low-permeability barrier (Harbaugh, 2005), characterised by K_{br} [LT^{-1}] and L_{br} [L], which are the hydraulic conductivity and thickness of the barrier, respectively (Hsleh and Freckleton, 1993). A very small value of 4.9×10^{-7} d^{-1} was adopted for K_{br}/L_{br} to simulate the closed-end of the horizontal pipe as a trade-off between restricting the flow and producing a numerically stable model.

5.9 Incorporating horizontal slotted pipe in a MODFLOW-CFP model

The slotted pipe was divided into multiple segments in the MODFLOW-CFP model, with each pipe segment connecting two MODFLOW cells at cell centres, as illustrated in Figure 22. The nodes representing pipe segments were assigned unique numbers, while each segment was assigned a pipe-segment number. The location of each pipe node is defined by MODFLOW row, column, and layer numbers. The elevation of each pipe node was aligned with the centroid elevation of the horizontal pipe. Figure 22 illustrates the pipe nodes and segments along with their corresponding identifiers for the base case model (Case B; see Section 6.1).

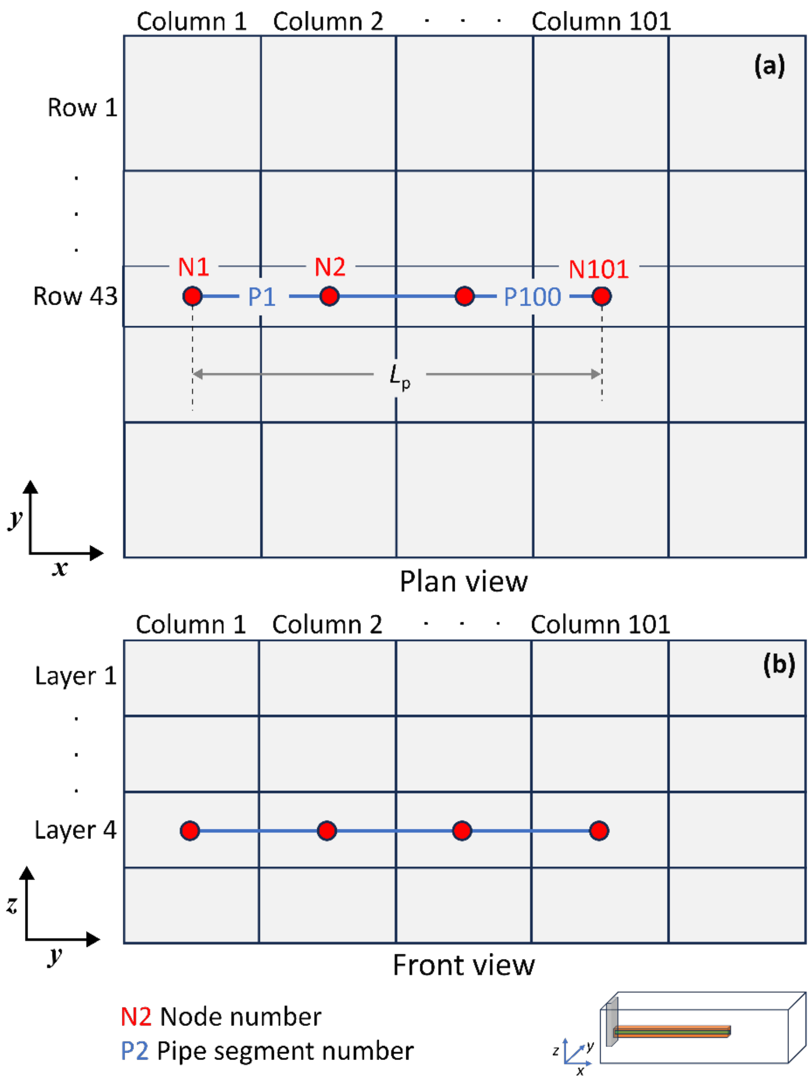

Figure 22. Schematic representation of pipe nodes and segments in MODFLOW-CFP: (a) plan view, and (b) front view, illustrating the configuration for the base case model (Case B; see Section 6.1).

Explicit simulation of the pipe in MODFLOW-CFP model required pipe hydraulic characteristics to be specified. These included constant (in space and time) values for the internal pipe diameter (D_i), internal roughness ($\varepsilon_s \times D_i$; detailed in Section 4.3.3), and tortuosity factor (τ_p [-]) for each individual pipe segment. Flow exchange between the pipe and the aquifer is governed by the pipe wall conductance (C_{sp}), calculated using Equation (12) (Section 4.3.2).

To evaluate the flow regime (laminar, transition, and turbulent) within the pipe, lower and upper limits of the Reynolds number (*Re*; detailed in Section 4.3.3) must be assigned in the MODFLOW-CFP model. Values of 2320 and 4000 (Werner et al., 2020) were adopted as the lower and upper limits (respectively) of *Re*. These were used in MODFLOW-CFP to determine the flow regime by comparing *Re* calculated internally by MODFLOW-CFP to the flow regime limiting values given above. The flow regime determined in this way dictates which equations are adopted by MODFLOW-CFP to determine flow-versus-head loss relationships in the pipe. Outflow from the horizontal pipe was restricted to the end connected to the abstraction well in MODFLOW-CFP.

5.10 Incorporating the abstraction well/sump into models

The abstraction well is isolated from the surrounding aquifer except through its connection to the horizontal well. This was represented in both MODFLOW and MODFLOW-CFP models using explicit layer at the base of the abstraction well with a thickness (t_s = 0.1 m) matching that of the well's base. A very low hydraulic conductivity (K_{sw} [LT^{-1}]) of 4.9 × 10^{-8} m/d (as recommended by Schneider et al. (2012) for concrete) was assigned to cells at the base of the abstraction well to isolate it from the underlying aquifer. To disconnect the side walls of the abstraction well from the aquifer, the HFB Package was adopted using K_{br}/L_{br} equal to 4.9 × 10^{-7} d^{-1}, applied between the abstraction well (high-K) cells and adjacent cells. Although abstraction wells are usually circular in shape, we adopted a rectangular cross section of side dimension set to the typical diameter of abstraction wells (D_s = 1 m). The cells representing the internal space of the abstraction well were simulated in the model using the high-K approach, employing a hydraulic conductivity value of 10^6 m/d in all directions. Again, this represented a trade-off between unrestricted water movements and numerical model stability.

6. Modelling Scenarios

6.1 Base case model for MODFLOW, MODFLOW-CFP, MODPATH and SEAWAT

The initial phase of this study utilised the base case (Case B) in freshwater-only simulations using MODFLOW, MODFLOW-CFP and MODPATH. Seawater was disregarded in the specified-head boundary (i.e., h_b represented the freshwater head) of these models. Subsequently, the SEAWAT variable-density simulations employed the same base case model (i.e., Case B), except the concentration of seawater (C_s = 1) was considered for the specified-head boundary (i.e., h_b represented the saltwater head). This section details Case B and twelve variant models. The parameters utilised in Case B and the sources for parameter values are outlined in Table 11.

Table 11. Summary of parameter values used in the base case model (Case B).

Component		Parameter	Value	Remark
Aquifer	Holocene sediment	Layer thickness (m)	10	Table 6
		Horizontal hydraulic conductivity, K_x (m/d)	10	
		Vertical hydraulic conductivity, K_z (m/d)	1	
		Porosity, n (-)	0.3	
		Specific yield, S_y (-)	0.3	
		Longitudinal dispersivity, α_L (m)	0.1	
		Horizontal transverse dispersivity, α_T (m)	0.005	
		Vertical transverse dispersivity, α_V (m)	0.001	
	Pleistocene limestone	Layer thickness (m)	40	Table 6
		Horizontal hydraulic conductivity, K_x (m/d)	500	
		Vertical hydraulic conductivity, K_z (m/d)	50	
		Porosity, n (-)	0.3	
		Specific yield, S_y (-)	0.3	
		Longitudinal dispersivity, α_L (m)	0.1	
		Horizontal transverse dispersivity, α_T (m)	0.005	
		Vertical transverse dispersivity, α_V (m)	0.001	
	-	Recharge, R (mm/y)	400	§4.1.1
		Mean sea level, MSL (m BGL*)	1.5	§5.5
		Specified-head measured from the base of model domain, h_b (m)	48.5	Fig. 12
		Distance between the pipe and shoreline, W_1 (m)	204.5	Fig. 11
		Half of the landward distance between two adjacent pipes, W_2 (m)	204.5	
		Half of the lateral distance between two adjacent pipes, L_1 (m)	50	
Infiltration gallery	Slotted pipe	Type	150 PN9	Table 7
		Orientation	Parallel to shoreline	Fig. 8a, 11 and 12
		Length, L_p (m)	100	Fig. 6a and 11
		Depth below MSL, D_3 (m)	0.3	Fig. 6a

Component		Parameter	Value	Remark
		Hydraulic conductivity in the *x*-direction, K_p (m/d)	3.5 × 10^8	Eq. (13)-(20)
		Hydraulic conductivity in the *y*- and *z*-directions, K_{sp} (m/d)	15,060	Table 8
		Modified hydraulic conductivity of slotted pipe in the *y*- and *z*-directions, K_{ep} (m/d)	141,452	Table 9
	Geofabric filter and plastic exclusion layer	Type	Plastic	Fig. 6b
		Width, w_p (m)	1	
		Thickness, t_p (m)	0.003	
		Hydraulic conductivity in all directions, K_{pl} (m/d)	4.9 × 10^{-8}	§4.3.1
	Gravel pack	Thickness, t_g (m)	0.15	Fig. 6b
		Hydraulic conductivity, K_g (m)	2592	§4.3.1
	Sump	Diameter, D_s (m)	1	Fig. 6a
		Depth of sump base below pipe base, D_4 (m)	1	
		Wall thickness, t_s (m)	0.1	§5.10
		Wall/base hydraulic conductivity, K_{sw} (m/d)	4.9 × 10^{-8}	
		Pump rate, Q (m^3/d)**	20	§5.8

*m BGL = metres below ground level.

**Pump rate is half the field value because of the symmetry axis placed centrally through the abstraction well.

As shown in Table 11, Case B consists of a transient simulation of an atoll aquifer containing an infiltration gallery comprising a single, horizontal, slotted pipe aligned parallel to the shoreline, with an abstraction well at one end of the pipe. The slotted pipe is surrounded by a gravel pack, and there is a plastic exclusion layer placed above the gravel pack. The model domain is delineated by the red-dashed line in Figure 11.

6.2 Overview of modelling scenarios in variable-density SEAWAT simulations

Twelve variants models were created as SEAWAT variable-density simulations to assess the influence of various design parameters on the performance of infiltration galleries and their impact on freshwater lenses. The simulations investigated a spectrum of scenarios associated with infiltration gallery design, as described below.

Case 1: The same as Case B (see Table 11), except the pumping rate was 50% of the Case B value.

Case 2: The same as Case B, except the pumping rate was 150% of the Case B value.

Case 3: The same as Case B, except the Holocene sediments had a hydraulic conductivity that was 50% of the value adopted in Case B.

Case 4: The same as Case B, except the Holocene sediments were 50% thicker than that adopted in Case B.

Case 5: The same as Case B, except the hydraulic conductivity of the pipe slots was 50% of the Case B value.

Case 6. The same as Case B, except rather than employing a layer of plastic on top of the gravel pack, a geofabric layer surrounded the gravel pack.

Case 7. The same as Case B, except the horizontal pipe was twice as long as the Case B value.

Case 8. The same as Case B, except the horizontal pipe diameter was 2/3 of the Case B value.

Case 9. The same as Case B, except the horizontal pipe was connected to two abstraction wells, one at each end of the pipe, instead of the central well used in Case B. The model domain for Case 9, including axes of symmetry (no-flow boundaries in the model), is shown by the red-dashed lines in Figure 23.

Case 10. The same as Case B, except the horizontal pipe was aligned perpendicular to the shoreline. The distance between the end of the pipe and the shoreline was ~24% of the Case B value. The model domain in Case 10 is shown by the red-dashed lines in Figure 24, again demonstrating axes of symmetry.

Case 11. The same as Case B, except the horizontal pipe was aligned perpendicular to the shoreline, and the distance between the end of the pipe and the shoreline was ~98% of the Case B value.

Case 12. The same as Case B, except with the addition of two small, branched pipes (each 24 m in length either side of the main horizontal pipe) aligned perpendicular to the shoreline at the midpoint of the main pipe. The model domain for Case 12 is shown by the red-dashed lines in Figure 25.

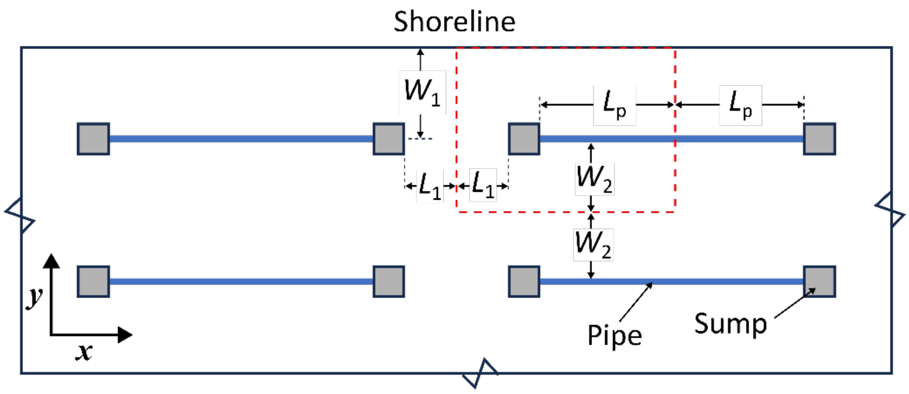

Figure 23. Plan view of a series of infiltration galleries aligned parallel to the shoreline with abstraction wells at either end of each gallery. The red-dashed line delineates the region utilised in simulating Case 9.

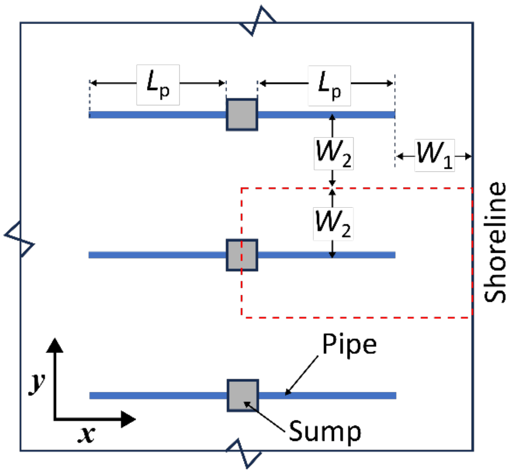

Figure 24. Plan view of a series of infiltration galleries aligned perpendicular to the shoreline. The red-dashed line delineates the region utilised in simulating Case 10.

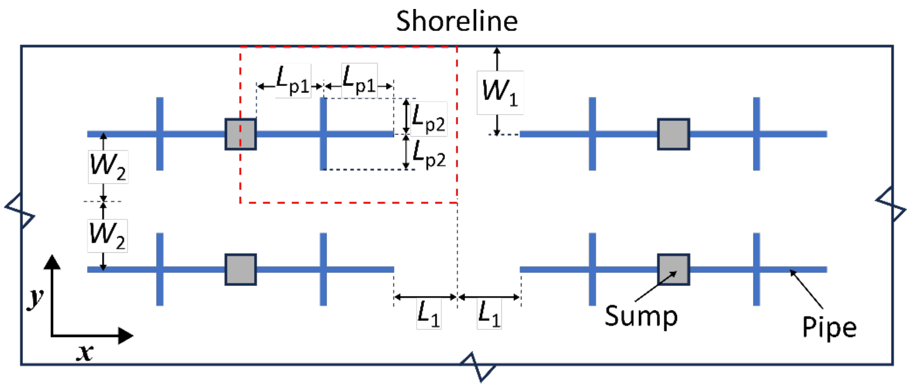

Figure 25. Plan view of a series of branched infiltration galleries, comprising pipes that are both parallel and perpendicular to the shoreline. The red-dashed line delineates the region utilised in simulating Case 12.

Table B1 (Appendix B) presents a summary of all model scenarios utilised in SEAWAT variable-density simulations. The details of the model discretisation for each model scenario are presented in Table B2 (Appendix B).

7. Results

7.1 Freshwater-only simulations

7.1.1 MODFLOW

The steady-state head results produced by MODFLOW (freshwater-only, neglecting density effects) for Case B are provided in Figure 26. The flow vectors are also shown as faint white arrows.

Figure 26a depicts the head distribution within a horizontal plane (*x*-*y*) that is midway through the vertical extent of the horizontal pipe, at an elevation of 0.22 m below MSL. Head variations are subtle, except around the horizontal pipe, where head contours reflect the drawdown caused by groundwater flow towards the slotted pipe. Near the shoreline, the head slopes towards the sea due to fresh groundwater discharge to the sea. A groundwater high (peak of a small groundwater mound) occurs at around y = 281 m, representing a transition from flow towards the pipe to flow towards the sea. The water table elevation of the groundwater high is 48.509 m above the model base, which is a mere 9 mm above MSL. There needs to be a groundwater elevation that exceeds mean sea level between the gallery and the sea to avoid significant amounts of seawater entering the infiltration gallery, because without fresh groundwater flow to the sea, seawater will flow actively towards the well (Werner, 2017). The fact that this is only 9 mm above sea level highlights the fragility of the system, in which a small drop in head could lead to the situation where the zone of groundwater flow towards the gallery captures the ocean boundary (and therefore seawater must eventually reach the gallery).

The groundwater high identifies the capture zone of the well, which is approximately 76.5 m seaward of the horizontal pipe. This is a zone where any surface contaminants would eventually reach the well. A groundwater high is not apparent on the other side of the well (0 m < y < 204 m) because the inland boundary is a no-flow condition. Thus, freshwater within the model domain immediately inland of the pipe flows towards it, defining this region as part of the gallery's capture zone. Arrows showing the flow pattern in Figure 26 reflect these interpretations of flow from the head contours.

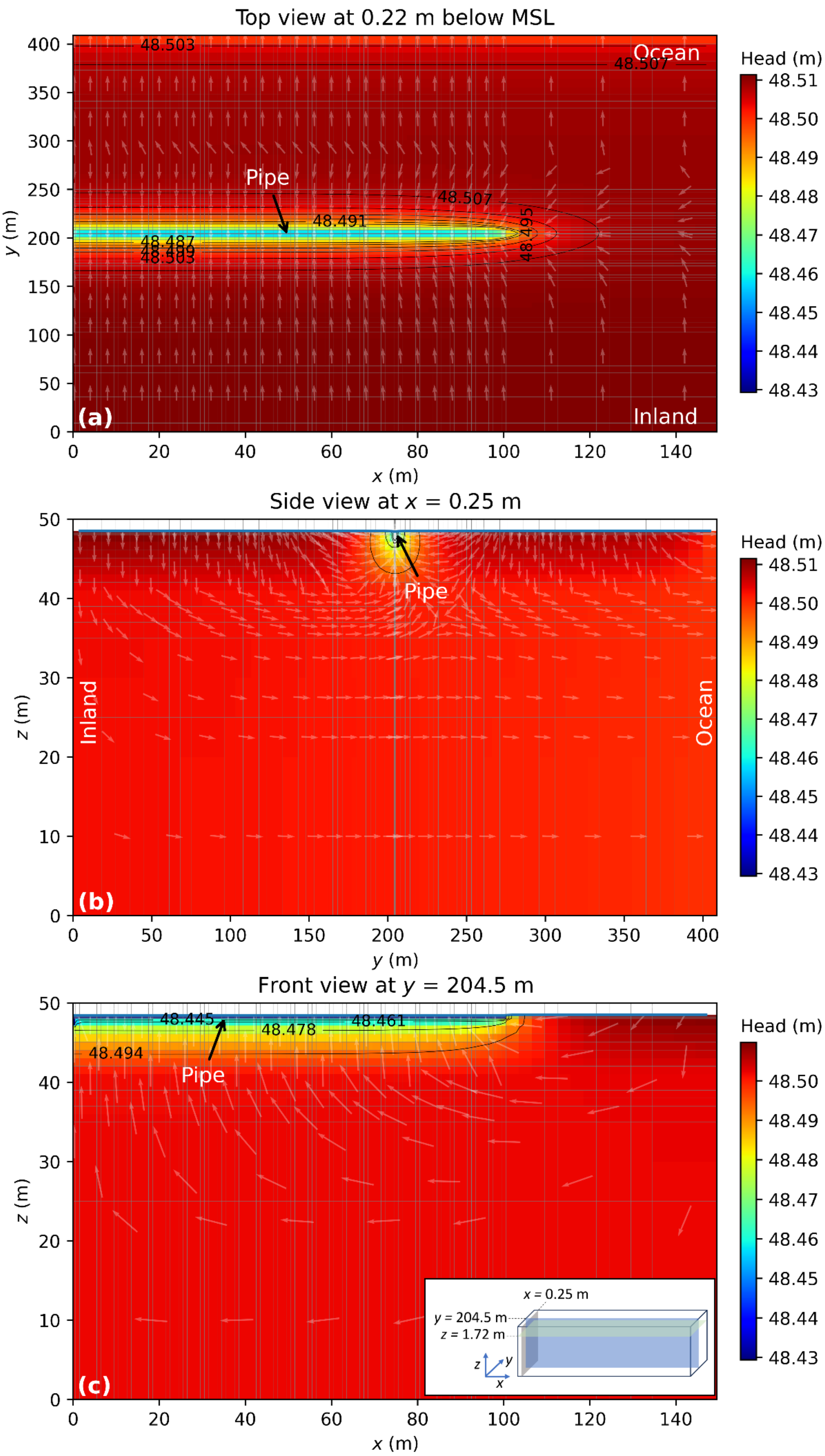

Figure 26. Head distribution for Case B obtained from the MODFLOW (freshwater-only) model. Black lines show the head contours, while the blue line indicates the water table. White arrows depict flow directions (arrows are shown for only a portion of the model cells).

At the end of the pipe furthest from the abstraction well (x = 100.5 m), the head inside the pipe was 48.4309 m. Here, we report heads that are unrealistically precise relative to modern water level instruments because an assessment of very small head gradients requires it. For example, at the end of the pipe connected to the abstraction well (x = 0.5 m), the head inside the pipe is 48.4308 m. This indicates a miniscule head drop of 1×10^{-4} m causing flow within the pipe. The head within the abstraction well was 48.4306 m, revealing also a very small head loss (2×10^{-4} m) between the pipe and the abstraction well. This is higher than the head drop due to flow along the horizontal pipe because the abstraction well adopts a higher K (10^6 m/d) than the horizontal pipe (3.5×10^8 m/d). Water entering the abstraction well from the horizontal pipe will experience an "entrance loss" of ~$v_p^2/2g$, which is roughly 9×10^{-6} m. These values are all well within measurement error and are therefore largely academic in terms of the hydraulics of the system. The head in the abstraction well was 0.03 m lower than the head in the aquifer surrounding it. The maximum drawdown observed in Case B, as a head drop compared to Case 0 (where Case 0 represents conditions before installation of the pipe) was recorded in the abstraction well, totalling 0.0810 m (results of the freshwater-only simulation for Case 0 are not presented here for brevity). Here, we use "drawdown" for the difference between the water level of open water (i.e. water in the abstraction well in Case B) and the water table in the aquifer (at the same location in Case 0) before the pipe was installed – even though "drawdown" is usually reserved for head drops in aquifers rather than open water head drops in pipes. The drawdown in the pipe at the beginning (x = 0.5 m) and end (x = 100.5 m) points were 0.0808 m and 0.0807 m, respectively.

7.1.2 MODFLOW-CFP

The steady-state head results produced by the MODFLOW-CFP model (freshwater-only; density effects were not considered) for Case B, featuring an infiltration gallery parallel to the shoreline as detailed in Section 6.1, are shown in Figure 27. The MODFLOW-CFP model explicitly simulates the slotted pipe, as outlined in Section 5.9.

The head results obtained from the MODFLOW-CFP model are very similar to those produced by the implicit pipe model developed in MODFLOW (see Figure 26), indicating that the explicit and high-K representations of the horizontal pipe in the two codes are largely consistent.

Table 12 summarises the key observations from the MODFLOW-CFP model and compares them with results from the MODFLOW model. These include the head at the beginning and end points of the pipe, the head in the abstraction well, the total head loss within the horizontal pipe, the head loss incurred from water entering the abstraction well from the pipe, and the drawdown at the beginning and end points of the pipe and within the abstraction well (recalling that drawdown here is the difference between the head in the pipe and the head in the aquifer before the pipe was installed).

Table 12. Key observation from the MODFLOW-CFP and MODFLOW models.

Parameters		MODFLOW	MODFLOW-CFP
Head (m)	**Pipe beginning***	48.4308	48.4300
	Pipe end**	48.4309	48.4300
	Abstraction well	48.4306	48.4294
Head loss (m)	**Along the pipe†**	1×10^{-4}	$<10^{-5}$#
	Entrance of abstraction well††	3×10^{-4}	2×10^{-4}
Drawdown (m)	**Pipe beginning**	0.0808	0.0816
	Pipe end	0.0807	0.0816
	Abstraction well	0.0810	0.0822

*Immediately adjacent to the abstraction well

**The end of the pipe that is closed off

†Calculated as the difference in the heads in the pipe at the pipe end and the pipe beginning.

††Calculated as the difference between the head in the pipe at the pipe beginning and the head in the abstraction well.

#Head loss less than the precision of reported values from MODFLOW-CFP

Table 12 reveals only small differences between the implicit (high-*K*) and explicit representations of the horizontal pipe. This is partly attributable to the very small head gradients that occur within (and between) the pipe and abstraction well, whereby even an order-of-magnitude difference in the head losses would be an error smaller than 0.01 m. Manual calculations of head losses in the pipe also showed exceedingly small values (see Section 4.3.3). This indicates that the high-*K* approach reasonably reproduces the pipe hydraulics (at least for the pumping rates that were considered in the comparison) and is suitable for application in SEAWAT to assess interactions between the infiltration gallery and the buoyant freshwater lens.

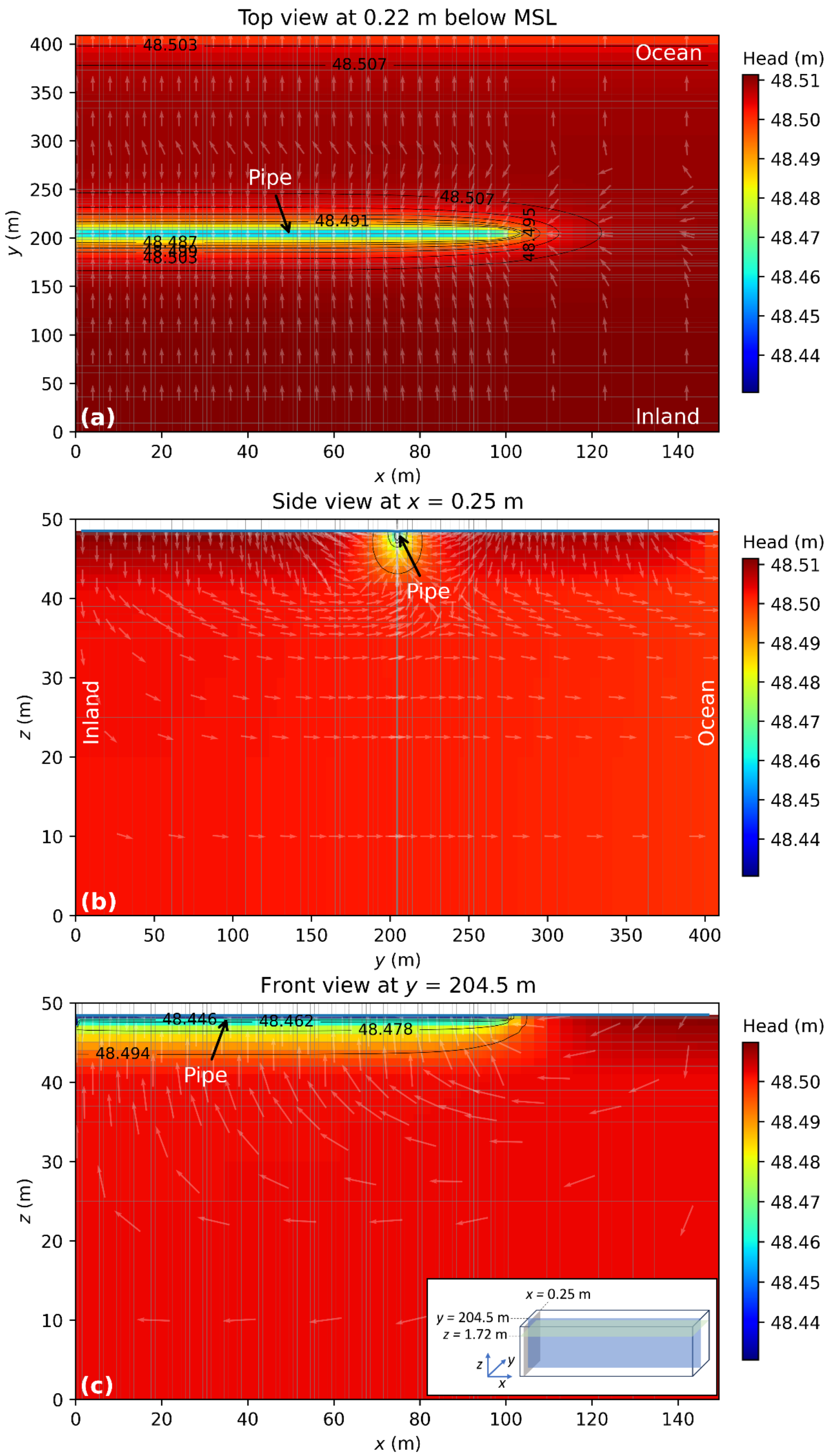

Figure 27. Head distribution for Case B derived from the MODFLOW-CFP (freshwater-only) model. Black lines show the head contours, while the blue line indicates the water table. White arrows depict flow directions (arrows are shown for only a portion of the model cells).

7.1.3 MODPATH

The results of the backward-tracking simulation of particle paths for Case B, obtained using MODPATH for freshwater-only conditions, are presented in Figure 28 in 2D planes. Figure 29 provides a 3D depiction of flow paths. As the main goal of freshwater-only simulations was to check the hydraulic calculations for the flow into and within the horizontal pipe, and considering that buoyancy forces are neglected, only a brief analysis of the well capture zone is offered here.

The flow paths are those taken by particles that have reached the edge of the horizontal pipe. Each particle trace represents its movement over a period of ~15 years. The paths of 80 particles are presented in Figures 28 and 29, with particles spaced at 5 m intervals along the pipe (in the *x*-direction) and four particles placed around the circumference of the pipe. In Figure 28, the particle traces are shown in three different 2D planes: *x*-*y*, *x*-*z* and *y*-*z*, with each passing through the middle of the pipe and/or the middle of the abstraction well.

Figures 28b and 28c show that particles flowing into the pipe tend to have an upward component of flow, after travelling downwards in recharge areas to deeper parts of the aquifer. Particles move perpendicular to the head contours, as expected. The arc followed by many particles causes them to flow well below the bottom of the pipe. Particle paths reach as deep as 16.1 m below MSL. This is deeper than the base of the Holocene, which occurs at 8.5 m below MSL in Case B (Table 11). The Holocene-Pleistocene unconformity in the model is apparent as inflexions in the particle paths at that depth (i.e., 40 m above the model base; Figure 28c). Pathways that move into the Pleistocene layer are more likely to entrain saltwater in the flow towards the well. These results do not consider buoyancy effects, which likely influence vertical flow given the higher density of saltwater, and therefore, the maximum depth reached by the flow paths was probably over-estimated (perhaps only to a small degree as seawater is only 2.5% denser than freshwater) in freshwater-only models.

Several particles in Figure 28 reach the water table, thereby showing the point of recharge for those particles. The starting point of particles that don’t reach the water table are predictable by considering their trajectories (e.g., Figure 28c). As some particles did not reach the water table within the ~15 years of the simulation, the maximum age of groundwater entering the well exceeds 15 years. Figure 28c shows that groundwater flowing into the gallery from the sea is substantially older because all of the particles on the landward side of the gallery reached the water table within the ~15-year timeframe of the model.

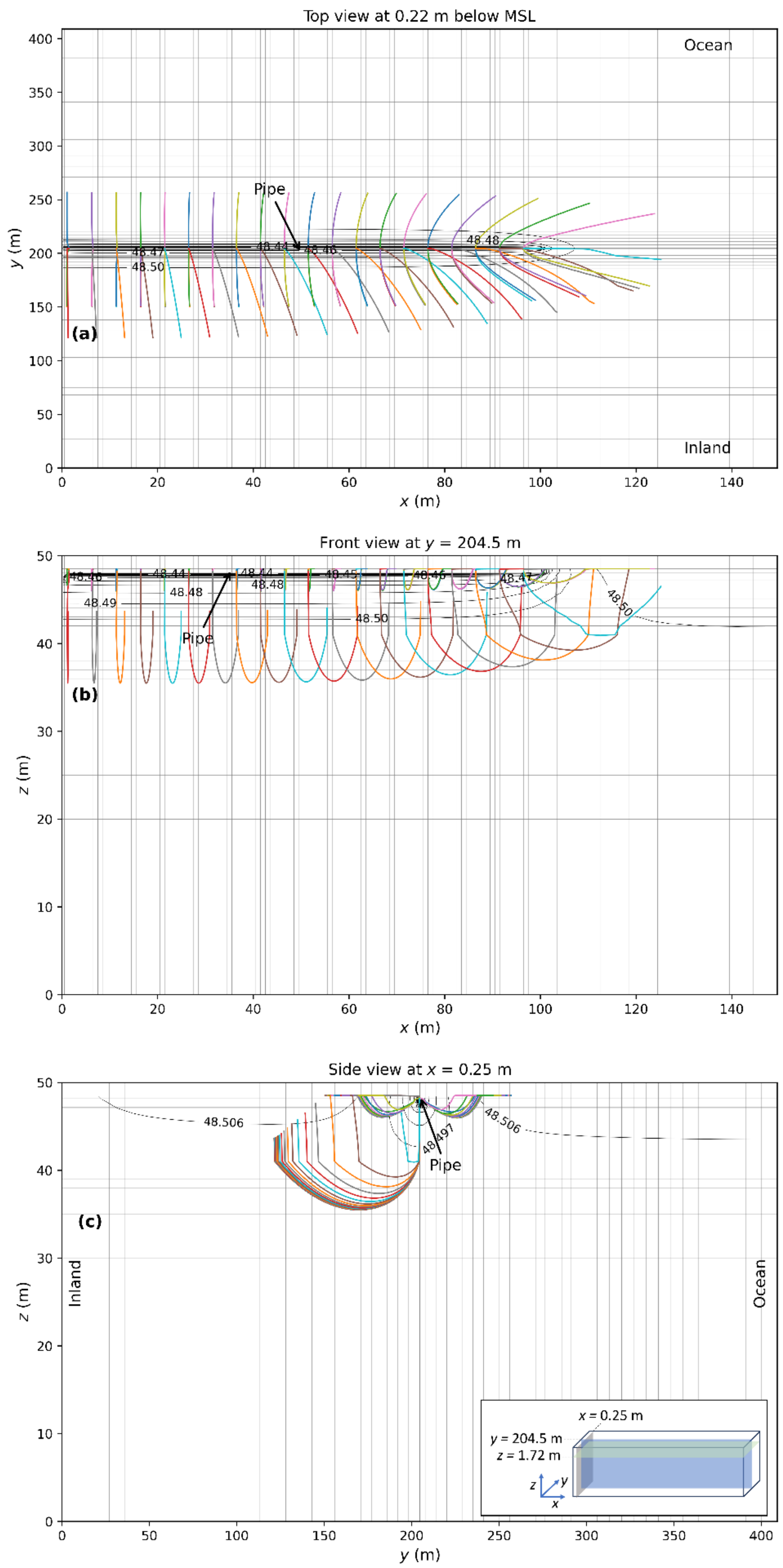

Figure 28. The capture zone of an infiltration gallery after ~15 years, obtained through backward-tracking of 80 particles in Case B. Particle paths are represented in 2D planes, as: (a) horizontal plane passing through the middle of the pipe (0.22 m below MSL), (b) cross-section passing through the middle of the pipe (*y* = 204.5 m), and (c) cross-section passing through the middle of the abstraction well (*x* = 0.25 m).

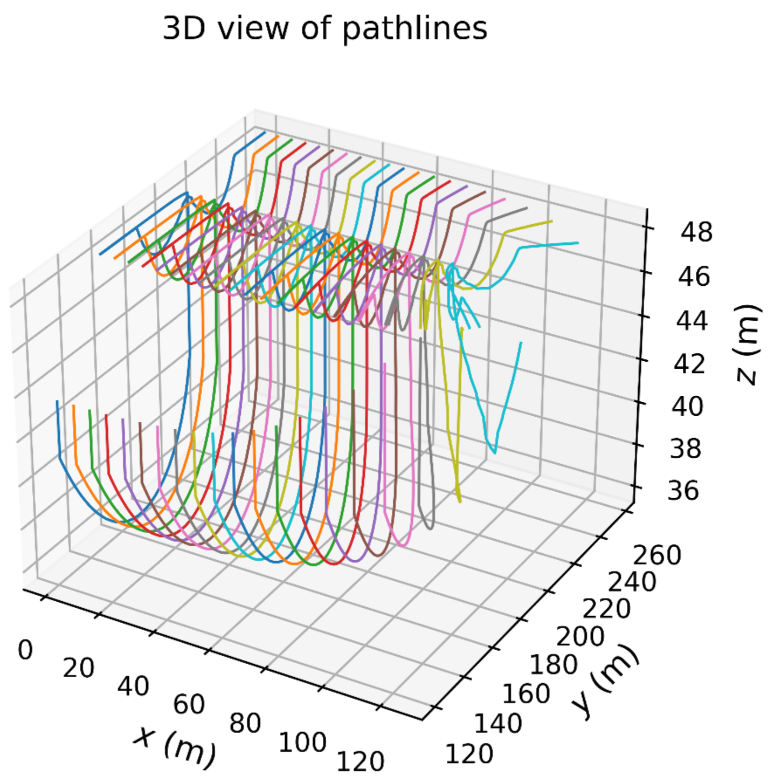

Figure 29. 3D representation of particle paths showing the capture zone (after ~15 years) for the infiltration gallery of Case B. Water density effects are neglected.

Figures 28a and 28c show that the capture zone of the well, identified by particle traces, was further afield on the landward side compared to the seaward side of the pipe (i.e., in the *y*-direction). Specifically, the capture zone (i.e., determined by the starting point of particles) was up to 83.3 m from the pipe centroid on the landward side and up to 51.5 m on the seaward side. The capture zone also extended up to 25 m beyond the end of the pipe. In fact, the capture zone on the seaward side of the pipe was 76.5 m from the pipe (the distance to the groundwater mound; Section 7.1.1), which is larger than the extent of particles due to the finite number of particles used to assess flow paths. Much of the recharge occurring on the landward side of the gallery flowed beneath the gallery, reaching the shoreline. This likely included recharge occurring over approximately 0 m < y < 121.2 m (i.e., beyond the landward extent of particle paths; Figure 28c) that bypassed the infiltration gallery. This is also apparent in the flow directions shown in Figure 27b.

7.2 SEAWAT variable-density simulations

7.2.1 Steady-state simulations prior to installation of the infiltration gallery (Case 0)

Simulations of the effects of infiltration galleries on the freshwater lens required a pre-development simulation to establish the conditions absent the gallery. This involved application of a transient model to capture the pre-development characteristics of the freshwater lens. The model utilised an identical set of aquifer parameters (refer to the “Aquifer” component of Table 11) and grid discretisation (refer to Section 5.3) as adopted in Case B but excluded pumping and hydraulic properties associated with infiltration galleries. Specifically, for corresponding cells that contained infiltration gallery components in Case B (i.e., abstraction well/sump, horizontal slotted pipe, and plastic/geofabric layer), the hydraulic properties of the Holocene sediments, including horizontal and vertical hydraulic conductivities (i.e., K_x and K_z, respectively), and porosity (refer to Table 11), were employed. The model ran for ~27 years until a steady-state condition was achieved in both head and salt concentration, determined by time-invariant total salt mass within the model domain. The steady-state results from this transient model were adopted as initial conditions for Cases B, 1, 2, 5 and 6 (see Table B1 in Appendix B), in which the hydraulic properties of the aquifer and the model size and discretisation were similar. The same approach was employed to build pre-development models for obtaining the initial conditions of all other cases, considering their respective aquifer hydraulic properties and model scale/discretisation.

The steady-state results of relative salinity and heads before the installation of the infiltration gallery are presented in Figures 30 and 31, respectively. Table 13 presents the freshwater thickness and water table elevation at the furthest landward boundary (i.e., y = 0 m) and the middle of the aquifer (i.e., y = 204.5 m).

Figure 30a depicts a freshwater lens with largest thickness (9.67 m) at the landward edge of the model (y = 0 m), as expected. Here, the freshwater lens thickness is the depth between the water table and a relative salinity of 0.01. This is larger than the depth of water above the Holocene-Pleistocene discontinuity of ~8.79 m (water table elevation of ~0.29 m MSL minus the discontinuity elevation of -8.5 m MSL). The effect of the Holocene-Pleistocene discontinuity on the lens creates a similar thickness of freshwater over most of its extent, with depths varying from 9.30 m to 9.67 m over the distance 0 m < y < 204.5 m (see Table 13). A classical saltwater wedge, with a sloping freshwater-saltwater mixing zone, occurs over a distance of roughly 60 m from the shoreline, beyond which the base of the freshwater lens is mildly sloping (Figure 30a).

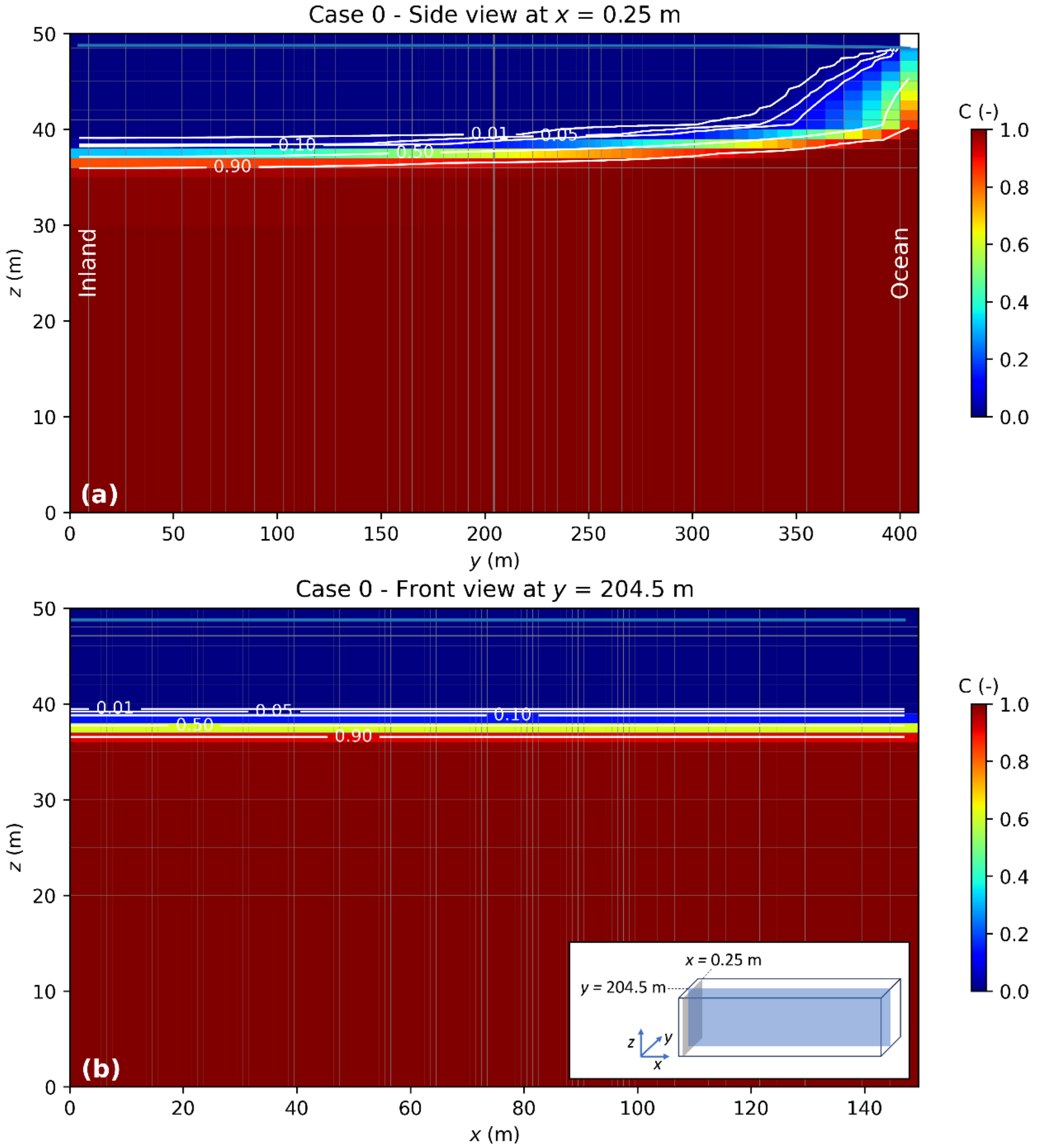

Figure 30. Salinity distribution under pre-development, steady-state conditions (prior to the installation of an infiltration gallery; Case 0): (a) Side view displaying the concentrations at *x* = 0.25 m, representing a cross-section passing through the location where the abstraction well occurs in Case B, (b) Front view of the concentration distribution at *y* = 204.5 m, corresponding to a cross-section passing through the centreline of the horizontal pipe that is simulated in Case B. A relative salinity scale is adopted, where *C* = 0 represents freshwater and *C* = 1 represents seawater. White lines show relative salinity contours, while the light-blue line indicates the water table.

Table 13. Freshwater lens thickness and water table elevation at the landward boundary (i.e., *y* = 0 m) and halfway between the shoreline and the landward boundary (i.e., *y* = 204.5 m, corresponding to the location of the horizontal pipe in Case B).

		at *y* = 0 m	at *y* = 204.5 m
Freshwater lens thickness (m)*	0.01 isochlor contour	9.67	9.30
	0.05 isochlor contour	10.38	9.60
	0.1 isochlor contour	10.55	9.97
	0.5 isochlor contour	11.65	11.04
	0.9 isochlor contour	12.84	12.22
Water table (m MSL)		0.29	0.28

*Calculated as the difference between the water table elevation and the elevation of the given relative salinity contours.

Table 13 shows that the water table elevation clearly exceeds the equivalent freshwater head at the Holocene-Pleistocene unconformity of 0.2125 m MSL. The head at *y* = 204.5 m exceeds this value by some 0.068 m. This gives a rough approximation of the allowable drawdown caused by the infiltration gallery, because if the water table falls below this value, seawater can be expected to reach the well (taking the conservation approach of the Ghyben-Herzberg relation).

Figure 31 provides 2D depictions of the groundwater heads in Case 0, using three different planes (*x*-*y*, *y*-*z* and *x*-*z*). Figure 31a shows the heads in a horizontal plane (*x*-*y*) that slices the model at an elevation of 0.22 m below MSL, thereby effectively showing the water table distribution throughout the model domain for Case 0. The elevation of the *x*-*y* plane in Figure 31a represents the middle elevation of the horizontal pipe that is included in Case B (but is omitted in this pre-development case). Figure 31 also displays the flow directions. The flow directions are not perpendicular to the head contours (see Figures 31b and 31c), as occurs in freshwater-only model results, due to the effects of density.

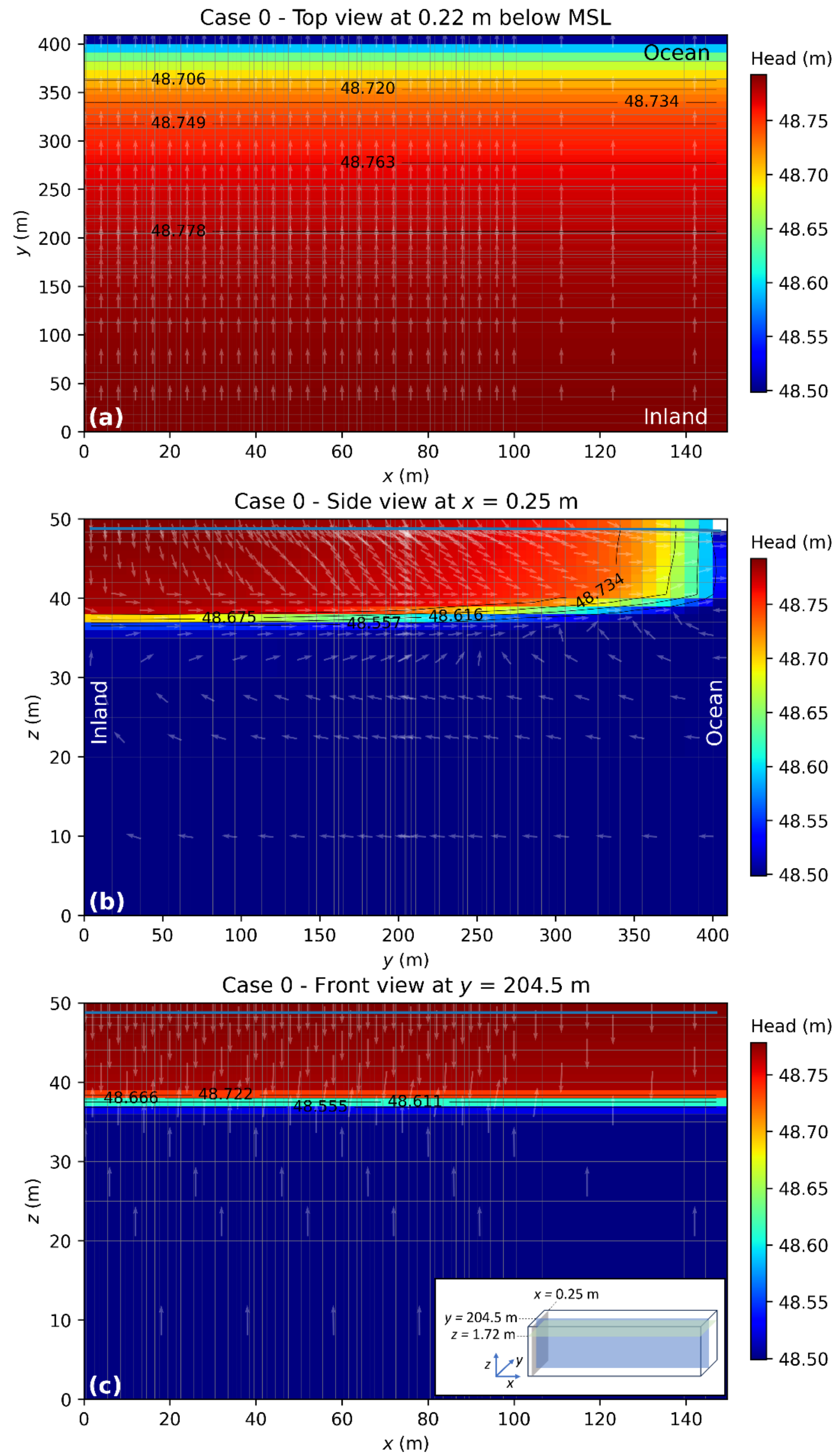

Figure 31. Head distributions from Case 0, representing steady-state, pre-development conditions. Black lines show the head contours, while the light-blue line indicates the water table. White arrows depict flow directions (arrows are shown for only a portion of the model cells). Heads are shown in 2D planes that pass through the centre line of the horizontal well and/or the infiltration gallery.

Figure 31 shows that the model produced head contours that are parallel to the shoreline, consistent with the expectation that all (net) recharge flows towards the sea in the absence of pumping from the lens. The flow field in Figures 31a and 31b (white arrows) shows freshwater flow toward the sea (consistent with the head contours) within the Holocene layer (the base of this layer is -8.5 m MSL). In the Pleistocene layer, seawater circulation is apparent as both inflow and outflow of seawater from/to the ocean (Figure 31b). This circulation is observable across the whole island, with seawater moving landward in the lower part of the model until it reaches the inland boundary, before returning to the ocean (y = 409 m) as seawater entrained in the freshwater-seawater mixing zone. Seawater circulation produces an upward component of groundwater flow in the deeper aquifer in Figure 31c, which also shows downward flow of fresh groundwater in the upper aquifer due to recharge.

The total volume of freshwater (V_f [L^3]) in the Case 0 lens, depicted in Figures 30 and 31, was 147,948 m^3. This equates to a depth of freshwater (open water) equal to 2.42 m (obtained by dividing the freshwater volume by the model surface area of 61,145.5 m^2), or an average freshwater lens thickness of 8.07 m (equal to the depth of freshwater divided by the porosity, n = 0.3). The calculation of V_f involved summing the volumes of freshwater in each cell, computed using the formula $(1-C) \times \Delta x \times \Delta y \times \Delta z \times n$, where C is the relative salinity (C = 0 for freshwater and C = 1 for seawater), Δx, Δy, and Δz denote the dimensions of the cell in the x-, y-, and z-directions, respectively, and n is the porosity of each cell. Only cells where $C \leq 0.01$ were considered in determining the freshwater volume, presuming that water exceeding this concentration is unsuitable for human use. For cells containing the water table (i.e., that are unconfined), the value of Δz was taken as the saturated thickness (the depth of water in the cell, calculated as the head minus the cell base).

The average lens thickness of 9.24 m is close to the freshwater lens thickness of 9.30 m at y = 204.5 m (Table 13), which is halfway between the shoreline (where the lens is thinnest) and the inland boundary (where the lens is thickest).

7.2.2 Case B

Case B includes an infiltration gallery parallel to the shoreline (see Section 6.1), but otherwise the same hydrogeological parameters as Case 0 were adopted. The steady-state results in terms of heads and relative salinities are presented in Figures 32 and 33, respectively.

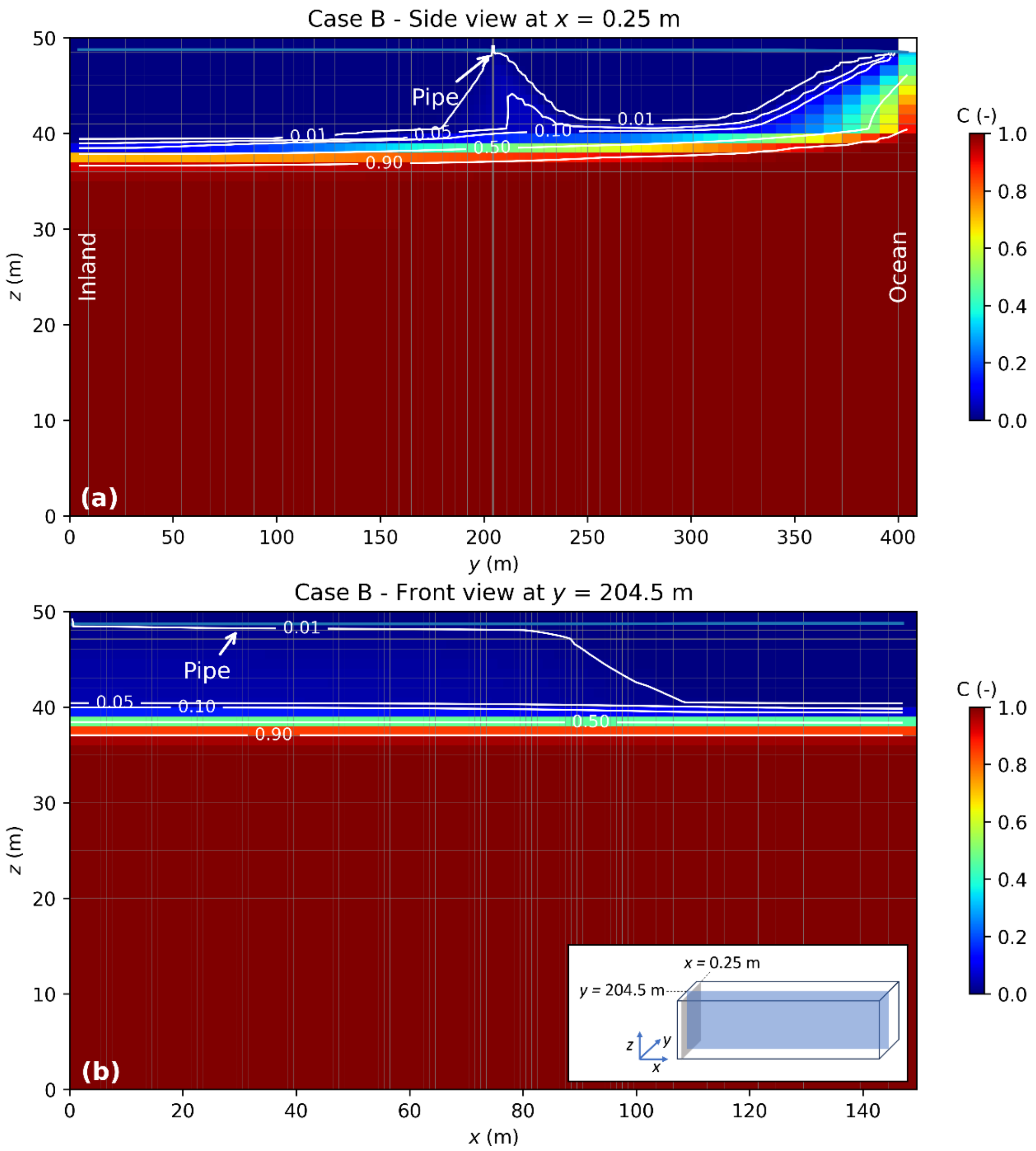

Figure 32. Relative solute concentration (C = 0 for freshwater and C = 1 for seawater) for Case B. White lines show the isochlor contours, while the blue line indicates the water table.

Figure 32a shows the salinity distribution at x = 0.25 m, a cross-section passing through the middle of the abstraction well. Up-coning is observed at the location of abstraction well, causing the 0.01 isochlor contour to reach the water level in the abstraction well (48.68 m measured from the base of the model or 0.18 m above MSL), indicating a salinity that exceeds this in the abstraction well. Figure 32b shows the concentration at y = 204.5 m, a cross-section passing through the pipe centreline. This shows the elevation of the 0.01 isochlor contour remaining at a similar elevation (approximately within the horizontal pipe; 48.205 m < z < 48.355 m) between about x = 80 m until the beginning of the pipe (at x = 0.5 m). The 0.01-isochlor rises from about z = 40 m (at x = 108.7 m) to approximately the base of the pipe at x = 80 m. Thus, the pipe influences the saltwater distribution over a distance of some 8.2 m beyond the end of the pipe (at x = 100.5 m). Other isochlor contours remain beneath the horizontal pipe, showing gentle increases in their elevations. For instance, the 0.05 isochlor contour elevation increases from 39.85 m (i.e., 8.65 m below MSL) at *x* = 147 m to 40.42 m (i.e., 8.08 m below MSL) at *x* = 0.25 m, while the 0.1 isochlor contour elevation increases from 39.43 m (i.e., 9.07 m below MSL) at *x* = 147 m to 39.97 m (i.e., 8.53 m below MSL) at *x* = 0.25 m. The 0.5 isochlor contour elevation increases from 38.37 m (i.e., 10.13 m below MSL) at *x* =147 m to 38.44 m (i.e., 10.06 m below MSL) at *x* = 0.25 m, while 0.9 isochlor contour in Figure 32b remains approximately at the same elevation of 37.06 m (i.e., 11.44 m below MSL).

Table 14 summarises the depths to various salinity contours at the location of the abstraction well and compares them to values for Case 0 (before the installation of the infiltration gallery; refer to Table 13). The results show larger changes for contours of lower salinity, which is expected given that these are more likely to rise due to up-coning compared to the higher-salinity contours.

Table 14. Depths to different salinity contours at the position of the abstraction well and the water level in the abstraction well (i.e., *x* = 0.25 m and *y* = 204.5 m). Percentage changes (i.e., for Case B) are relative to values for the aquifer before installation of the gallery (Case 0).

		Value (m)	Percentage change (%)**
Depth to difference salinity contours*	**0.05 isochlor contour**	8.26	-14.0
	0.1 isochlor contour	8.72	-12.5
	0.5 isochlor contour	10.2	-7.25
	0.9 isochlor contour	11.6	-4.91
Water table		0.18***	-3.44

*Calculated as the difference between the water table elevation and salinity contours.

**(Case B value – Case 0 value)/Case 0 value ×100%.

***Above MSL.

At the end of the pipe (i.e., *x* = 100.5 m), the concentration inside the pipe was 0.00014. This increased towards the abstraction well, reaching a maximum value of 0.0109 at the beginning of the pipe (i.e., *x* = 0.5 m; where it connects to the abstraction well). This is consistent with observations of the 0.01 relative salinity contour occurring within the well, as described above. Meanwhile, the concentration in the gravel pack layer just beneath the pipe at the end and beginning of the pipe reached 0.00022 and 0.0121, respectively. The lower concentration in the pipe indicates dilution due to freshwater entering along the slotted pipe, particularly from the sides and from above, where the groundwater is fresher than below the pipe. The relative salinity in the abstraction well was 0.0109 (the same as the value at the beginning of the pipe, as expected). This value is equivalent to ~1094 µS/cm, assuming a recharge water salinity of 500 µS/cm and taking seawater salinity to be 55,000 µS/cm. Notably, measurements of produced-water salinity on Kiritimati Atoll typically range from 1200 to 1400 µS/cm, providing compelling evidence that the model reasonably reflects atoll island conditions.

Figure 33 illustrates head distributions within three planes passing through the middle of the pipe and/or the abstraction well, similar to the *x-y*, *x-z* and *y-z* planes presented in Figures 27 and 31. Figure 33a shows that head contours in some places are no longer parallel to the shoreline, as was observed in Case 0 (before the installation of the gallery; Figure 31). Drawdown is evident around the pipe, as is flow towards the pipe, due to extraction. A water table mound formed at approximately y = 253 m (Figures 33b and 33c), with a maximum water table elevation of 48.75 m (measured from the model base). This indicates that the pipe captured water from a region that extends approximately 48.5 m seaward of the pipe. This is less than seaward capture zone in the freshwater-only simulations of 76.5 m (see Section 7.1.3). This arose because a greater proportion of freshwater entered the well from the landward side because the freshwater-saltwater interface limited the depth of freshwater flow. The interface caused a smaller region beneath the well where freshwater flowed towards the sea (compare Figures 27b and 33b), thereby forcing freshwater that was recharged inland of the gallery into the horizontal well.

At the end of the pipe (x =100.5 m), the head was 48.6823 m, while at the beginning of the pipe (x = 0.5 m), the head was 48.6821 m, indicating a minuscule head loss of 1×10^{-4} m along the pipe, as obtained in the freshwater-only model. The head in the abstraction well was 48.6818 m, showing a 2 mm head loss between the pipe and the abstraction well, also consistent with the freshwater-only case. The abstraction well water level was lower than the head in the aquifer surrounding the abstraction well by approximately 0.028 m. The maximum drawdown in Case B was 0.096 m, recorded at the abstraction well location (i.e., recalling that *drawdown* here is the difference between the Case B water level in the abstraction well and the aquifer head at the abstraction well location in Case 0). Drawdown at the beginning (x = 0.5 m) and the end (x = 100.5 m) of the pipe was 0.068 m and 0.0524 m, respectively.

The total volume of freshwater in Case B was computed to be 130,090 m^3 (8.07 m average freshwater lens thickness), reflecting a 12.1% reduction compared to Case 0.

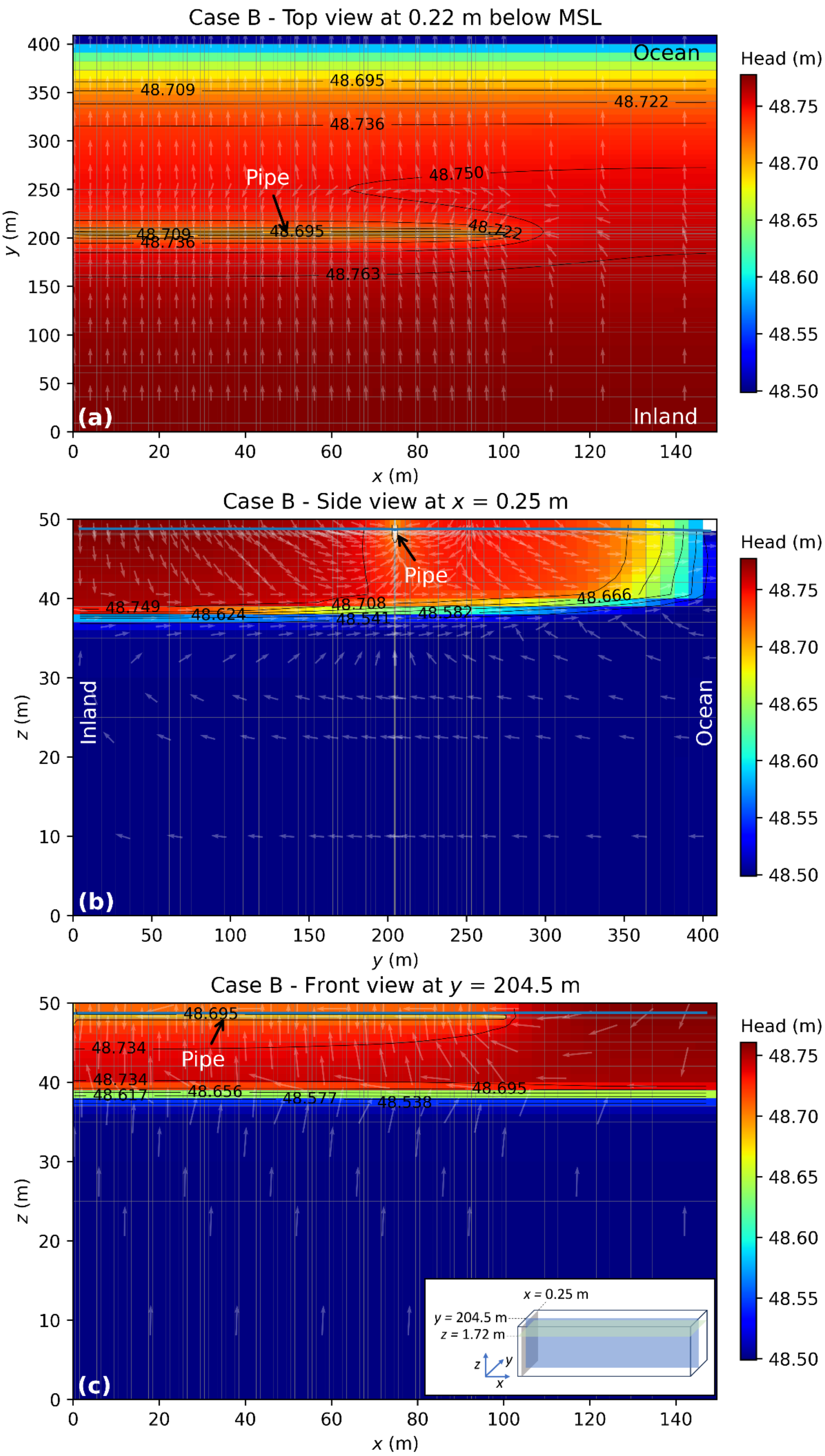

Figure 33. Head distribution for Case B. Black lines show the head contours, while the blue line indicates the water table. White arrows depict flow directions (arrows are shown for only a portion of the model cells). Heads are shown in 2D planes that pass through the centre line of the horizontal well and/or the infiltration gallery.

7.2.3 Cases 1 to 12

The steady-state concentration distributions for Cases 1 to 12 are illustrated in Figures C2 to C13 (Appendix C), while the corresponding steady-state head are depicted in Figures D2 to D13 (Appendix D). The scenarios adopted in Cases 1 to 12 are described in Section 6.2.

The main observations for each case are summarised in the following tables. These encompass:

1. Elevation of salinity contours at the beginning of the pipe where it connects to the abstraction well (Table 15).
2. Total volume of freshwater within the aquifer before and after installation of the gallery (Table 16).
3. Equivalent average freshwater lens thickness after gallery installation (Table 16).
4. Concentration and salinity of extracted water and the concentration and salinity inside the pipe at its beginning and end points (Table 17).
5. Drawdown at the abstraction well and in the beginning and end of the pipe (Table 18).
6. Head values inside the pipe at its beginning and end points, along with the head loss between the pipe and the abstraction well (Table 19).

To quantify the impact of different modelling scenarios on the freshwater-saltwater interface, the elevation (measuring from the mean sea level) of the isochlor contours at the beginning of the pipe where it connects to the abstraction well was analysed. The beginning of the pipe was located at x = 0.5 m and y = 204.5 m in all cases except Case 9, where the pipe starts at x = 100.5 m and y = 204.5 m. The elevation data for four salinity contours (i.e., 0.05, 0.1, 0.5, 0.9) extracted simulated salinity distributions are summarised in Table 15.

Table 15. Elevation of salinity contours at the beginning of the pipe where it connects to the abstraction well (i.e., *x* = 0.5 m and *y* = 204.5 m for all cases, except Case 9 where the pipe starts at *x* = 100.5 m and *y* = 204.5 m). Note that the horizontal pipe ranges from 0.295 to 0.145 m below MSL, and so larger values indicate that salinity contours are below the pipe. The background colour of each cell indicates the cell value, where smaller values are red and larger values are green.

Scenario	Isochlor contour elevation (m BMSL)*			
	0.05	**0.1**	**0.5**	**0.9**
Case B	8.08	8.53	10.06	11.44
Case 1	8.97	9.20	10.45	11.74
Case 2	1.45	4.41	9.57	10.99
Case 3	8.18	8.74	10.23	11.61
Case 4	10.3	13.20	14.59	15.88
Case 5	8.08	8.53	10.06	11.44
Case 6	8.08	8.53	10.06	11.44
Case 7	8.77	9.14	10.38	11.70
Case 8	8.07	8.53	10.06	11.46
Case 9	8.20	8.60	9.89	11.70
Case 10	-0.09**	0.45	3.71	8.71
Case 11	1.63	8.19	9.67	10.89
Case 12	8.11	8.57	10.06	11.36

*m BMSL = metres below mean sea level.
**0.05 salinity contour exceeded MSL.

In Table 15, the elevations of the 0.05-isochlor contour for Cases B, 3, 5, 6, 8 and 12 closely align, ranging from 8.07 to 8.20 m BMSL (below mean sea level). This suggests that variations in the hydraulic conductivity of the Holocene layer (as seen in Case 3) and modifications to the infiltration gallery (such as reducing the slotted pipe conductance in Case 5, using a geofabric layer instead of a plastic layer in Case 6, employing a smaller diameter of slotted pipe in Case 8, adopting two abstraction wells instead of one central abstraction well in Case 9, or implementing a branched slotted pipe in Case 12) caused only minor shifts in the vertical distribution of salinities beneath the abstraction well. However, other changes exerted more significant influences on salinities beneath the abstraction well. For example, reducing the extraction rate in Case 1 caused salinity contours to occur at lower elevations (e.g., the 0.05-isochlor was 0.89 m deeper). Case 4, in which the depth of the Holocene layer was thicker, exhibited the greatest freshwater thicknesses, with the 0.05-isochlor occurring some 2.2 m deeper (10.3 m BMSL) than in Case B. The longer pipe used in the infiltration gallery of Case 7 also produced a deeper 0.05-isochlor contour (8.77 m BMSL).

The results in Table 15 show that infiltration galleries with pipes that are perpendicular to the shoreline (Cases 10 and 11) produced 0.05-isochlor contours that were much higher in elevation (0.09 m above mean seawater level and 1.63 m BMSL, respectively). The former is higher than the base of the horizontal pipe. The greater extraction rate of Case 2 also produced a 0.05-isochlor contour that was much higher than Case B. Similar observations can be made for other contours based on the results presented in Table 15.

Table 16 presents the freshwater volume before and after gallery installation, along with percentage changes. The mean freshwater lens thickness is also provided. The freshwater volume in the aquifer for each modelling scenario was calculated using the method outlined in Section 7.2.1. This calculation considered cells with concentrations less than or equal to 0.01 ($C \leq 0.01$) both before and after installation of galleries.

Table 16. Freshwater volume in the aquifer and the mean freshwater lens thickness before and after installation of an infiltration gallery. The freshwater volume was calculated for cells with concentrations less than or equal to 0.01 ($C \leq 0.01$). Background colours reflect cell values where red values are larger and green values smaller (in magnitude).

Scenario	Aquifer surface area (m^2)	Freshwater volume before gallery (m^3)	Freshwater volume after gallery (m^3)	Average freshwater lens thickness after gallery (m)*	Percent change (%)**
Case B	61,146	147,948	130,090	7.1	-12.1
Case 1	61,146	147,948	142,983	7.8	-3.46
Case 2	61,146	147,948	118,198	6.4	-20.1
Case 3	61,146	148,208	138,189	7.5	-6.76
Case 4	61,146	211,932	180,241	9.8	-15.0
Case 5	61,146	147,948	130,091	7.1	-12.1
Case 6	61,146	147,948	130,046	7.1	-12.1
Case 7	102,046	247,970	236,015	7.7	-4.82
Case 8	61,146	148,200	130,336	7.1	-12.1
Case 9	61,146	147,949	121,471	6.6	-17.9
Case 10	61,146	90,233	70,865	3.9	-21.5
Case 11	123,314	257,472	243,613	6.6	-5.38
Case 12	61,146	148,171	130,574	7.1	-11.9

*Calculated as [(freshwater volume after gallery – freshwater volume before gallery)/freshwater volume before gallery] × 100%.
**Calculated as freshwater volume after gallery/aquifer surface area/porosity.

Table 16 shows that the volume of freshwater within the aquifer reduced from the operation of an infiltration gallery by between 3.5% and 21.5% across the 13 cases. This reduction occurs because of saltwater up-coning, increased freshwater-saltwater mixing, lateral seawater intrusion within the coastal fringe, and drawdown. These processes are apparent in the concentration distributions depicted in Figures C2 to C13 (Appendix C).

Table 16 shows that the installation galleries of Cases B, 5, 6, 8 and 12 had similar impacts on the stored freshwater volume. Decreases in freshwater volume in these cases amounted to around 12%. These cases overlap with those that caused similar variations to the salinity beneath the abstraction well, except Case 3 (half the *K* of Case B) had a much smaller impact on the lens volume than Cases B, 5, 6, 8 and 12. This is the consequence of a smaller lateral extent of drawdown (causing less saltwater rise) in aquifers of lower *K*.

The smallest changes in freshwater volume were observed in Case 1 (-3.46%), Case 7 (-4.82%) and Case 11 (-5.38%). This is expected in Case 1 due to the reduced rate of pumping. The reduced drawdown due to the longer pipe (relative to Case B) in Case 7 also created a greater storage freshwater volume. Both these cases also produced deeper 0.05-isochlor contours (Table 15). Case 11 (pipe perpendicular to the shoreline) showed contradictory behaviour, in that the 0.05-isochlor salinity rose to close to the base of the gallery, but the freshwater lens was more voluminous (pumping caused by 5.38% decline in the freshwater volume) compared to Case B (12.1% freshwater storage decline). This occurred because the drawdown in Case 11 was focussed on the central part of the model domain (rather than distributed parallel to the coast), leaving much of the saltwater body only slightly changed due to pumping. Similarly, using the infiltration gallery perpendicular to the shoreline with a longer pipe distance from the shoreline (Case 11) also shows improvement, with the freshwater volume reduced by only 5.38%.

Infiltration galleries in Cases 2, 4, 9, and 10 caused the largest freshwater storage losses (20.1%, 15.0%, 17.9% and 21.5%, respectively) from pumping. For Cases 2 and 10, this is consistent with the shallow depth of salinity contours (Table 15), whereas Cases 4 and 9 involved deeper salinity contours and yet the freshwater volume experienced larger losses compared to other cases. This indicates that freshwater lenses in thicker aquifers (Case 4) may show larger reductions in storage, despite weaker localised up-coning. This is caused by the larger transmissivity of the freshwater zone propagating drawdown (and therefore lens thinning) further afield. The infiltration gallery that is closer and perpendicular to the shoreline (Case 9) produced similarly disparate results (smaller freshwater volume but relatively deeper salinity isochlors). These results may be caused by movement of the seawater wedge in the coastal fringe that falls within the gallery's footprint (of Case 9) and that adds to the freshwater losses (from lens thinning) in a way that galleries further from the coast do not.

A critical parameter for evaluating infiltration gallery performance is the salinity of the extracted water. This was obtained by averaging salinities of the pumping cells within the abstraction well. Table 17 provides both relative (dimensionless) and absolute (in µS/cm) salinity values for each modelling scenario. The salinity at the beginning (x = 0.5 m for all cases except Case 9 where the pipe began at x =100 m) and the end of the pipe (x = 100.5 m for all cases except Case 9, where the end of the pipe was located at x = 0 m) are also presented.

Table 17. Salinity of extracted water and within the horizontal pipe at its beginning and end points. Background colours are indicative of cell values, where red indicates larger values and green shows smaller ones.

Scenario	Relative salinity, *C* (-)			Salinity (µS/cm)*		
	Extracted water	Pipe beginning	Pipe end	Extracted water	Pipe beginning	Pipe end
Case B	0.0109	0.0109	1.40×10^{-4}	1094	1094	508
Case 1	0.0006	0.0006	1.27×10^{-8}	533	533	500
Case 2	0.0367	0.0367	1.60×10^{-3}	2500	2500	587
Case 3	0.0103	0.0103	1.20×10^{-4}	1061	1061	507
Case 4	0.0039	0.0039	5.35×10^{-7}	713	713	500
Case 5	0.0109	0.0109	1.40×10^{-4}	1094	1094	508
Case 6	0.0108	0.0108	1.40×10^{-4}	1089	1089	508
Case 7	0.0008	0.0008	2.44×10^{-8}	544	544	500
Case 8	0.0108	0.0108	1.90×10^{-4}	1089	1089	510
Case 9	0.0179	0.0186	2.87×10^{-2}	1476	1514	2064
Case 10	0.0992	0.0992	3.61×10^{-2}	5906	5906	2467
Case 11	0.0142	0.0142	4.00×10^{-4}	1274	1274	522
Case 12	0.0112	0.0112	7.51×10^{-5}	1110	1110	504

*Calculated as $C \times (EC_s - EC_r) + EC_r$, where C (-) represents the relative concentration, EC_s = 55,000 µS/cm is the salinity of seawater and EC_r = 500 µS/cm is the assumed salinity of recharge.

The results in Table 17 show that the salinities of the extracted water align with those at the beginning of the pipe (where it connected to the abstraction well), as expected, with the only exception being Case 9. The concentration at the beginning of the pipe is approximately 4% higher than the concentration of the extracted water in Case 9. In all cases except Case 9, the concentration along the pipe increases in the direction of flow (from the pipe end to the pipe beginning) caused by the entry of higher-salinity water into the slotted pipe relative to the water already in the pipe. Conversely, in Case 9, the concentration along the slotted pipe decreases, indicating the influx of fresher water into the pipe closer to the abstraction well. This can be attributed to the use of two abstraction wells instead of one central abstraction well in Case 9. This causes (fresher) groundwater to be drawn into the horizontal pipe from beyond the pipe's extent (longitudinally; near the abstraction well; see Figure 23) that isn't possible in other cases because of the no-flow symmetry boundary (see Figures 11 and 24).

The salinity of extracted water in Cases B, 3, 5, 6, 8 and 12 falls within a small range (relative salinities of 0.0103 to 0.0112). These are the same cases that caused 0.05-isochlor contours to occur at similar depths. Thus, there is a close correlation between up-coning and the salinity of the produced water, as expected. Similarly, Cases 1, 4 and 7 showed the lowest produced-water salinities (relative salinities ranging between 0.0006 and 0.0039) while being the cases that produced the deepest isochlor contours.

The highest salinities were obtained from Cases 2, 9, 10 and 11. Of these, Cases 2, 10 and 11 produced the shallowest salinity isochlors, so the high salinities of produced water are the result of up-coning. Cases 2, 9 and 10 produced the most thinning of the freshwater lens.

Therefore, with less freshwater stored in the aquifer, the infiltration galleries in these cases extracted more of the saline groundwater. The produced water salinity was equal to or exceeded 2500 μS/cm in Cases 2 (150% higher pumping than Case B) and 10 (perpendicular to the shoreline and closer to it), indicating that these systems would require adjustment to the extraction rate to secure a potable supply.

Although the drawdown in infiltration galleries is generally small, the values obtained in the model for the different cases are nonetheless of interest. Table 18 lists drawdown within the abstraction well and at the pipe beginning and end. Drawdown is the difference between water levels in the pipe (including the abstraction well) and the water table in the aquifer at the site of infiltration gallery before it was installed.

Table 18. Drawdown at the abstraction well, beginning and end of the pipe. The background colour of each cell indicates the cell value, where red identifies larger values and green smaller ones.

Scenario	Drawdown (m)*		
	Abstraction well	Pipe beginning	Pipe end
Case B	0.096	0.068	0.052
Case 1	0.046	0.032	0.025
Case 2	0.151	0.110	0.084
Case 3	0.170	0.113	0.084
Case 4	0.106	0.078	0.060
Case 5	0.096	0.068	0.052
Case 6	0.091	0.087	0.081
Case 7	0.049	0.034	0.027
Case 8	0.099	0.068	0.055
Case 9	0.096	0.066	0.061
Case 10	0.165	0.132	0.089
Case 11	0.093	0.064	0.046
Case 12	0.088	0.063	0.049

*Calculated as the drop in water table in the gallery relative to the water table height prior to gallery installation.

In each case, the largest drawdown occurs in the abstraction well, while the least drawdown occurs in the end of the pipe that is furthest from it, as expected. All drawdown values in Table 18 are less than or equal to 0.17 m. This makes the field observation of drawdown challenging in atoll islands (due to the need to capture small head drops in aquifers commonly subjected to tides and other temporal variability) relative to the measurement of up-coning, which manifests as changes in the elevations of isochlor contours by several metres (e.g., Table 15). In Table 18, drawdown was similar in Cases B, 4, 5, 6, 8, 9, 11 and 12, ranging from 0.088 m to 0.106 m. Of these, Cases B, 5, 6, 8, 9 and 12 had intermediate saltwater up-coning (Table 15), Cases B, 5, 6, 8 and 12 had intermediate impacts on the average lens thickness (Table 16), and Cases B, 5, 6, 8 and 12 had intermediate produced-water salinities (Table 17). Thus, only Cases 4 (50% thicker Holocene thickness) and 11 (gallery set perpendicular to the shoreline) show divergent salinity behaviour relative to the drawdown results. Case 4 had lower produced-water salinities versus the drawdown than other cases due to the greater depth to saltwater in the deeper Holocene layer. Case 11 had a slightly higher produced-water salinity, reduced impact on the average lens thickness, and stronger up-coning. This can be explained by the capture zone of the Case 11 gallery including part of the saltwater wedge, but otherwise, the hydraulics is not dissimilar to many of the other cases (see Table 18).

In Table 18, the lower drawdown in Cases 1 and 7 is consistent with the lower pumping rate (Case 1) and the longer pipe (Case 7). The highest drawdowns were caused by higher pumping (Case 2), lower Holocene K (Case 3), and the gallery being closer to the shoreline (Case 10) where the fixed head of the ocean mitigates drawdown (at the expense of saltwater intercepting the gallery; Table 17).

Table 19 shows heads in the horizontal pipe, and head losses in the pipe and between the pipe and the abstraction well. These are included in the interests of reporting the internal hydraulics of the infiltration gallery, although the small values of head losses effectively fall within the margin of error of any measurement that could possibly be taken in the field.

Table 19. Heads in the slotted, horizontal pipe, as well as head losses along the pipe and between the pipe and the abstraction well. Background colours reflect cell values.

Scenario	Head (m)		Head loss (m)	
	Pipe beginning	Pipe end	Along pipe	Pipe-to-abstraction well
Case B	48.682	48.682	2.2×10^{-4}	2.1×10^{-4}
Case 1	48.732	48.732	4.2×10^{-5}	1.0×10^{-4}
Case 2	48.627	48.628	5.4×10^{-4}	3.1×10^{-4}
Case 3	48.621	48.621	2.0×10^{-4}	2.0×10^{-4}
Case 4	48.792	48.792	1.7×10^{-4}	2.1×10^{-4}
Case 5	48.682	48.682	2.2×10^{-4}	2.1×10^{-4}
Case 6	48.687	48.687	2.3×10^{-4}	2.1×10^{-4}
Case 7	48.729	48.729	2.4×10^{-4}	2.1×10^{-4}
Case 8	48.679	48.680	6.8×10^{-4}	4.0×10^{-4}
Case 9	48.682	48.682	$<1 \times 10^{-5}$	3.7×10^{-4}
Case 10	48.555	48.556	5.4×10^{-4}	2.0×10^{-4}
Case 11	48.672	48.672	2.5×10^{-4}	2.0×10^{-4}
Case 12	48.691	48.691	2.3×10^{-4}	2.1×10^{-4}

Table 19 reports miniscule values for head losses within pipes and the abstraction well of the infiltration galleries considered in this study, including values that are below the precision of reporting from MODFLOW (i.e., in Case 9). Head losses between the pipe and the abstraction well are larger than losses along the pipe because of the smaller *K* (selected as a trade-off between a lower value for numerical stability and a higher value to represent free-flowing water), as discussed in Section 7.1.1.

7.2.4 Comparing the performance of simulated infiltration galleries

The key findings from the 13 simulated cases of infiltration galleries, consisting of alternative design and hydrogeological conditions, were integrated using a scoring approach to rank the cases and the changes in terms of relevant performance indicators (PIs). These included measures of up-coning, volume of freshwater stored in the aquifer, drawdown, and the produced-water salinity. The analysis evaluated these PIs relative to the base case (Case B). An initial review of differences between the PIs of the difference cases is provided in Table 20. As head losses were small across all cases (Table 19), these parameters were not taken into consideration in the evaluation of PIs. The colour shading in Table 20 recognises where the listed case produced "better" or "worse" conditions – for example, a smaller drawdown or produced-water salinity are shaded green, while a smaller depth to the 0.05-salinity contour or average freshwater lens thickness are shaded red.

Table 20. Results of key performance indicators (PI) from modelling scenarios, taken relative to the base case model (Case B). The cell shading of green-to-red represents a sliding scale between "better" to "worse" conditions in the listed case relative to Case B.

	Difference in PI relative to Case B* (%)			
	Depth to the 0.05-salinity contour**	**Average freshwater lens thickness**	**Produced-water salinity**	**Drawdown at extraction well**
Case 1	11	8.3	-51	-52
Case 2	-82	-7.7	129	57
Case 3	1.3	5.2	-3	77
Case 4	26	32	-35	10
Case 5	-0.0	0.0	0.0	0.0
Case 6	-0.0	0.0	-0.5	-5.2
Case 7	8.6	6.9	-50	-49
Case 8	-0.1	0.0	-0.5	3.1
Case 9	1.5	-5.7	35	0.0
Case 10	-101[#]	-38	440	72
Case 11	-80	-5.0	16	-3.1
Case 12	0.4	0.2	1.5	-8.3

*Calculated as [(value for each case-value for Case B)/value for Case B] × 100.
**Depths are elevations that use the datum of metres below MSL
[#]0.05-isochlor of Case 10 exceeded 0 m MSL

The following key points are derived from the results provided in Table 20:

1. The two cases in which the pumping rate was changed by 50%, Cases 1 and 2, produced opposite results in terms of the four PIs, as expected. While the drawdown and average freshwater lens thickness were roughly the same in magnitude (but opposite in direction), up-coning beneath the gallery and the salinity of produced water were contrasting in magnitude, with much larger changes caused by increasing the extraction rate by 50%. This demonstrates the non-linear response of salinity to changes in pumping rates, even though the hydraulic response was approximately linearly related to the pumping rate across the three cases (Cases B, 1 and 2). Continued monitoring of an infiltration gallery working under the more complicated conditions of a field situation will no doubt be affected by other factors, such as tidal processes and time-varying recharge, making the pumping-salinity relationships even more complicated. Nevertheless, efforts to understanding this relationship are encouraged to help manage the operation of galleries, but also, if the freshwater lens is monitored concurrently with measurements of the infiltration gallery salinity (and drawdown, etc.), links between these factors will help managers protect the integrity of the freshwater lens.

2. Changes to the Holocene sediment properties represented in Cases 3 (*K* lowered by 50%) and 4 (thickness increased by 50%) produced changes that were the same in direction (decreasing or increasing each of the four PIs) but different in magnitude. This is surprising given that Case 3 involved a lower transmissivity while Case 4 had a higher transmissivity (changed by the same magnitude of 50% but opposite in direction). That is, a lower *K* or deeper Holocene layer thickness produced less up-coning (deeper 0.05-isochlor contours), a thicker freshwater lens (on average), lower-salinity produced water, but greater drawdown. The magnitudes of effects were contrasting, with larger influence on the IPs of up-coning, lens thickness and produced-water salinity in Case 4, while the drawdown was affected more so in Case 3. Given these mixed results, it may be necessary to run these cases for longer timeframes because a lower *K* or thicker sediments will require more time to reach steady-state conditions.
3. Varying the pipe/gravel pack/plastic layer design in Cases 5 (pipe slots less permeable), 6 (geofabric instead of plastic layer), 8 (pipe diameter reduced) had minimal impact on the PIs (<6% changes for all cases and PIs), mostly because the resistance of these features is considerably lower than the resistance to flow in the aquifer, and therefore, several order-of-magnitude change is likely needed before significant impact to PIs occurs. We did not examine the effect of geofabric clogging because information related to the hydraulics of this problem was not available in previous studies.
4. Changes to the extraction rate per length of gallery was assessed in two cases: Case 1 (50% lower pumping) and Case 7 (horizontal pipe twice as long), with both cases adopting the same pumping/gallery length ratio (i.e., half that of Case B). As expected, the PI results were the same in direction (less up-coning, thicker lens, lower produced-water salinity, less drawdown) and the magnitude of changes were rather similar (see Table 20). Case 1 had a slightly larger effect on all four PIs than increasing the length of the gallery, but the numbers were rather close and within the margins-of-error that arise from the assumptions of the model. While this might seem prima facie that doubling the gallery length or building two galleries has the same effect, the results of Case 2 are important to note here, because increasing the pumping had a more profound impact on salinities than decreasing the pumping by the same % (50%; Cases 1 and 2). Therefore, facing the option of building two galleries or pumping twice as much from one gallery that is twice as long requires individual analysis, but we expect that two galleries pumping half as much as the extraction from a single gallery twice as long is preferred given that doubling the pumping produced an ‘over-reaction’ in terms of the salinity response, at least for the gallery length of 100 m (see Table 11) adopted in Cases 1 and 2. Regardless, investigation is needed in each case that includes an assessment of construction, maintenance and running costs, amongst other practical considerations.
5. Adding a second abstraction well to the infiltration gallery (Case 9) had minor effects on up-coning, the lens thickness and drawdown (<6% change), but caused a larger produced-water salinity by 35%, although the approximate salinity in Case 9 (1476 μS/cm) is well below the suggested limit for potable water of 2500 μS/cm. This result is challenging to reconcile with the hydraulics of the problem, because the head drop in

the pipe is miniscule, and so we expected limited changes arising from moving the abstraction well location from a theoretical perspective. Further investigation of this outcome (which included a thinner freshwater lens in Case 9) is warranted.

6. The implementation of branched-pipe networks and galleries perpendicular to the shoreline were considered in Cases 10 (perpendicular to, and closer to, the shoreline), 11 (perpendicular to the shoreline) and 12 (branched pipe). Adverse outcomes arose from the installation of infiltration galleries perpendicular to the shoreline, especially where the gallery-to-shoreline distance was smaller (Case 10) than Case B. This result highlights the influence of the freshwater lens having a near-uniform thickness beyond the coastal fringe (e.g., see Figure 30), and therefore, the distance from the shoreline only influences the PIs where the gallery is close enough to the coast that it interacts with the saltwater wedge (which was approximately 60 m from the coast; Section 7.2.1) under pre-development conditions. The gallery in Case 10 had an end point at 50 m from the coast. Even though the nearest point of Case 11 (perpendicular) was approximately the same distance to the shoreline as Case B (parallel), Case 11 showed a worse performance in terms of up-coning, the lens thickness and the produced-water salinity. Galleries situated parallel to the coast out-perform those that are perpendicular because the former more effectively capture submarine groundwater discharge that is otherwise lost to the sea if the gallery is placed along a flow line (i.e., galleries that are perpendicular to the coast are oriented in the direction of groundwater flow in pre-development cases; see Figure 31a). This outcome helps to explain why adding branches to the gallery in Case 12 had only a small effect on salinity-based PIs (2% changes), with the drawdown smaller by 8.3%. Thus, adding branches that are perpendicular to the shoreline appears to provide little additional benefit for the cases we considered, even though the extra construction costs are likely to be significant (48 m of extra horizontal pipe in Case 12). Under real-world conditions, the lenses of atolls are often irregularly shaped due to topographical variability and its effect on evapotranspiration, amongst other factors. Thus, infiltration galleries of complex alignments may prove to be more effective where the shape of lenses is well constrained (and irregular), even though we found minimal benefits from branched-galleries in the current study.

7.2.5 Discussion of other effects on infiltration gallery performance

The models developed in this study neglect several factors likely to be influential in the performance of infiltration galleries, including (a) intra-layer heterogeneities (e.g., reef-flat plate, local-scale sediment variability, karst conduits in the Pleistocene limestone, etc.), (b) tidal effects, (c) temporal variability in rainfall, (d) temporal variability in gallery extraction rates, (e) episodic events, such as storms, (f) impact of private extraction by landholders, (g) topographic variability, and in particular, its influence on evapotranspiration, and (h) land-use change, including the clearing of vegetation and a multitude of anthropogenic activities. Many of these processes will create a more dispersive lens, which is likely to cause infiltration galleries to show poorer performance in terms of the previous IPs, especially those related to salinity, because a small amount of mixing with seawater renders the produced water non-potable. For example, if recharge water is presumed to have a salinity of 500 μS/cm and seawater salinity is 55,000 μS/cm, then a sample of groundwater that contains 3.7% of seawater has a salinity of 2500 μS/cm. For this reason, greater research effort is warranted to explore the process creating more dispersive mixing zones to seek opportunities to mitigate these where it is possible. Where the freshwater-seawater mixing zone is wider (e.g., where the tidal range is greater), the thickness of the Holocene sediments is probably more important, because this would allow wider mixing zones to be accommodated within the sediments more commonly associated with freshwater lenses.

Spatial variability in evapotranspiration, anticipated to arise from differences in vegetation type, soil type and/or topographic elevations, was also neglected in the current study. The latter may also play a role in controlling the distribution of any seawater over-wash during storm events. Given the shallow depth to the water table on atoll islands, evapotranspiration is likely a critical factor, including whether or not trees are able to extract directly from groundwater or require water in the unsaturated zone. Yet, the measurement of evapotranspiration is challenging, and rarely attempted, and the controls on its spatial and temporal variability are poorly constrained. Given the high salt-spray loads to atoll islands, evapotranspiration may also create regions where groundwater salinity is elevated due to evapo-concentration processes. An analysis of the potential for this to occur in atoll environments would help to understand the wider gamut of stresses on freshwater lenses in these settings. This would also help to guide decisions on vegetation management in parts of the island that are dedicated to groundwater extraction, given that clearing is often raised as a potential opportunity for enhanced recharge.

The current study did not examine the role of the Pleistocene hydraulic conductivity (K) on infiltration gallery performance, mainly because information on the hydraulic properties of these sediments is lacking. The high K of the Pleistocene layer generally causes truncation of the lens, and so a lower Pleistocene K is expected to allow for larger lenses to develop. As more field testing is undertaken of deeper sediment properties in atoll islands, the current modelling study can be extended to evaluate the role of Pleistocene properties (including spatial variability in the elevation of the Holocene-Pleistocene discontinuity).

The models described in this report adopted vertical shorelines, even though the coastal boundaries are sloping, often very gradually on the lagoon-side of atoll islands. This has the effect of amplifying tidal processes on the time-averaged groundwater head of the shoreline and may lead to complicated salinity patterns in the near-shore. These include an upper tidal-circulation cell that is susceptible to landward incursion under the effects of pumping. Without tides, a sloping boundary is expected to lead to similar results (in terms of the gallery IPs) to a vertical coastline, especially for thin aquifers or freshwater lenses, such as those on atoll islands.

Research on the design and analysis of infiltration galleries should consider three additional factors to those evaluated in the current study.

1. The stored volume of fresh groundwater is a function of the rate of fresh groundwater discharge to the sea, whereby reducing the seaward discharge leads to larger lenses and allows for greater rates of gallery extraction. This was revealed by the better performance of galleries that are parallel to the coast and therefore capture the seaward discharge of fresh groundwater over a longer stretch of shoreline. Galleries closer to the shoreline will capture more of the seaward freshwater discharge, but a limit is reached where the gallery starts to draw from the seawater wedge of the coastal fringe, impacting the salinity of produced water. Thus, the goal of infiltration gallery placement should be to draw from as close to the coast as possible while limiting saline water uptake. This type of optimisation is possible through an extension to the approach of the current study, although real-world conditions likely need to be accounted for due to variations in conditions between atoll settings.
2. The storage of freshwater in atoll island aquifers is reduced by freshwater-saltwater mixing, but this is rarely considered in water balance studies that lead attempt to determine the sustainable yield. Mixing will be enhanced by tidal fluctuations, but also by factors influenced by gallery operation, such as the intermittency of pumping and the rate of pumping versus the thickness of the lens (i.e., pumping from a thinner lens likely causes greater mixing). The losses from freshwater due to mixing needs further investigation because the practicality or benefits of reducing mixing losses is currently unclear.
3. Options to improve the performance of infiltration galleries through engineering intervention methods have previously been evaluated from only a theoretical standpoint. While options such as physical flow-barriers are perhaps limited due to the cost of construction, some measures to improve gallery performance exist that require smaller investments. For example, saltwater pumping (negative hydraulic barrier) has been shown to produce greater opportunities for freshwater storage in coastal aquifers, at least in continental settings Artificial recharge with treated wastewater to create hydraulic barriers is another technique that may have merit, at least in islands with larger, centralised populations with wastewater treatment systems, which may produce water of sufficient rates and quality for injection.

8. Conclusions and Recommendations

This document outlines the findings of three major project activities: (1) Literature review of gallery design that included a information provided by infiltration gallery operators during a visit to Kiritimati Island, (2) Development of conceptual models of atoll island hydrogeology and infiltration gallery design, and (3) Analysis of infiltration gallery performance using groundwater models.

The literature review (and operator information) found that the hydrogeological properties of atoll islands varying over one or two orders of magnitude, depending on the specific characteristic. This likely reflects the limited amount of aquifer testing for hydraulic properties, such as hydraulic conductivity and storativity. Solute transport parameters (dispersivity, porosity) are especially poorly constrained. Despite this, many atoll environments have similar water table depths, vegetation and soil types.

Even though island hydraulic properties are widely varying, infiltration galleries tend to have many similar attributes. Horizontal Pipe lengths tend varying from ~80 to 300 m, with 100 mm PVC a common material, although large-diameter (800 mm) concrete pipes and rectangular EcoBloc modules have also been used. Gravel packs are used almost ubiquitously, albeit gravel can be a difficult commodity to source on atoll islands. Extraction rates from infiltration galleries vary substantially (e.g., 0.06 to 2 m^3/d per metre length of horizontal pipe), although individual galleries are pumped at 25-140 m^3/d per gallery.

The conceptual model of an infiltration gallery installed in an atoll island adopted in this study consisted of a dual-aquifer (Holocene and Pleistocene layers) system with multiple galleries operating and a simple island geometry that allow axes of symmetry to be applied the led to smaller domains. Hydraulic characteristics incorporated in these models reflected typical atoll island parameters while also considering the specific conditions encountered on Kiritimati Atoll. The base case adopted a net recharge rate (400 mm/y) equal to 40% of the average rainfall, a 10-m thick Holocene layer of hydraulic conductivity equal to 10 m/d, and an island width of 818 m (half the island width was simulated). The infiltration of the base case adopted a continuous extraction rate of 20 m^3/d from a 100-m long pipe of 150 mm diameter surrounded by a 150 mm gravel pack and installed parallel to the shoreline and 204.5 m from it.

The four models codes applied in this study (MODFLOW, MODFLOW-CFP, MODPATH and SEAWAT) allowed for assessments of the hydraulics of the infiltration gallery design (MODFLOW), including with the horizontal pipe incorporate explicitly in the model (MODFLOW-CFP), as well as an evaluation of the capture zone of the gallery (MODPATH) and the influence of the gallery on freshwater-seawater interactions (SEAWAT). The MODFLOW-CFP results demonstrate that the implicit representation of the pipe (as a high-*K* feature) in MODFLOW is valid, as were the integration of multiple gallery components (e.g., the pipe slots and the internal pipe bore) into single model cells.

Comparisons of the groundwater captures zones (the region around a gallery in which groundwater flowed towards it) from particle tracking in MODPATH versus the location of groundwater divides (e.g., located at the peak of groundwater mounds) were insightful, showing the arcs that particles take in their movement towards the well, at least under the relatively simple conditions presented in freshwater-only models. Adding seawater to the model (i.e., in SEAWAT) caused the capture zone of the gallery to lengthen in the inland direction and contract in the seaward direction. In the base case (Case B), this led to a capture zone of 10s of metres seaward and ~200 m landward of the gallery. The establishment of buffer zones for restricting land-use activities in the vicinity of infiltration galleries would benefit from modelling of site-specific conditions using similar methods to those adopted in the current study.

The modelling analysis of 13 infiltration gallery scenarios produced important findings of relevance to the design of infiltration galleries. Key amongst these include:

1. Minimal head losses occur within the horizontal pipe and abstraction well.
2. The salinity of produced water was sensitive to the extraction rate, showing nonlinear relationships whereby increased extraction created a greater salinity increase than the drop in salinity accompanying a lower pumping rate.
3. Other performance indicators (PIs) of the system were also assessed, including the average freshwater lens thickness, the pumping-induced drawdown, and the up-coning of saltwater beneath the gallery. These showed mixed behaviour, in that a higher salinity did not always reflect a thinner freshwater lens or lower drawdown.
4. The results of other cases indicate complicated relationships between the distance between the infiltration gallery and the coast, the length and orientation of the horizontal pipe and the properties of the Holocene aquifer, although general trends are clear from the modelling results for most PIs. For example, longer horizontal pipes, lower pumping rates, a pipe orientation parallel to the coast, and an offset distance between the pipe and the coast that avoids the seawater wedge in the coastal fringe, all lead to improved gallery performance, in particular in terms of the produced-water salinity.
5. The costs of salinity improvements in terms of the pipe length (and other aspects the affect construction costs), infiltration gallery placement, and extraction rates need to be carefully weighed in developing designs for infiltration gallery networks.

The following recommendations for further work are proposed to enhance the outcomes of future modelling efforts:

1. Future field studies are required to provide more accurate details for stratigraphic information, aquifer hydraulic parameters, hydrological fluxes (e.g., evapotranspiration) and infiltration gallery key parameters. These should include data collection for salinity, water levels, tidal fluctuations, etc. within the aquifer to assist in the calibration of site-specific models.
2. Time-dependent measurements of pumping rates (from individual galleries), the produced water salinity and the drawdown in the abstraction well are important to support gallery operational decisions and to guide any changes to infrastructure.

3. Evaluations of tidal effects, rainfall variations, intermittent pumping, more complex shoreline geometries, and irregular layouts of infiltration gallery networks are needed as the next steps in developing an improved understanding of the effects of infiltration galleries on atoll freshwater lenses.
4. Particle-tracking analysis of density-dependent modelling would build on the analysis here of freshwater-only capture zones.
5. The salinity of rainfall, and the collection of other environmental tracers, would assist in constraining the hydrogeology of atoll island aquifers.

It is important to emphasise that these conclusions and suggestions are drawn from relatively simple conceptual models that are meant to represent generic conditions. Results will vary under real-world conditions, and thus, site-specific modelling is needed that captures the unique characteristics of each case.

9. Acknowledgements

We would like to express our gratitude to Tony Falkland and the SPC team, particularly Jake Ward, for their invaluable contributions and support during the PGGKE workshop. The advice and discussions with SPC staff were invaluable to the delivery of this report.

10. References

Abarca E., Carrera J., Sánchez-Vila X. and Dentz M. 2007. Anisotropic dispersive Henry problem. Advances in Water Resources 30(4): 913-926. DOI: 10.1016/j.advwatres.2006.08.005.

Alam K. and Falkland A. 1997. Vulnerability to climate change of the Bonriki freshwater lens, Tarawa. Prepared for the Ministry of Environment and Social Development Republic of Kiribati.

Alam K., Falkland A. and Mueller N. 2002. Sustainable yield of Bonriki and Buota freshwater lenses, SAPHE Project, Hydrogeology Component, Tarawa, Kiribati.

Altshul A. and Kishelev P. 1975. Hydraulics and Aerodynamics. Second edition. USSR: Stroisdat Publishing House.

America I., Zhang C., Werner A.D. and van der Zee, S.E.A.T.M. 2020. Evaporation and salt accumulation effects on riparian freshwater lenses. Water Resources Research 56(12): Art. no. e2019WR026380. DOI: 10.1029/2019WR026380

Anderson M.P., Woessner W.W. and Hunt R.J. 2015. Applied groundwater modeling: simulation of flow and advective transport, 2nd ed. Elsevier. Academic Press. DOI: 10.1016/C2009-0-21563-7

Anthony S.S. 2004. Hydrogeology of selected islands of the Federated States of Micronesia. p. 693–706. In: Geology and Hydrogeology of Carbonate Islands. Vacher H.L. and Quinn T.M. (Eds.). Amsterdam: Elsevier.

Ayers J.F. and Vacher H.L. 1986. Hydrogeology of an atoll island: A conceptual model from detailed study of a Micronesian example. Groundwater 24(2): 185-198. DOI: 10.1111/j.1745-6584.1986.tb00994.x

Barrash W., Clemo T., Fox J.J. and Johnson T.C. 2006. Field, laboratory, and modeling investigation of the skin effect at wells with slotted casing, Boise Hydrogeophysical Research Site. Journal of Hydrology 326(1-4): 181-198. DOI: 10.1016/j.jhydrol.2005.10.029

Bayer-Raich M., Jordana S., Jaime O.M., Lynch T.D., McGillicuddy K.B., Guimerà J. and Jaime M.J. 2022. Numerical Modeling of Head Losses in Different Types of Well Screens. Groundwater 60(6): 747-756. DOI: 10.1111/gwat.13196

Bear J. 1972. Dynamics of fluids in porous media. Amsterdam: Elsevier.

Bennett T.W. 1970. On the design and construction of infiltration galleries. Groundwater 8(3): 16-24. DOI: 10.1111/j.1745-6584.1970.tb01304.x

Bosserelle A., Jakovovic D., Post V.E.A., Galvis Rodriguez S., Werner A.D. and Sinclair P. 2015. Assessment of sea-level rise and inundation effects on Bonriki freshwater lens, Tarawa Kiribati: groundwater modelling report. Report for Bonriki Inundation Vulnerability Assessment Project. Geoscience Division Technical Report. Secretariat of the Pacific Community.

Bourrouilh-Le Jan F.G. 1998. The role of high-energy events (hurricanes and/or tsunamis) in the sedimentation, diagenesis and karst initiation of tropical shallow water carbonate platforms and atolls. Sedimentary Geology 118(1-4): 3-36. DOI: 10.1016/S0037-0738(98)00003-7

Bresciani E., Ordens C.M., Werner A.D., Batelaan O., Guan, H. and Post V.E.A. 2014. Spatial variability of chloride deposition in a vegetated coastal area: Implications for groundwater recharge estimation. Journal of Hydrology 519: 1177-1191. DOI: 10.1016/j.jhydrol.2014.08.050

Bryan E., Meredith K.T., Baker A., Post V.E.A. and Andersen M.S. 2016. Island groundwater resources, impacts of abstraction and a drying climate: Rottnest Island, Western Australia. Journal of Hydrology 542: 704-718. DOI: 10.1016/j.jhydrol.2016.09.043

Buddemeier R.W. and Oberdorfer J.A. 2004. Hydrogeology of Enewetak Atoll. p. 667–692 In: Geology and Hydrogeology of Carbonate Islands. Vacher H.L. and Quinn T.M. (Eds.). Amsterdam: Elsevier.

Chen N.H. 1979. An explicit equation for friction factor in pipe. Industrial and Engineering Chemistry Fundamentals 18(3): 296-297. DOI: 10.1021/i160071a019

Clemo T. 2006. Flow in Perforated Pipes: A Comparison of Models and Experiments. SPE Production & Operations 21 (02): 302-311. DOI: 10.2118/89036-PA

Custodio Gimena E. and Bruggeman G.A. 1987. Groundwater Problems in Coastal Areas. UNESCO. IHP, Studies and report in hydrology. Imprimerie Bietlot Frères, Fleurus, Belgique, 596 p. https://unesdoc.unesco.org/ark:/48223/pf0000074510

DEPS (Delivering Economic Piping Solutions). 2023. Monitoring Well Products. https://deps.com.au/our-products/environmental-well-products/

Domenico P.A. and Schwartz F.W. 1990. Physical and Chemical Hydrogeology. John Wiley & Sons, New York, 824 p.

Falkland A.C. 1991. Hydrology and Water Resources of Small Islands: A Practical Guide. A Contribution to the International Hydrological Programme (IHP). UNESCO Press, Paris, France.

Falkland A.C. 1992. Review of Tarawa freshwater lenses, Republic of Kiribati. Report HWR92/681. Hydrology and Water Resources Branch, ACT Electricity and Water. Prepared for the Australian International Development Assistance Bureau.

Falkland A.C. 1996. South Pacific Applied Geoscience Commission. Report on Appropriate Technologies for Freshwater Development and Management on Small Islands for UNEP Project (Technologies for Maximising and Augmenting Freshwater Resources in Small Islands), Hydrology Services ACTEW Corporation.

Falkland A.C. 1999. Cocos (Keeling) Islands, Guidelines for Water Supply Galleries – Revision 1. Prepared by GHD Pty Ltd and Territories Office, Department of Transport and Regional Services EHYD99/02.

Falkland A.C. 2011. Pacific Adaptation Strategy Assistance Program. Report on Water Security & Vulnerability to Climate Change and Other Impacts in Pacific Island Countries and East Timor, prepared by Falkland A.C. on behalf of GHD Pty Ltd for Department of Climate Change & Energy Efficiency.

Falkland A.C. and Brunel J.P. 1993. Chapter 10: review of hydrology and water resources of the humid tropical islands. In: Bonell, M., Hufschmidt, M.M., Gladwell J.S. (Eds.), Hydrology and Water Management in the Humid Tropics, Hydrological Research Issues and Strategies for Water Management. Cambridge University Press/IAHS, Cambridge, pp. 135–163.

Falkland A.C., White I. and Turner B. 2023. Kiribati SAPHE Project, Report on AbaTao-Tabiteuea Groundwater Investigations, Tarawa, Kiribati. For Original Engineering Consultants, Osaka, Japan and SAPHE Project Management Unit, Bairiki, Tarawa.

Falkland A. and Woodroffe C. 1997. Geology and hydrogeology of Tarawa and Christmas Island, Kiribati. p. 577–610. In: Geology and hydrogeology of carbonate islands. Vacher H.L. and Quinn T.M. (Eds.). Amsterdam: Elsevier.

Fetter C.W. 2001. Applied hydrogeology (4th ed.). NJ: Prentice Hall Inc.

Genthon P., Wirrmann D., Hoibian T. and Allenbach M. 2008. Steady water level and temperature in a karstic system: The case of the coral Lifou Island (SW Pacific). Comptes Rendus Geoscience 340(8): 513-522. DOI: 10.1016/j.crte.2008.06.002

Gingerich S.B. 1996. Ground-water resources and contamination at Roi-Namur Island, Kwajalein Atoll, Republic of the Marshall Islands, 1990-91. Series Number 95-4275, USGS Publications Warehouse. DOI: 10.3133/wri954275.

Gou W. and Langevin C.D. 2002. User's Guide to SEAWAT: A Computer Program for Simulation of Three-Dimensional Variable-Density Ground-Water Flow. In: U.S. Geological Survey Techniques of Water-Resources Investigations, Book 6, Chapter A7, 77 p. DOI: 10.3133/twri06A7

Harbaugh A.W. 2005. MODFLOW-2005, the U.S. Geological Survey modular ground-water model - the Ground-Water Flow Process. In: U.S. Geological Survey Techniques and Methods 6-A16.

Hsleh P.A. and Freckleton J.R. 1993. Documentation of a computer program to simulate horizontal-flow barriers using the U.S. Geological Survey's modular three-dimensional finite-difference ground-water flow model. U.S. Geological Survey Open-File Report 92-477. Prepared in cooperation with the City of Santa Barbara, Sacramento, California, 37 p.

Hunt C.D. 1996. Ground-water resources and contamination at Kwajalein Island, Republic of the Marshall Islands, 1990-91. In: U.S. Geological Survey, Water-Resources Investigations Report 94-4248, Honolulu, Hawaii. DOI: 10.3133/wri944248

Hunt C.D. and Peterson J.F.L. 1980. Groundwater Resources of Kwajalein Island Marshall Islands. Report No. 126, Report Documentation from Water Resources Research Center, University of Hawaii at Manoa, 101 p. https://scholarspace.manoa.hawaii.edu/server/api/core/bitstreams/a911c66e-fb24-45bf-b631-b24c25423bf9/content

Jakovovic D., Werner A.D., de Louw P.G., Post V.E.A. and Morgan L.K. 2016. Saltwater upconing zone of influence. Advances in Water Resources 94: 75-86. DOI: 10.1016/j.advwatres.2016.05.003.

Jazayeri A., Solórzano-Rivas S.C., Sinclair P., Antoniou A., Irvine D.J. and Werner A.D. 2019. A Groundwater Modelling Investigation of Greywater Disposal. Flinders University and Secretariat of the Pacific Community (SPC). The World Bank Group, Washington DC, 100 p. https://openknowledge.worldbank.org/server/api/core/bitstreams/a62c48ac-3b1d-5131-8abc-99c60356a957/content

Jazayeri A., Werner A.D. and Cartwright N. 2021. Partially penetrating lake-aquifer interaction in a laboratory-scale tidal setting. Journal of Hydrology 603: Art. no 127080. DOI: 10.1016/j.jhydrol.2021.127080

Knight A.C., Werner A.D. and Morgan L.K. 2018. The onshore influence of offshore fresh groundwater. Journal of Hydrology 561: 724-736. DOI: 10.1016/j.jhydrol.2018.03.028.

Kuniansky E.L. 2016. Simulating groundwater flow in karst aquifers with distributed parameter models - Comparison of porous-equivalent media and hybrid flow approaches: U.S. Geological Survey Scientific Investigations Report 2016–5116, 14 p. DOI: 10.3133/sir20165116

Langevin C.D., Thorne D.T., Dausman A.M., Sukop M.C. and Gou W. 2008. SEAWAT Version 4: A computer program for simulation of multi-species solute and heat transport. In: US Geological Survey Techniques and Methods, Book 6, Chapter A22, 39 p. DOI: 10.3133/tm6A22

Maréchal J.C., Hakoun V. and Corbier P. 2022. Role of Reef-Flat Plate on the Hydrogeology of an Atoll Island: Example of Rangiroa. Water 14(17): Art no. 2695.DOI: 10.3390/w14172695

Moench A.F. 1984. Double-porosity models for a fissured groundwater reservoir with fracture skin. Water Resources Research 20 (7), 831–846. DOI: 10.1029/WR020i007p00831

Morris D.A. and Johnson A.I. 1967. Summary of hydrologic and physical properties of rock and soil materials as analyzed by the Hydrologic Laboratory of the U.S. Geological Survey, U.S. Geological Survey Water-Supply Paper 1839-D, 42p.

Morrison R.J. and Woodroffe C.D. 2009. The Soils of Kiritimati (Christmas) Island, Kiribati, Central Pacific: New Information and Comparison with Previous Studies 1. Pacific Science 63(3): 397-411. DOI: 10.2984/049.063.0308

Naranjo G., Cruz-Fuentes T., Cabrera M.D.C. and Custodio E. 2015. Estimating natural recharge by means of chloride mass balance in a volcanic aquifer: northeastern Gran Canaria (Canary Islands, Spain). Water 7(6): 2555-2574. DOI: 10.3390/w7062555

NJS. 2023. Project to provide planning guidance for the water supply project (phase-1). Project for water supply system reconstruction assistance in the Kingdom of Tonga.

NRW Specialists. 2021. Decca Well Design and Pipework Details – Sheet 1 of 2. Kiritimati Water Supply Improvement Project.

Ouyang L.B. and Aziz K. 1996. Steady-state gas flow in pipes. Journal of Petroleum Science and Engineering 14(3-4): 137-158. DOI: 10.1016/0920-4105(95)00042-9

Pauloo R.A., Fogg G.E., Guo Z. and Harter T. 2021. Anthropogenic basin closure and groundwater salinization (ABCSAL). Journal of Hydrology 593, Art. no. 125787. DOI: 10.1016/j.jhydrol.2020.125787.

Pollock D.W. 2016. User guide for MODPATH Version 7 - A particle-tracking model for MODFLOW. In: U.S. Geological Survey Open-File Report 2016–1086, 35 p. DOI: 10.3133/ofr20161086

Post V.E.A., Bosserelle A.L., Galvis S.C., Sinclair P.J. and Werner A.D. 2018. On the resilience of small-island freshwater lenses: Evidence of the long-term impacts of groundwater abstraction on Bonriki Island, Kiribati. Journal of Hydrology 564: 133-148. DOI: 10.1016/j.jhydrol.2018.06.015

Reilly T.E. and Goodman A.S. 1987. Analysis of saltwater upconing beneath a pumping well. Journal of Hydrology 89(3-4): 169-204. DOI: 10.1016/0022-1694(87)90179-X

Schneider S., Mallants D. and Jacques D. 2012. Determining hydraulic properties of concrete and mortar by inverse modelling. Material Research Society Proceedings, 1475: 367-372. DOI: 10.1557/opl.2012.601

Shoemaker W.B., Kuniansky E.L., Birk S., Bauer S. and Swain E.D. 2007, Documentation of a Conduit Flow Process (CFP) for MODFLOW-2005. U.S. Geological Survey Techniques and Methods, Book 6, Chapter A24, 50 p. DOI: 10.3133/tm6A24

Sinclair P., Singh A., Fielea Q., Hyland K. and Moala A. 2014. Assessing vulnerability and adaptation to sea-level rise: Lifuka Island Ha'apai, Tonga. B1: Physical resources, 1.2: Groundwater resources assessment. DOI: 10.13140/RG.2.1.4505.9923

Siwon Z. 1987. Solutions for lateral inflow in perforated conduits. Journal of Hydraulic Engineering 113(9): 1117-1132. DOI: 10.1061/(ASCE)0733-9429(1987)113:9(1117)

Snow D.T. 1968. Rock fracture spacings, openings, and porosities. Journal of the Soil Mechanics and Foundations Division 94(1): 73-91. DOI: 0.1061/JSFEAQ.0001097

Solorzano-Rivas S.C., Werner A.D. and Irvine D.J. 2021. Mixed-Convective Processes Within Seafloor Sediments Arising From Fresh Groundwater Discharge. Frontiers in Environmental Science 9: Art. no. 600955. DOI: 10.3389/fenvs.2021.600955

SOPAC. 2007. Annual Report Summary. Pacific Islands Applied Geoscience Commission. Suva, Fiji. https://library.sprep.org/sites/default/files/2021-04/SOPAC-annual-report.pdf

Stoddart D.R. 1975. Scientific Studies in the Southern Cook Islands: Background and Bibliography. Atoll Research Bulletin 190: 1-30. https://repository.si.edu/bitstream/handle/10088/34129/ARB_scientificstudies.pdf?sequence=1&isAllowed=y

UNEP. 1998. Source book of alternative technologies for freshwater augmentation in small island developing states. UNEP International Environmental Technology Centre. Osaka, Japan, 223 p.

WBG and ADB. 2021. Climate Risk Country Profile: Tuvalu (2021): The World Bank Group and the Asian Development Bank. https://climateknowledgeportal.worldbank.org/sites/default/files/2021-06/15824-WB_Tuvalu%20Country%20Profile-WEB.pdf

Werner A.D. 2017. On the classification of seawater intrusion. Journal of Hydrology 551: 619-631. DOI: 10.1016/j.jhydrol.2016.12.012

Werner A.D., Jakovovic D. and Simmons C.T. 2009. Experimental observations of saltwater up-coning. Journal of Hydrology 373(1-2): 230-241. DOI: 10.1016/j.jhydrol.2009.05.004

Werner A.D., Jazayeri A. and Ramirez-Lagunas M. 2020. Sediment mobilisation and release through groundwater discharge to the land surface: Review and theoretical development. Science of the Total Environment 714, Art. no. 136757. DOI: 10.3389/fenvs.2021.600955. Doi: 10.1016/j.scitotenv.2020.136757.

Werner A.D., Kawachi A. and Laattoe T. 2016. Plausibility of freshwater lenses adjacent to gaining rivers: Validation by laboratory experimentation. Water Resources Research 52(11): 8487-8499. DOI: 10.1002/2016WR019400

Werner A.D., Sharp H.K., Galvis S.C., Post V.E.A. and Sinclair P. 2017. Hydrogeology and management of freshwater lenses on atoll islands: Review of current knowledge and research needs. Journal of Hydrology 551: 819-844. DOI: 10.1016/j.jhydrol.2017.02.047

White F.M. 2016. Fluid Mechanics (8th ed). Secacus, United State: McGraw Hill Education.

White I. and Falkland A.C. 2004. Effects of Pumping from Infiltration Galleries on Crop Health and Production in Low Coral Islands: Groundwater Impacts. Report for ACIAR Project LWR1/2001/050, 37 p.

White I., Falkland A.C., Metutera T., Metai E., Overmars M. and Perez P. 2007. Climatic and Human Infl uences on Groundwater in Low Atolls. Vadose Zone Journal 6(3): 581-590. DOI:10.2136/vzj2006.0092

White I. and Falkland T. 2010. Management of freshwater lenses on small Pacific islands. Hydrogeology Journal 18(1): 227-246. DOI: 10.1007/s10040-009-0525-0

Wiener O. 1912. Abhandlungen der mathematisch, Physischen Klasse der Koniglichen S ¨ achsischen Gesellschaft der Wissenschaften 32, 509.

Witherspoon P.A., Wang J.S., Iwai K. and Gale J.E. 1980. Validity of cubic law for fluid flow in a deformable rock fracture. Water Resources Research 16(6): 1016-1024. DOI: 10.1029/WR016i006p01016

Xu Z., and Hu B.X. 2017. Development of a discrete-continuum VDFST-CFP numerical model for simulating seawater intrusion to a coastal karst aquifer with a conduit system. Water Resources Research 53: 688-711. DOI:10.1002/2016WR018758

Zimmerman R.W. and Bodvarsson G.S. 1994. Hydraulic Conductivity of Rock Fractures. Earth Sciences Division, Report no. LBL-35976, UC-800, Lawrence Berkeley Laboratory, University of California. https://inis.iaea.org/collection/NCLCollectionStore/_Public/26/034/26034259.pdf

11. Appendices

Appendix A – MODFLOW results utilising the equivalent hydraulic conductivity approach

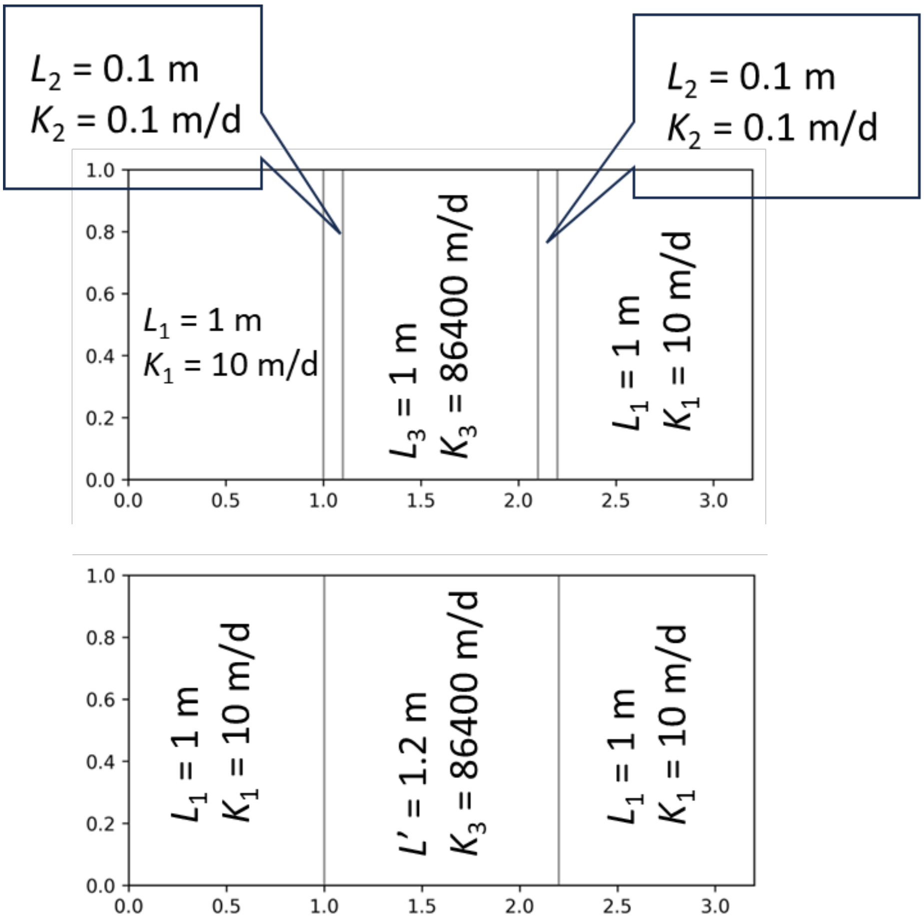

Figure A1. MODFLOW model properties comparing (a) a five-layer model and (b) a three-layer model. In panel (b), three layers from the middle of panel (a) are consolidated into a single layer, positioned at the centre of panel (b), with an equivalent hydraulic conductivity derived from the combined hydraulic conductivity of those three layers in panel (a) using Equation (21).

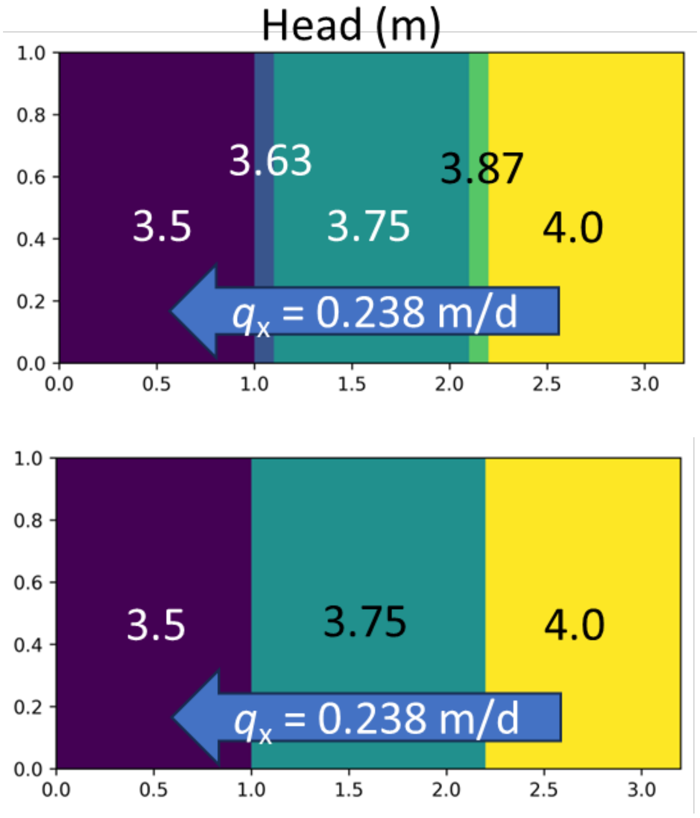

Figure A2. Head and flow results comparing (a) a five-layer model and (b) a three-layer model.

Appendix B – Summary of model scenarios

Table B1. Summary of model scenarios utilised in the SEAWAT variable-density simulations for this study.

Scenario	Component*			
	Aquifer	Infiltration gallery		
		Pipe	Filter	Abstraction well/sump
Case 1	As per Case B (Table 11)	K_p = 5.6 × 10^8 m/d, K_{sp} = 15,147 m/d, K_{ep} = 142,265 m/d; Other parameters as per Case B (Table 11)	As per Case B (Table 11)	Q = 10 m^3/d; Other parameters as per Case B (Table 11)
Case 2	As per Case B (Table 11)	K_p = 2.6 × 10^8 m/d, K_{sp} = 14,975 m/d, K_{ep} = 140,657 m/d; Other parameters as per Case B (Table 11)	As per Case B (Table 11)	Q = 30 m^3/d; Other parameters as per Case B (Table 11)
Case 3	Holocene sediment: K_x = 5 m/d, K_z = 0.5 m/d; Other parameters as per Case B (Table 11)	As per Case B (Table 11)	As per Case B (Table 11)	As per Case B (Table 11)
Case 4	Holocene sediment: Layer thickness = 15 m; Other parameters as per Case B (Table 11)	As per Case B (Table 11)	As per Case B (Table 11)	As per Case B (Table 11)
Case 5	As per Case B (Table 11)	K_{sp} = 7418 m/d, K_{ep} = 70,618 m/d; Other parameters as per Case B (Table 11)	As per Case B (Table 11)	As per Case B (Table 11)
Case 6	As per Case B (Table 11)	As per Case B (Table 11)	Type: Geofabric, as per Table 10	As per Case B (Table 11)
Case 7	As per Case B (Table 11)	L_p = 200 m, K_p = 3.5 × 10^8 m/d, K_{sp} = 15,147 m/d, K_{ep} = 142,265 m/d; Other parameters as per Case B (Table 11)	As per Case B (Table 11)	As per Case B (Table 11)
Case 8	As per Case B (Table 11)	Type: 100 PN9, K_p = 2.9 × 10^8 m/d, K_{sp} = 10,902 m/d K_{ep} = 129,628 m/d; Other parameters as per Case B (Table 11)	As per Case B (Table 11)	As per Case B (Table 11)
Case 9	As per Case B (Table 11)	As per Case B (Table 11)	As per Case B (Table 11)	As per Figure 23; Other parameters as per Case B (Table 11)
Case 10	As per Case B (Table 11)	Orientation: perpendicular, W_1 = 50	As per Case B (Table 14)	As per Case B (Table 11)

Scenario	Component*			
	Aquifer	Infiltration gallery		
		Pipe	Filter	Abstraction well/sump
		m; Other parameters as per Case B (Table 11)		
Case 11	As per Case B (Table 11)	Orientation: perpendicular; W_1 = 200 m; Other parameters as per Case B (Table 11)	As per Case B (Table 11)	As per Case B (Table 11)
Case 12	As per Case B (Table 11)	Orientation: parallel and perpendicular (Figure 25), L_{p1} = 50 m, L_{p2} = 24 m; Other parameters as per Case B (Table 11)	As per Case B (Table 11)	As per Case B (Table 11)

*Gravel pack properties remain consistent with those employed in Case B (refer to Table 11) across all model scenarios.

Table B2. Details of the model discretization for each model scenario. *NCOL*, *NROW*, and *NLAY* represent the number of columns (*x*-direction), rows (*y*-direction), and layers (*z*-direction), respectively.

Scenario	*x*-direction			*y*-direction			*z*-direction			Total cells
	Min. Δx (m)	Max. Δx (m)	*NCOL* (-)	Min. Δy (m)	Max. Δy (m)	*NROW* (-)	Min. Δz (m)	Max. Δz (m)	*NLAY* (-)	
Case 1	0.5	5	114	0.15	9	85	3×10^{-3}	20	24	232,560
Case 2	0.5	5	114	0.15	9	85	3×10^{-3}	20	24	232,560
Case 3	0.5	5	114	0.15	9	85	3×10^{-3}	20	24	232,560
Case 4	0.5	5	114	0.15	9	85	3×10^{-3}	15	27	261,630
Case 5	0.5	5	114	0.15	9	85	3×10^{-3}	20	24	232,560
Case 6	0.5	5	114	0.15	9	85	3×10^{-3}	20	24	232,560
Case 7	0.5	5	214	0.15	9	85	3×10^{-3}	20	24	436,560
Case 8	0.5	5	114	0.11	9	85	3×10^{-3}	20	24	232,560
Case 9	1.0	5	114	0.15	9	85	3×10^{-3}	20	24	232,560
Case 10	0.5	5	114	0.15	9	85	3×10^{-3}	20	24	232,560
Case 11	0.5	7	146	0.15	9	85	3×10^{-3}	20	24	297,840
Case 12	0.15	5	119	0.15	9	85	3×10^{-3}	20	24	242,760

Appendix C – Concentration distribution for Cases B to 12

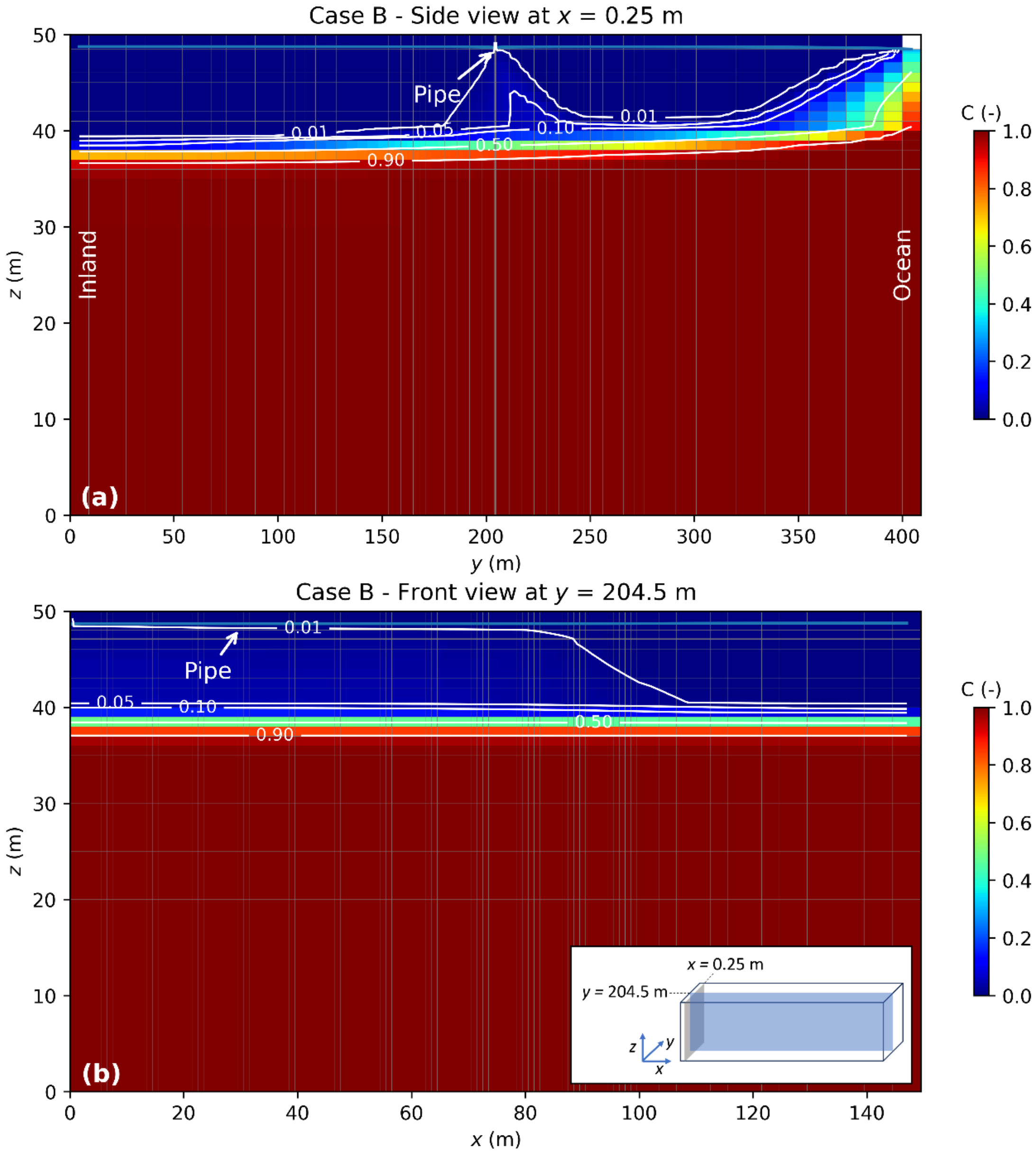

Figure C1. Relative solute concentration (C = 0 for freshwater and C = 1 for seawater) for Case B. White lines show the isochlor contours, while the blue line indicates the water table.

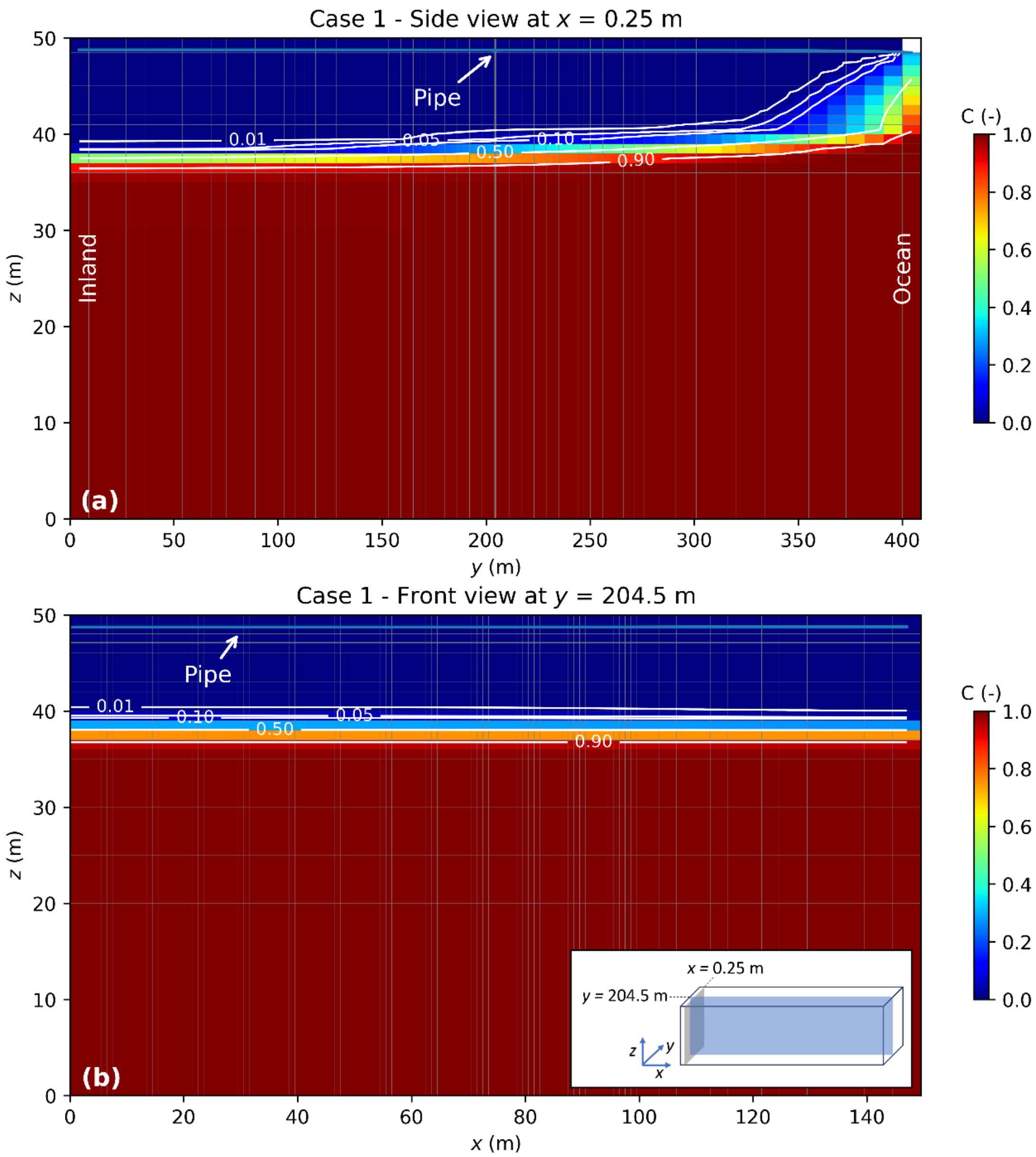

Figure C2. Relative solute concentration (C = 0 for freshwater and C = 1 for seawater) for Case 1. White lines show the isochlor contours, while the blue line indicates the water table.

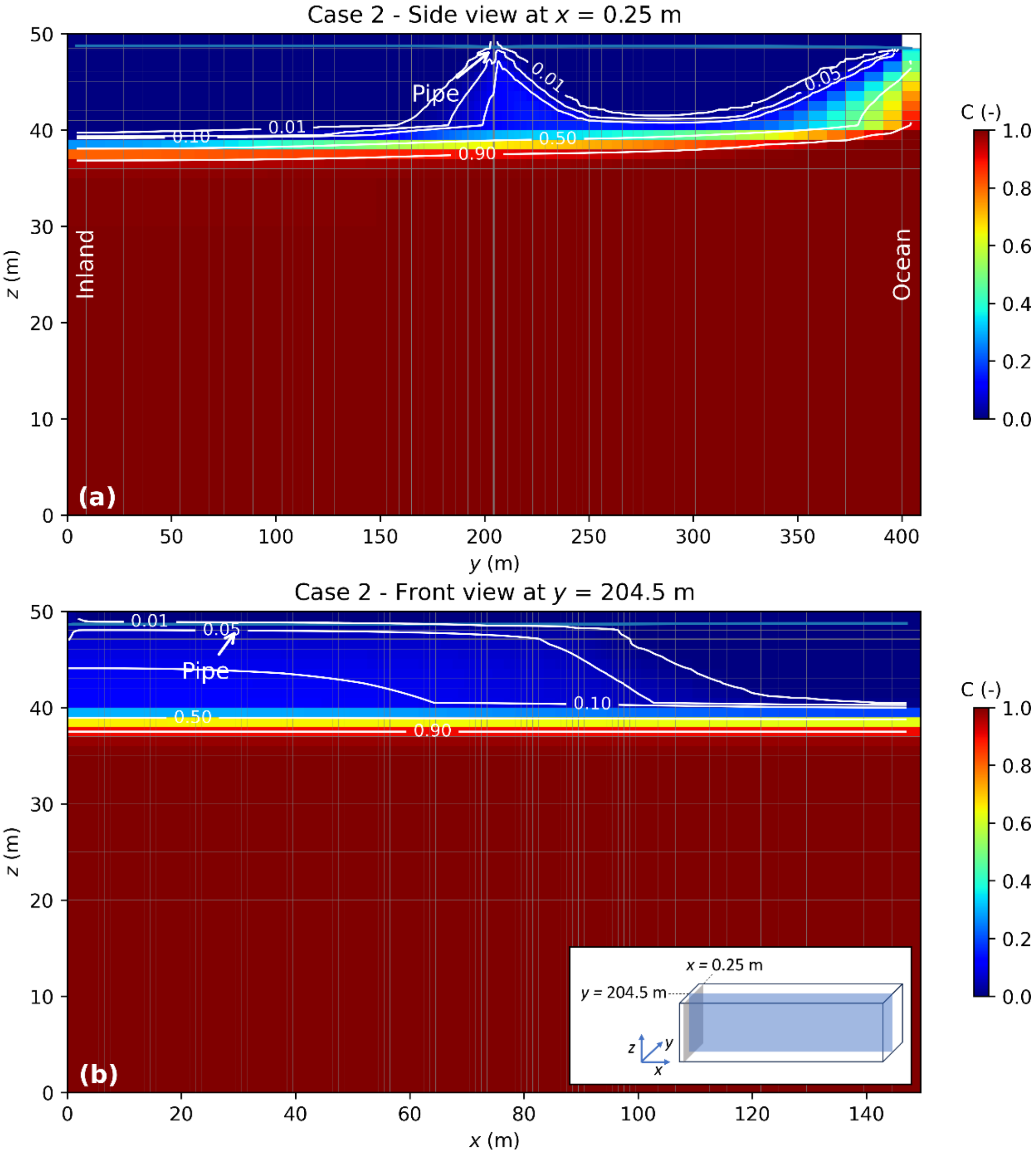

Figure C3. Relative solute concentration (C = 0 for freshwater and C = 1 for seawater) for Case 2. White lines show the isochlor contours, while the blue line indicates the water table.

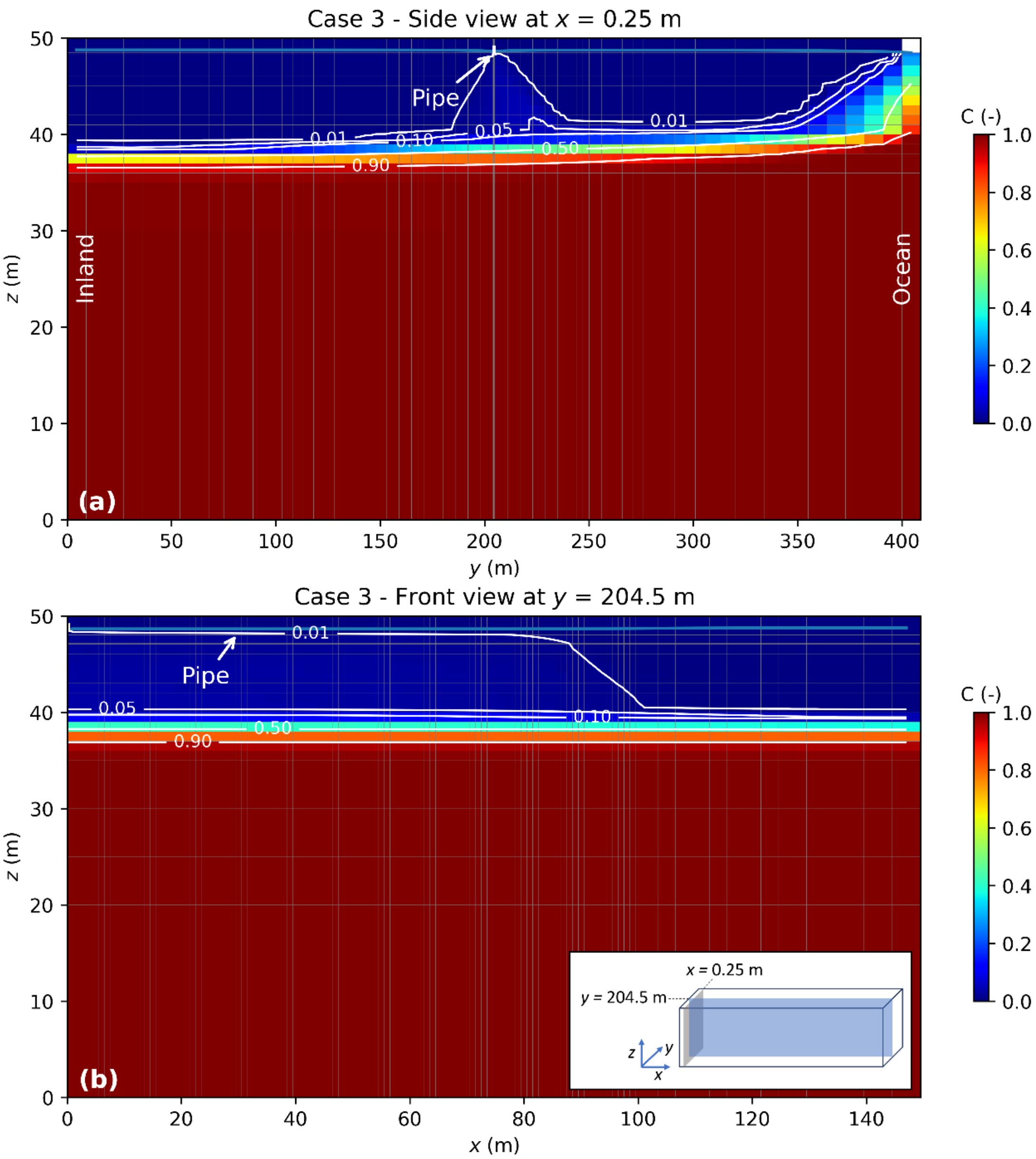

Figure C4. Relative solute concentration (C = 0 for freshwater and C = 1 for seawater) for Case 3. White lines show the isochlor contours, while the blue line indicates the water table.

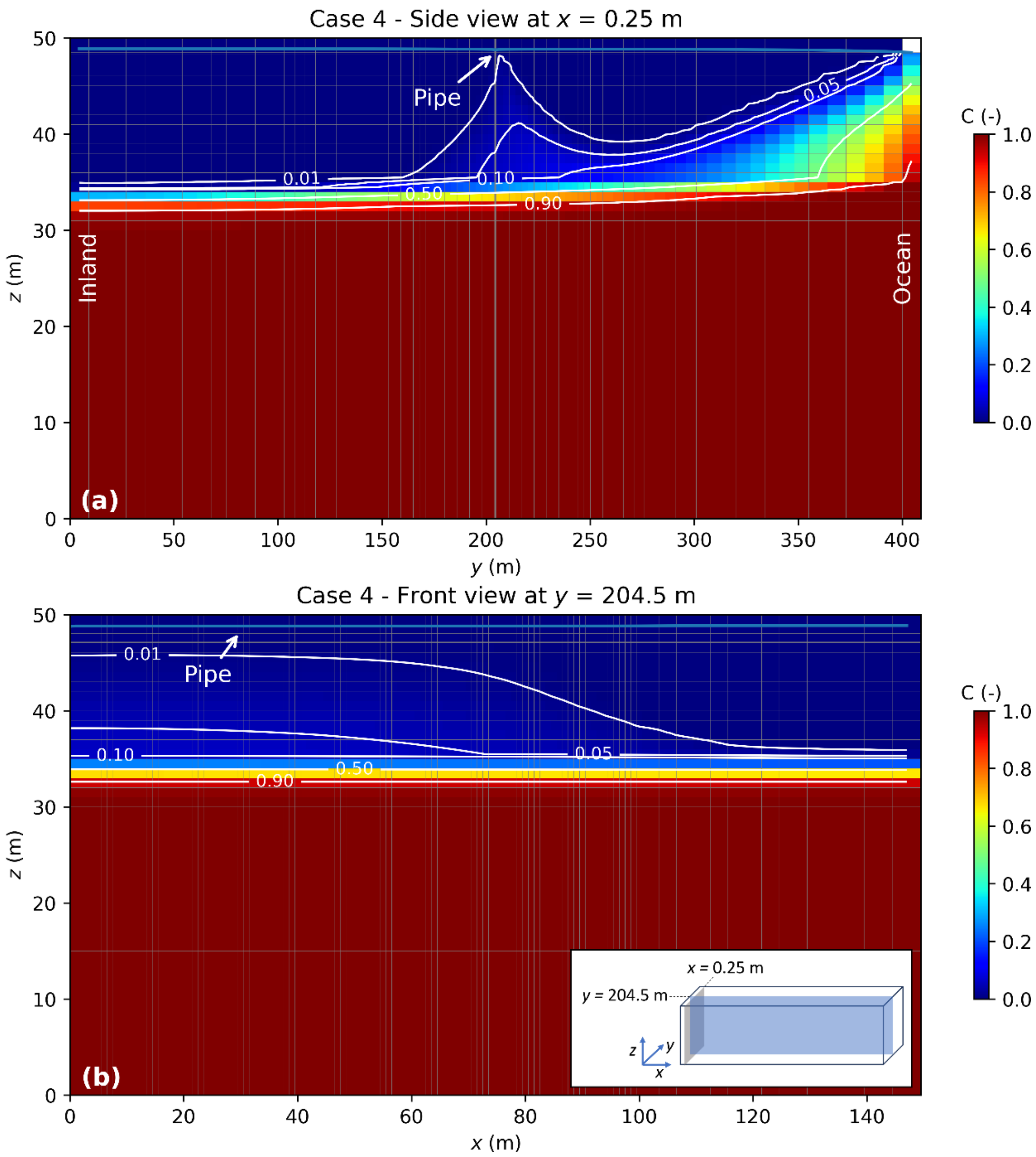

Figure C5. Relative solute concentration (C = 0 for freshwater and C = 1 for seawater) for Case 4. White lines show the isochlor contours, while the blue line indicates the water table.

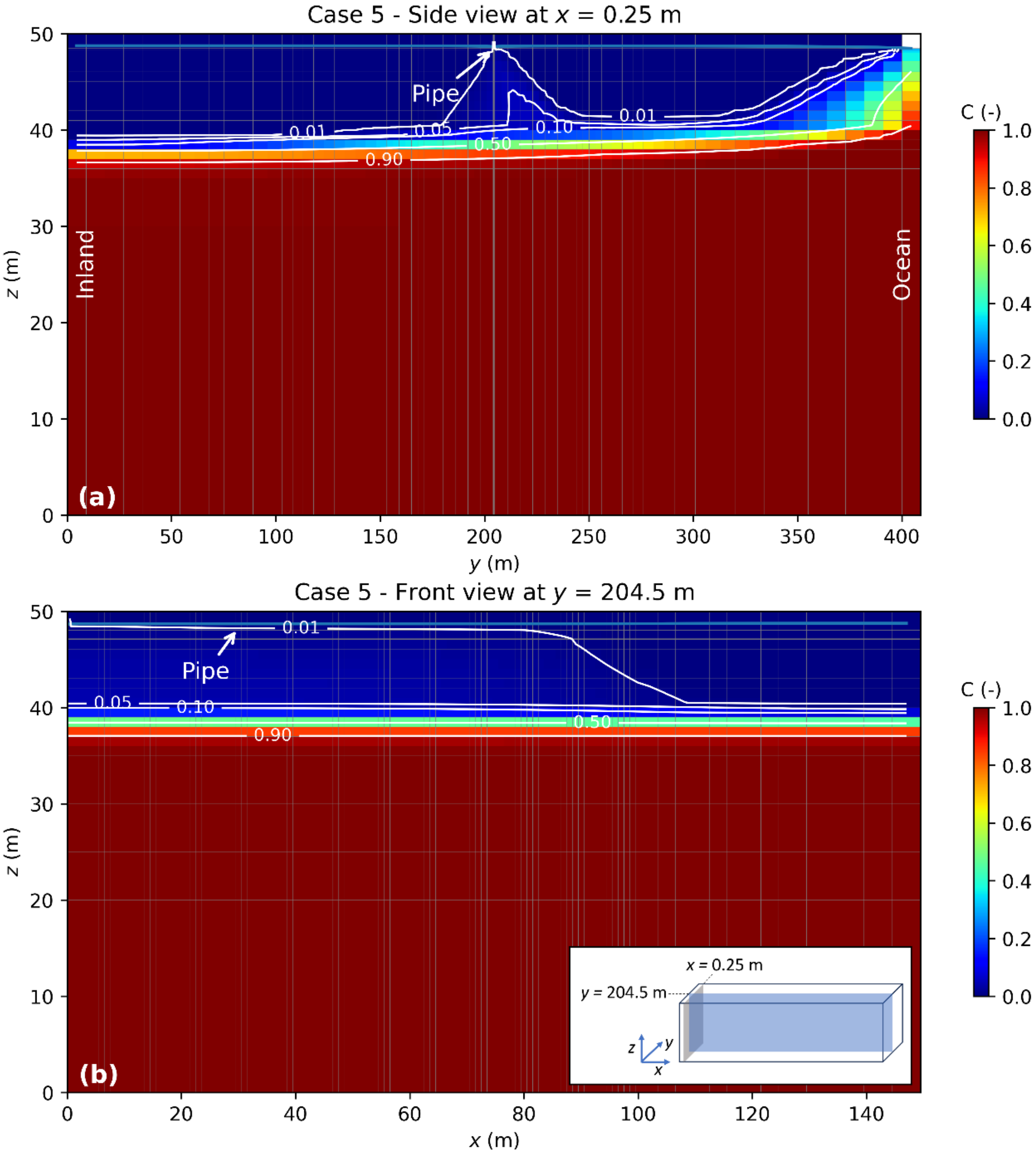

Figure C6. Relative solute concentration (C = 0 for freshwater and C = 1 for seawater) for Case 5. White lines show the isochlor contours, while the blue line indicates the water table.

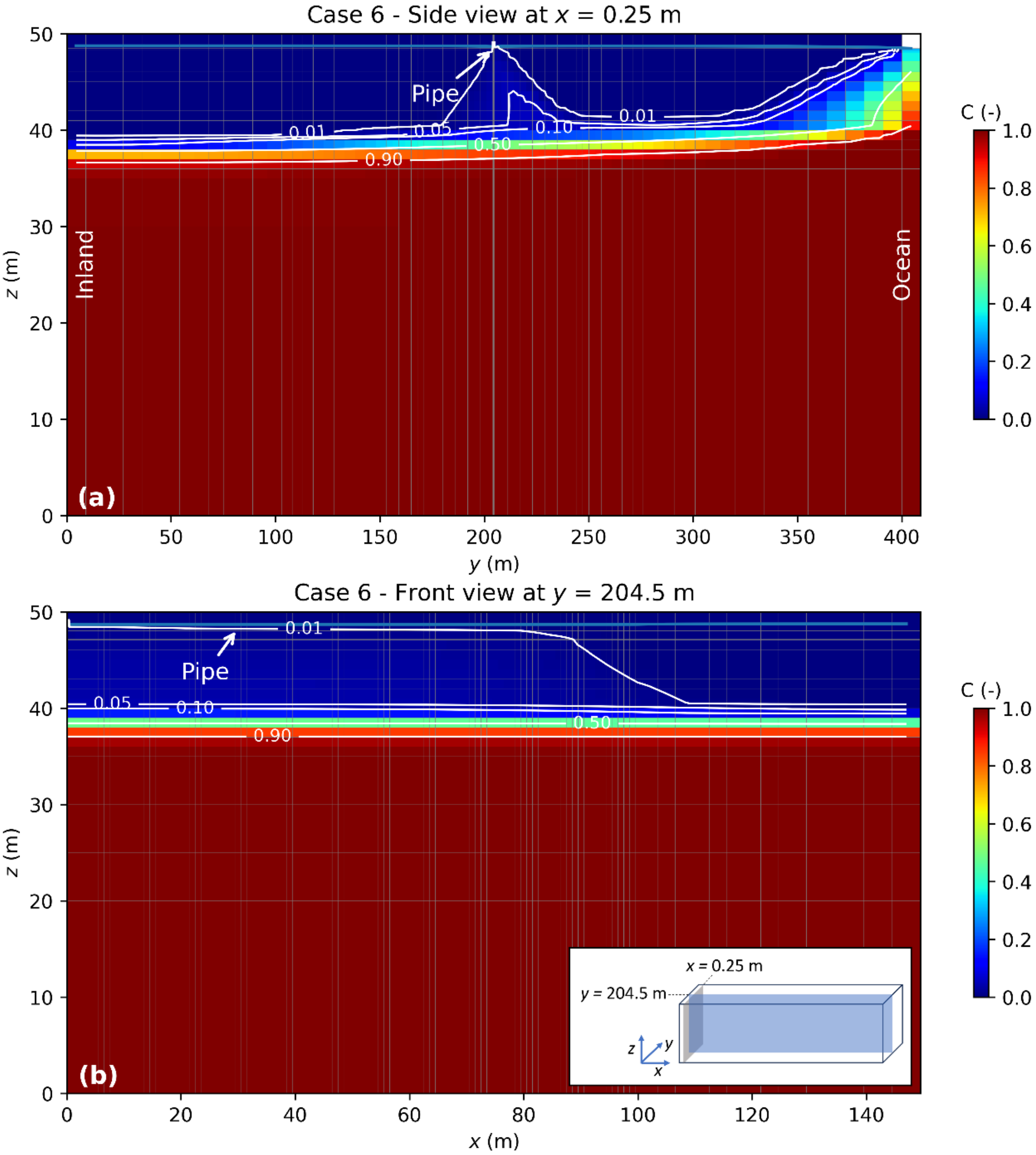

Figure C7. Relative solute concentration (C = 0 for freshwater and C = 1 for seawater) for Case 6. White lines show the isochlor contours, while the blue line indicates the water table.

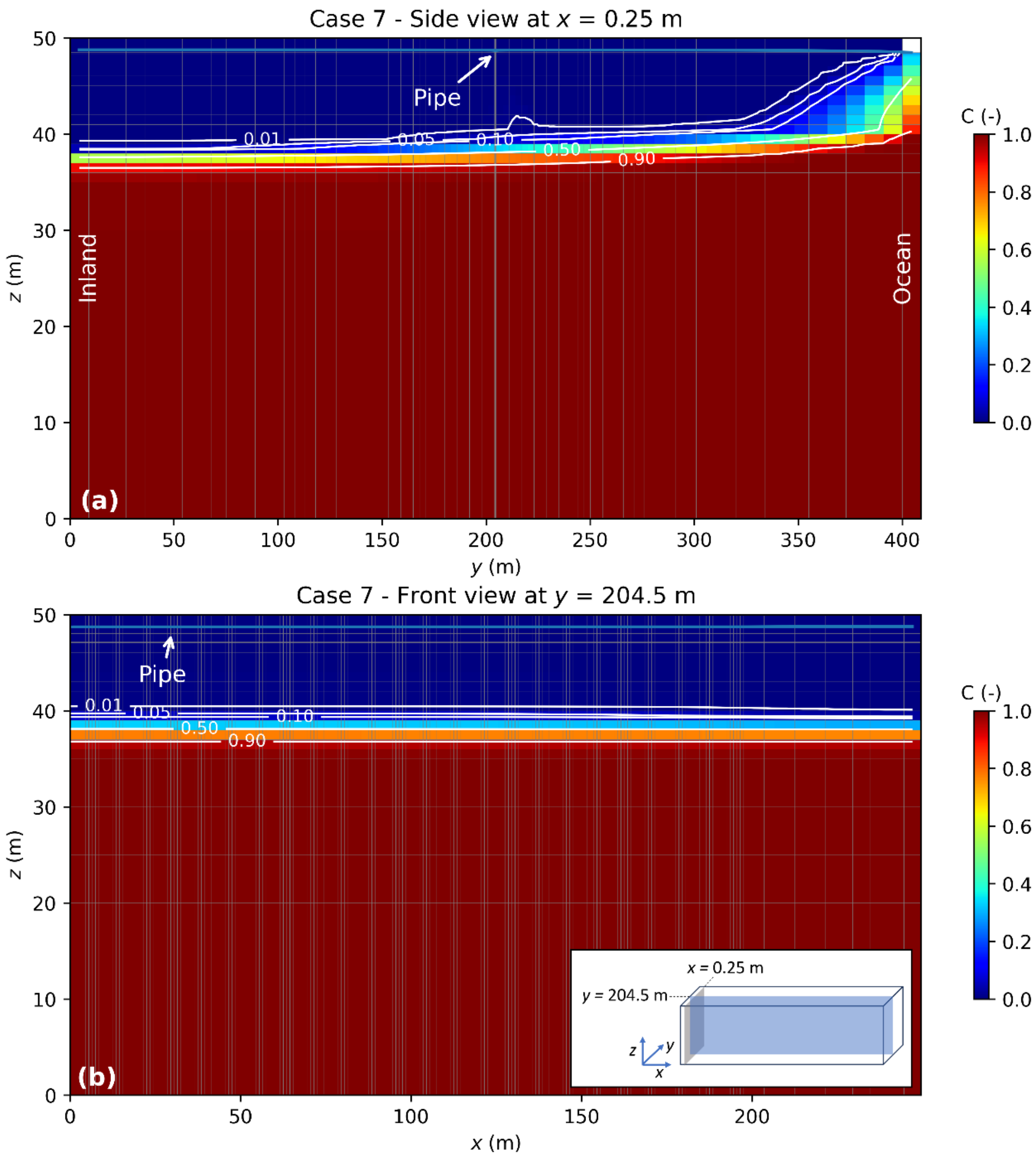

Figure C8. Relative solute concentration (C = 0 for freshwater and C = 1 for seawater) for Case 7. White lines show the isochlor contours, while the blue line indicates the water table.

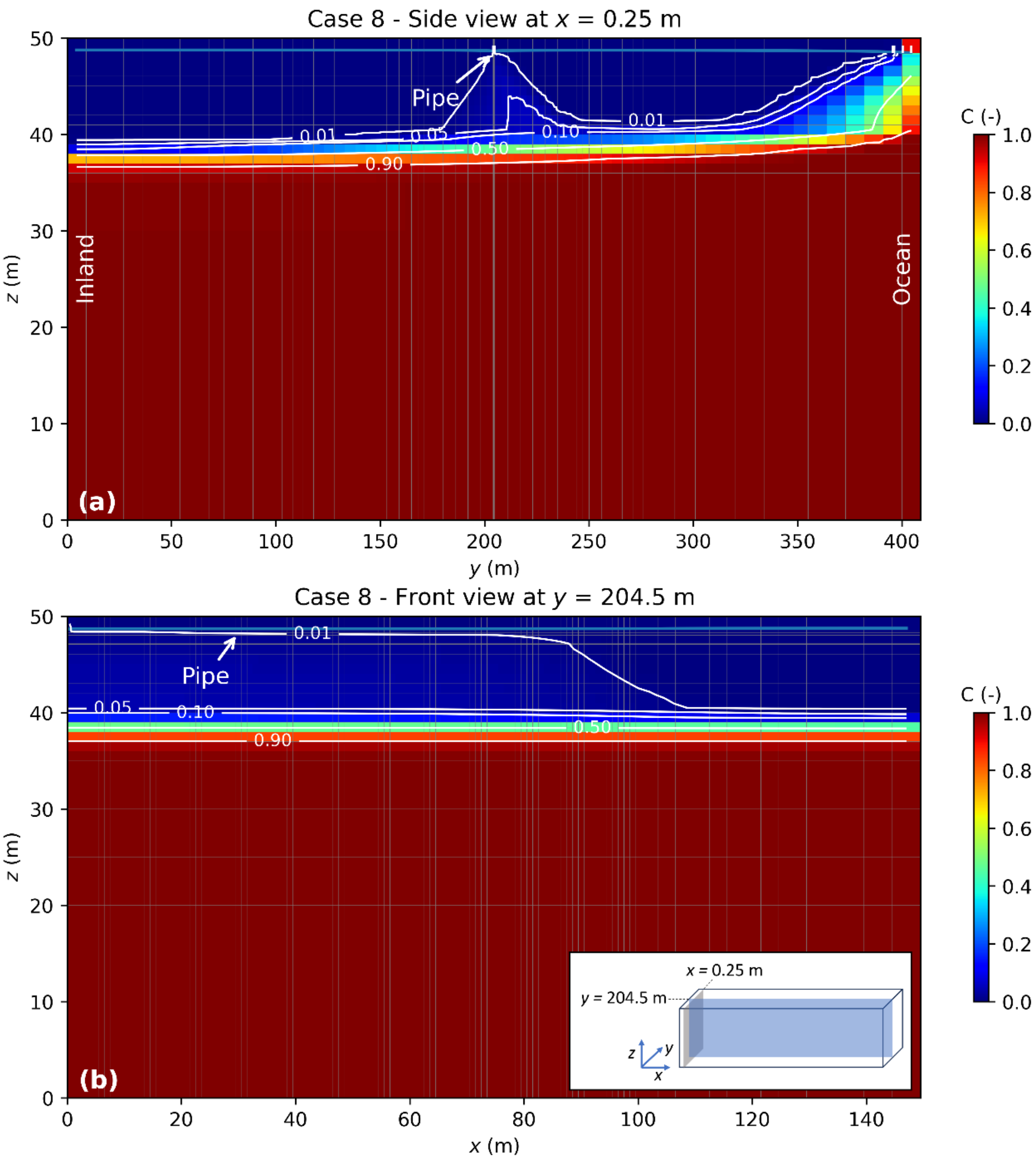

Figure C9. Relative solute concentration (C = 0 for freshwater and C = 1 for seawater) for Case 8. White lines show the isochlor contours, while the blue line indicates the water table.

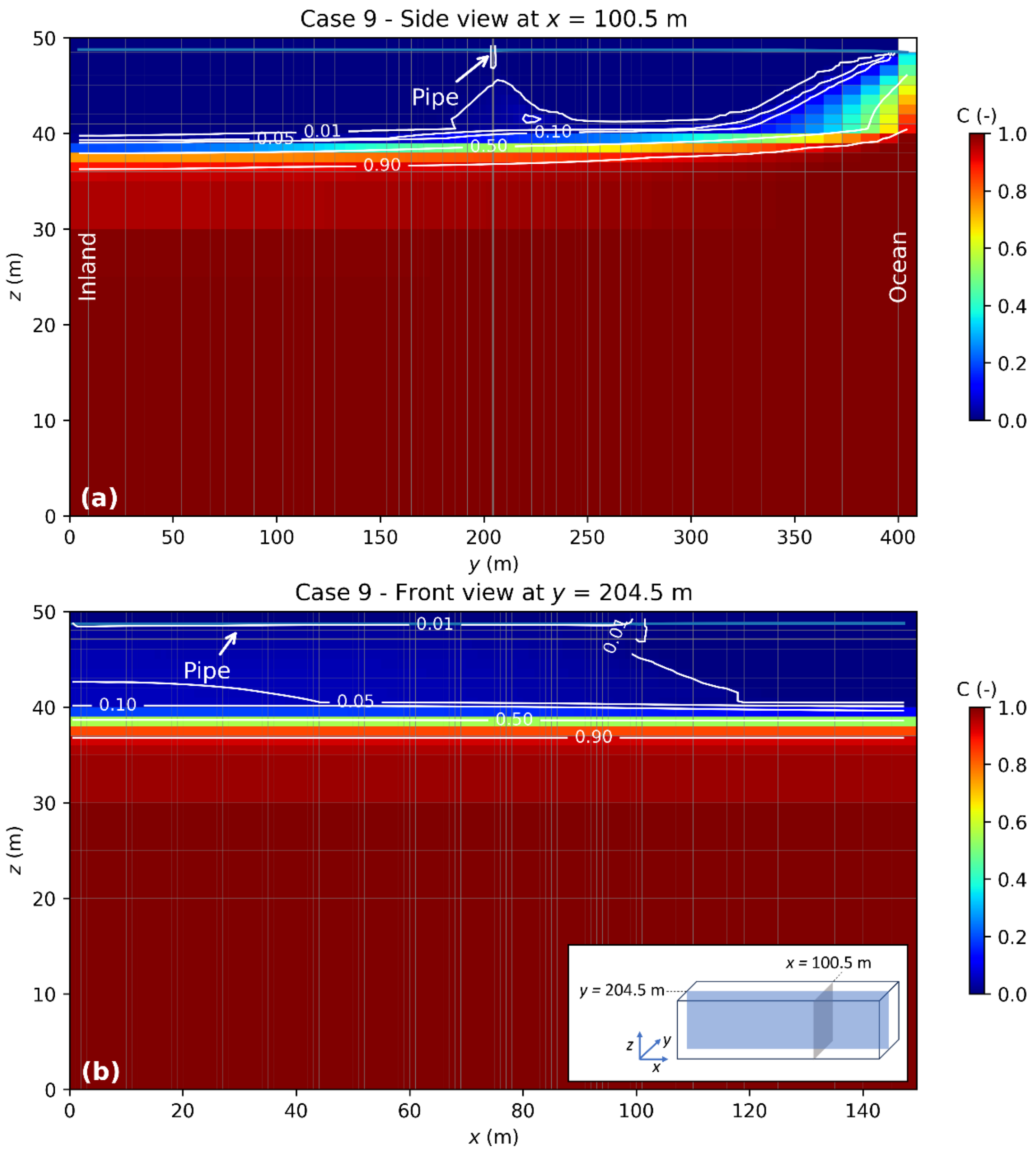

Figure C10. Relative solute concentration (C = 0 for freshwater and C = 1 for seawater) for Case 9. White lines show the isochlor contours, while the blue line indicates the water table.

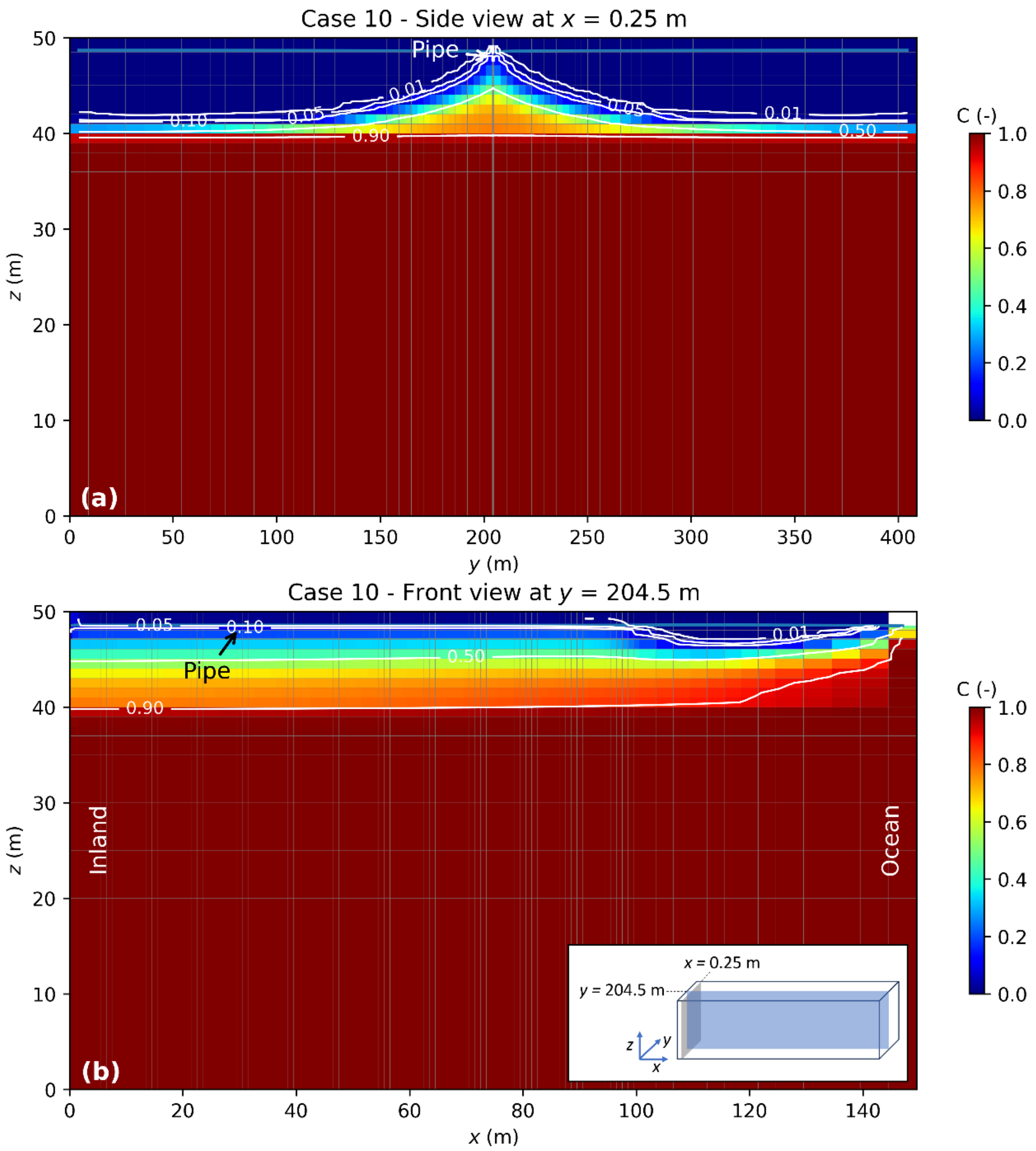

Figure C11. Relative solute concentration ($C = 0$ for freshwater and $C = 1$ for seawater) for Case 10. White lines show the isochlor contours, while the blue line indicates the water table.

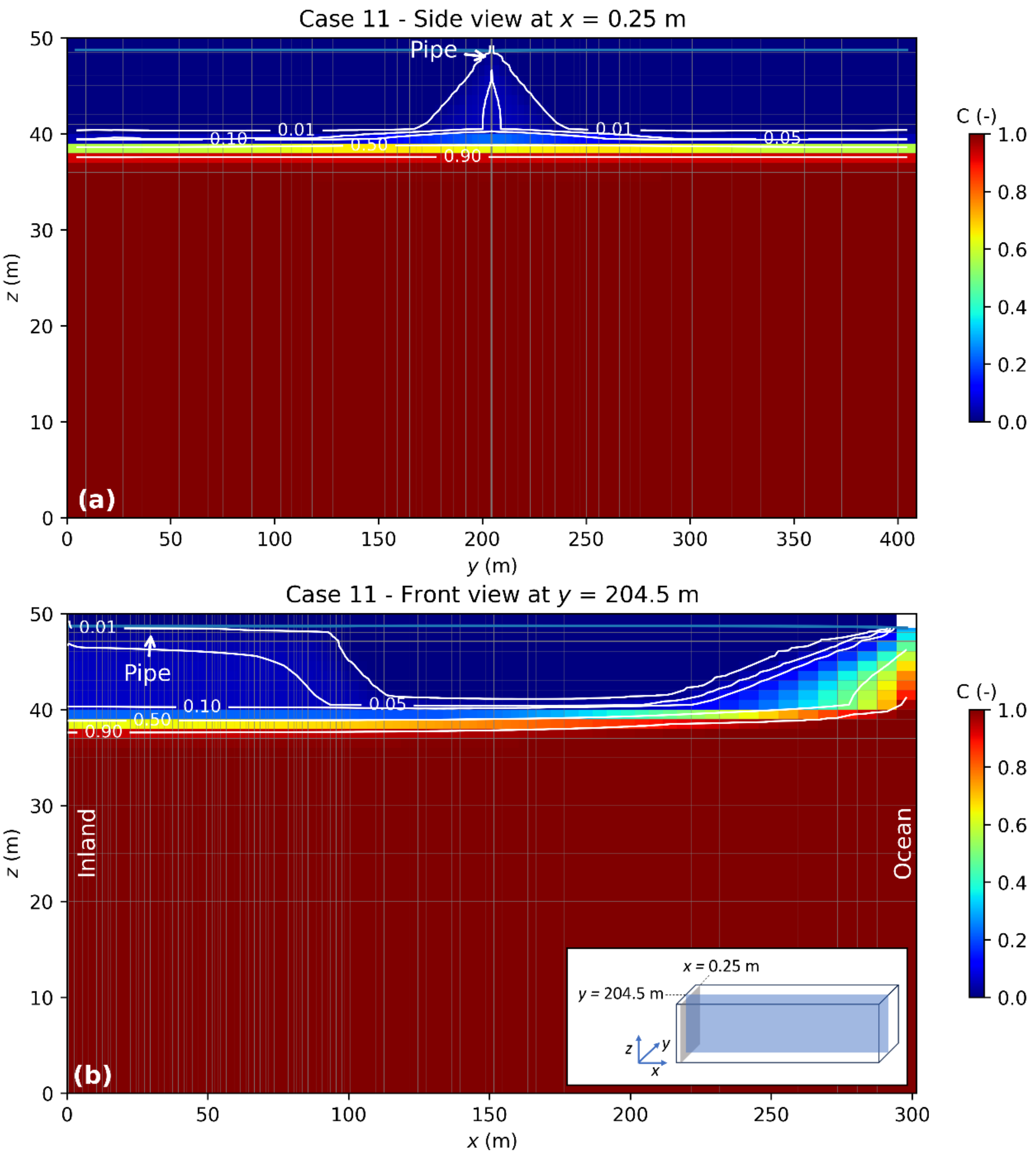

Figure C12. Relative solute concentration (C = 0 for freshwater and C = 1 for seawater) for Case 11. White lines show the isochlor contours, while the blue line indicates the water table.

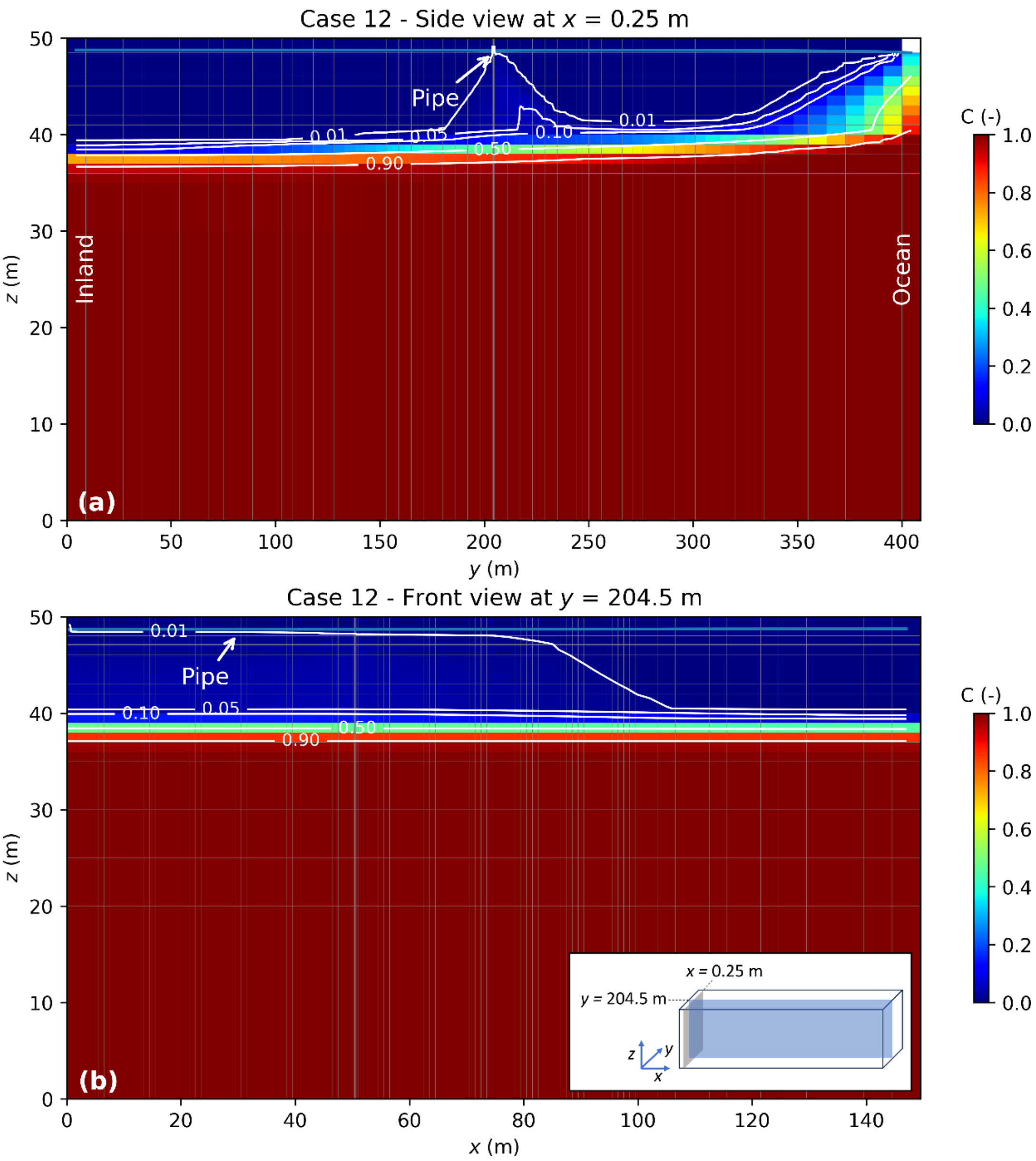

Figure C13. Relative solute concentration (C = 0 for freshwater and C = 1 for seawater) for Case 12. White lines show the isochlor contours, while the blue line indicates the water table.

Appendix D – Head distribution for Cases B to 12

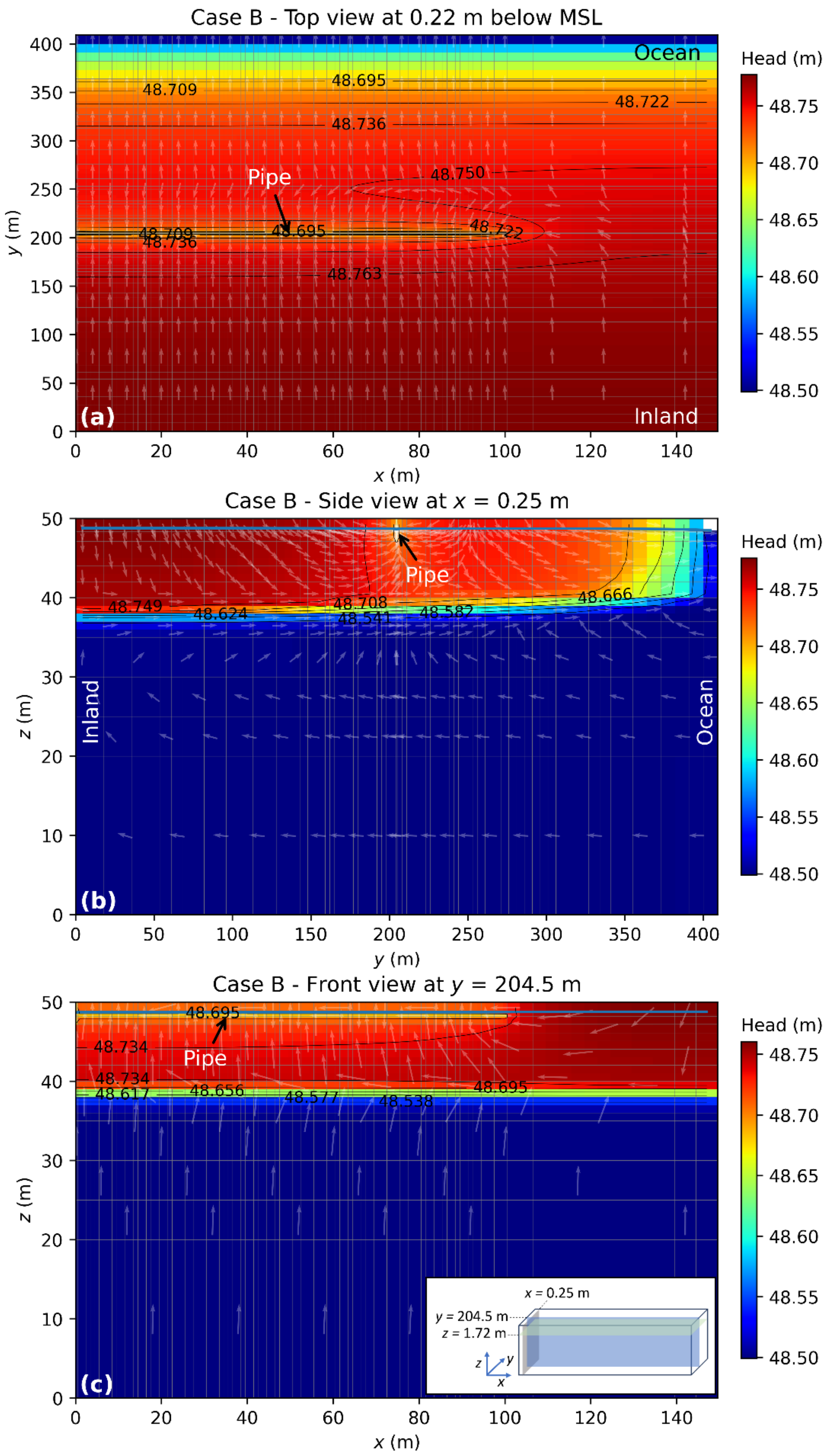

Figure D1. Head distribution for Case B. Black lines show the head contours, while the blue line indicates the water table. White arrows depict flow vectors (only a portion of vectors is shown).

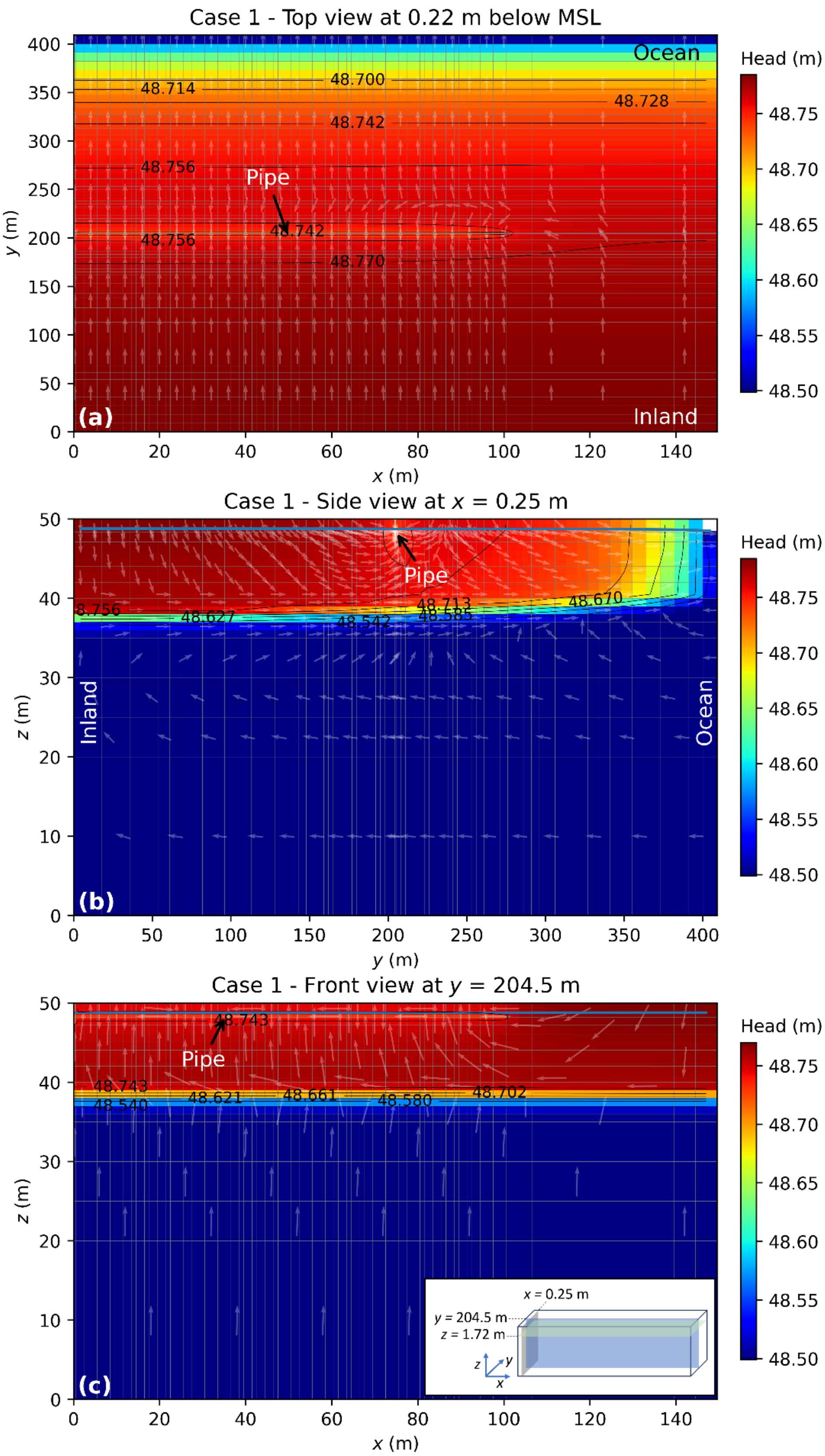

Figure D2. Head distribution for Case 1. Black lines show the head contours, while the blue line indicates the water table. White arrows depict flow vectors (only a portion of vectors is shown).

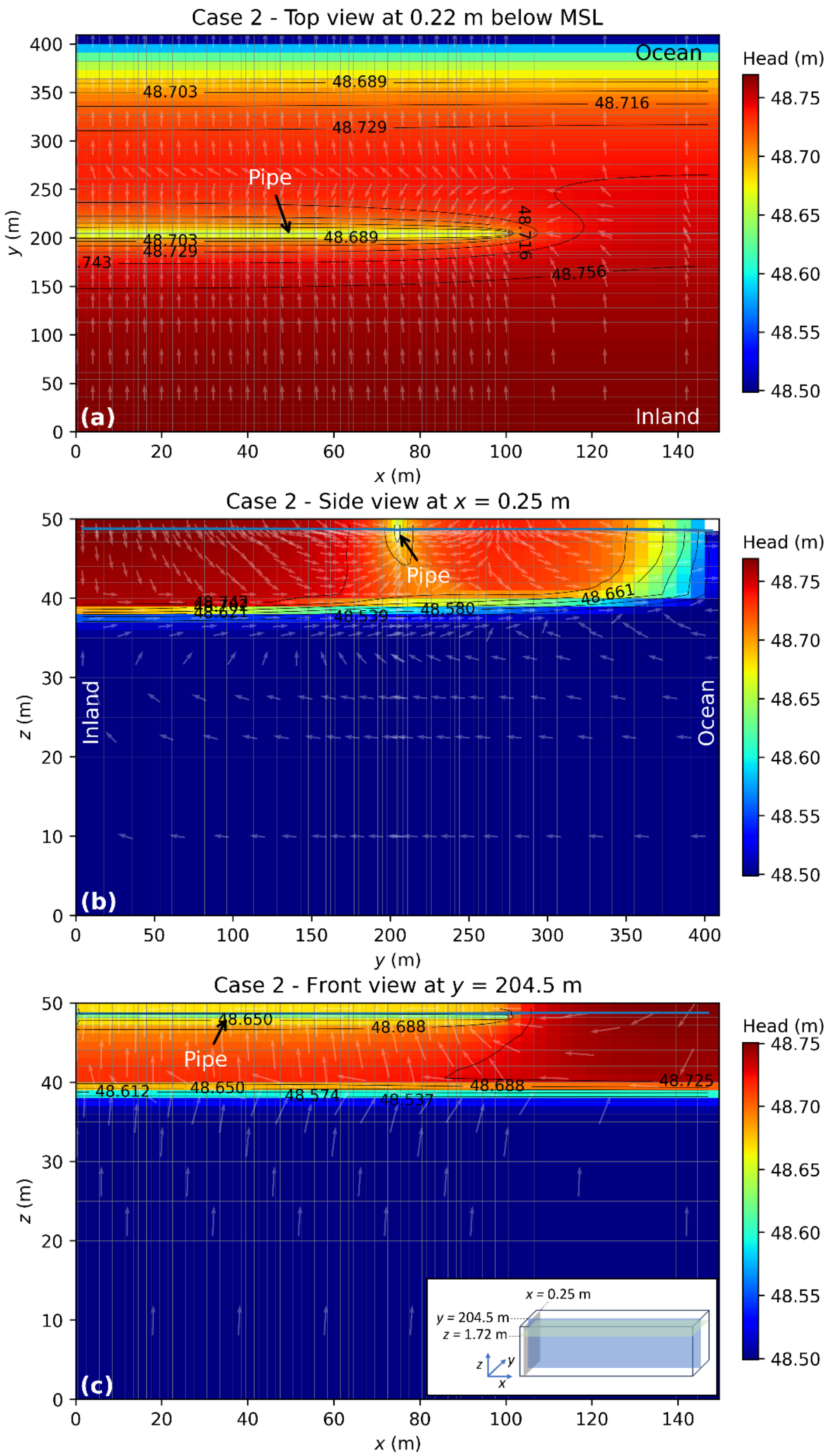

Figure D3. Head distribution for Case 2. Black lines show the head contours, while the blue line indicates the water table. White arrows depict flow vectors (only a portion of vectors is shown).

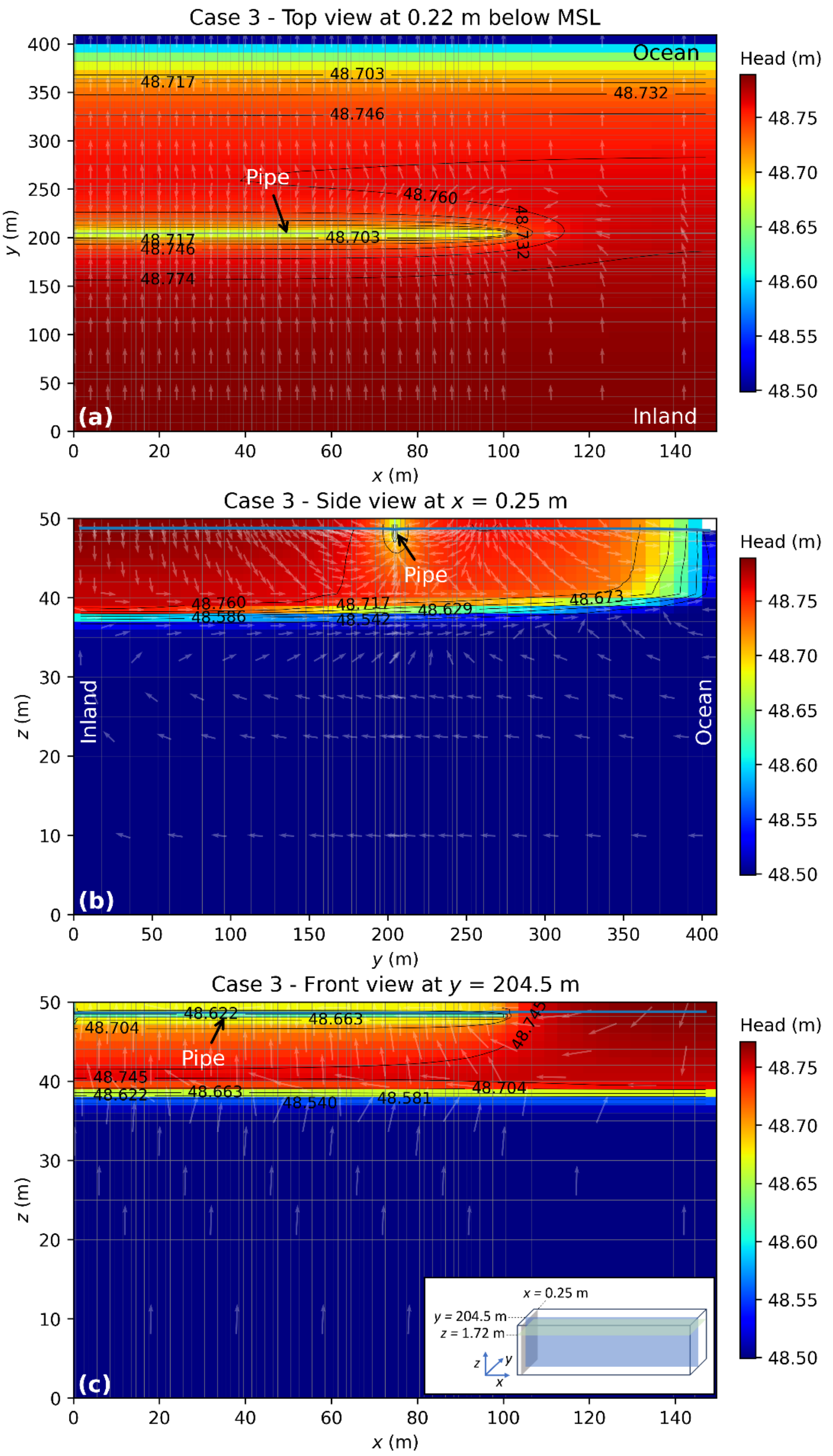

Figure D4. Head distribution for Case 3. Black lines show the head contours, while the blue line indicates the water table. White arrows depict flow vectors (only a portion of vectors is shown).

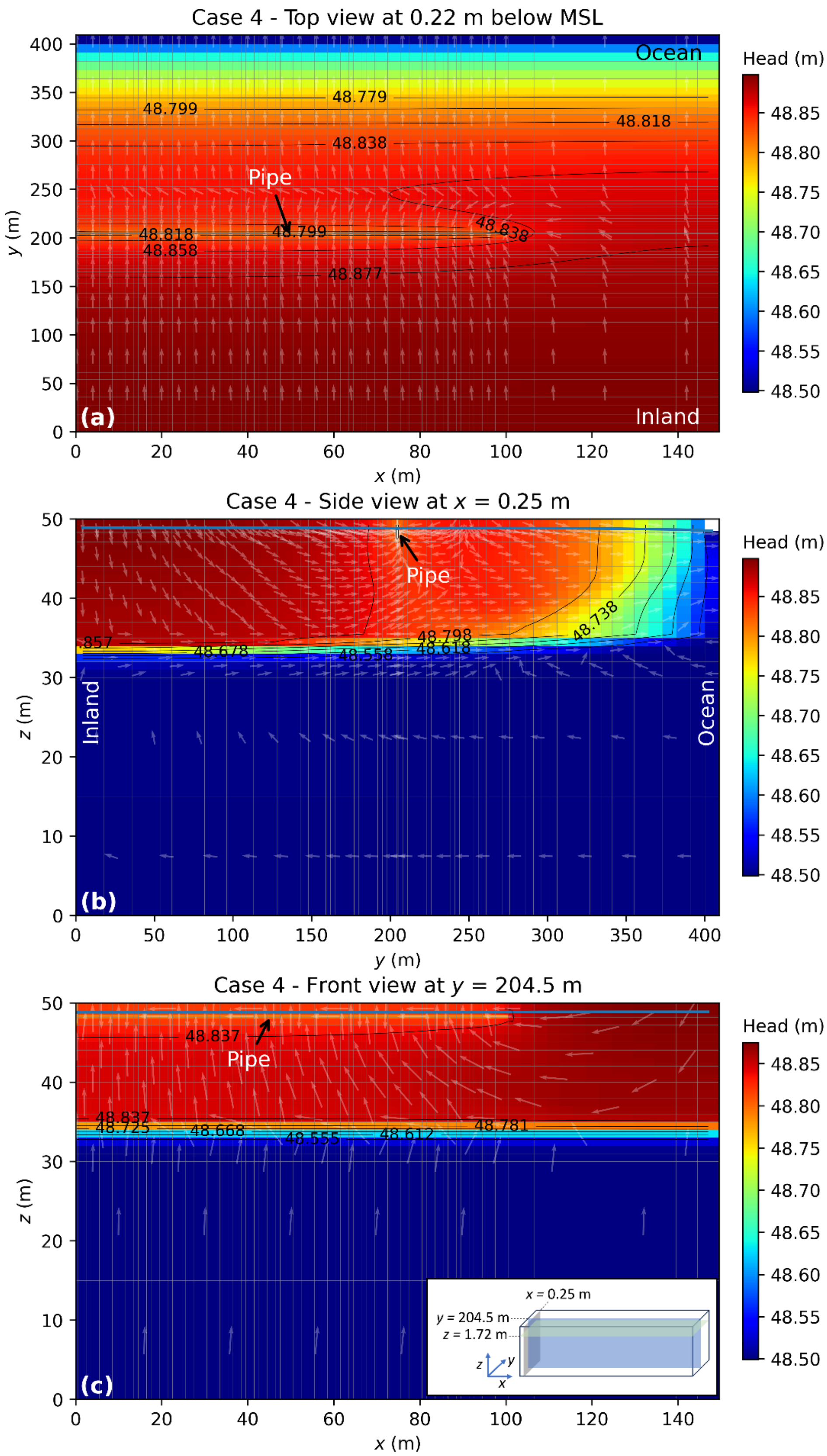

Figure D5. Head distribution for Case 4. Black lines show the head contours, while the blue line indicates the water table. White arrows depict flow vectors (only a portion of vectors is shown).

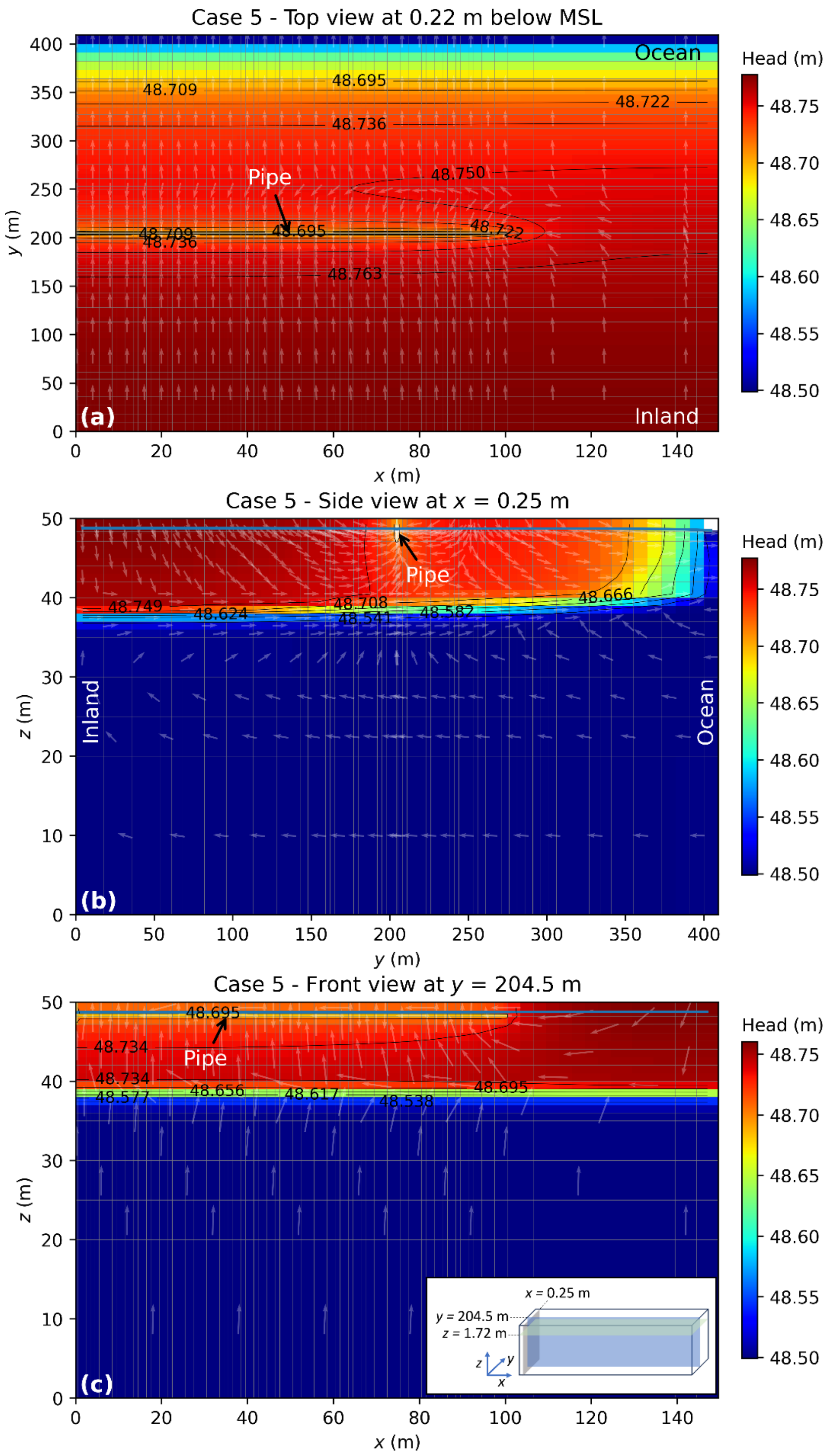

Figure D6. Head distribution for Case 5. Black lines show the head contours, while the blue line indicates the water table. White arrows depict flow vectors (only a portion of vectors is shown).

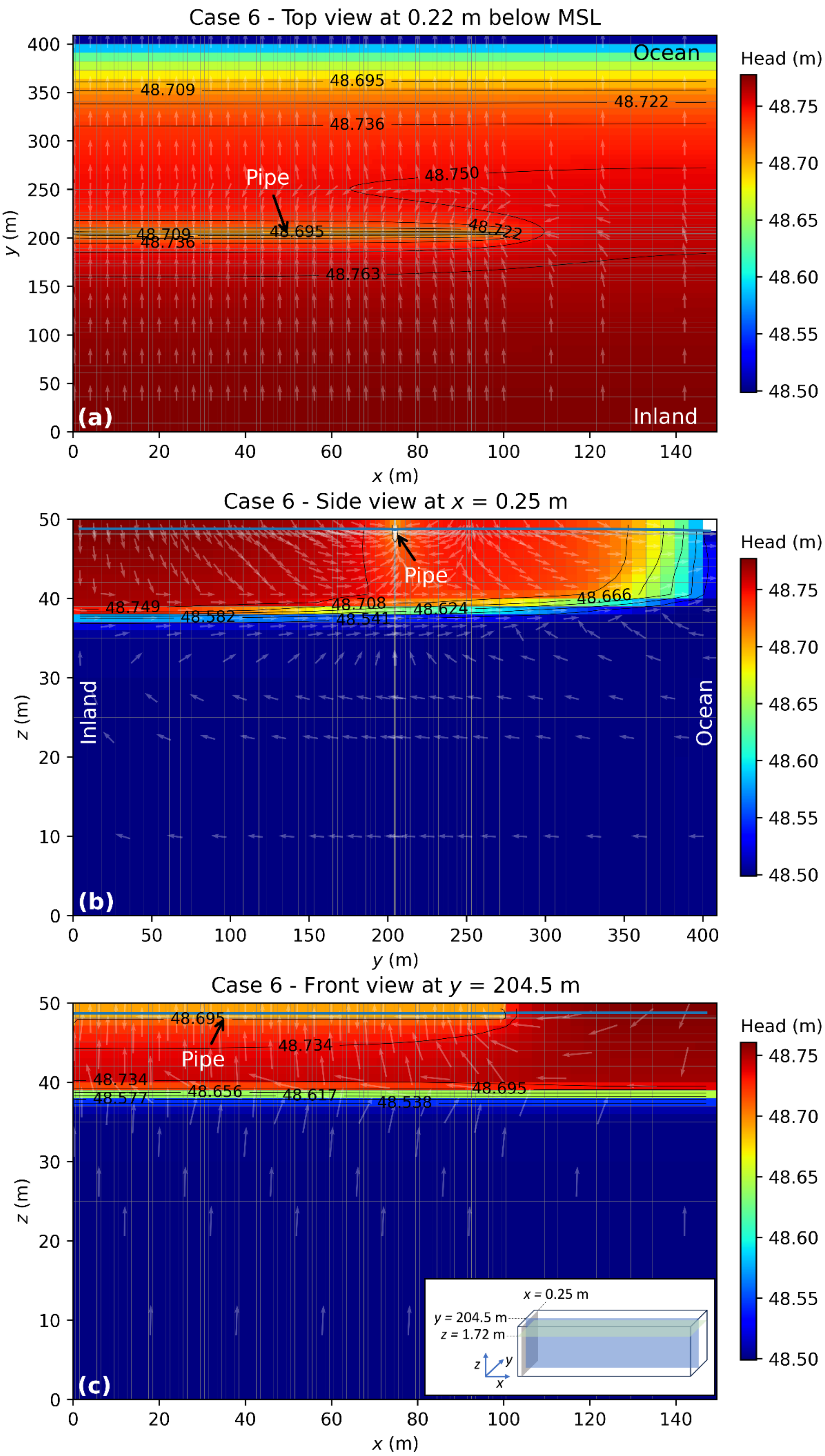

Figure D7. Head distribution for Case 6. Black lines show the head contours, while the blue line indicates the water table. White arrows depict flow vectors (only a portion of vectors is shown).

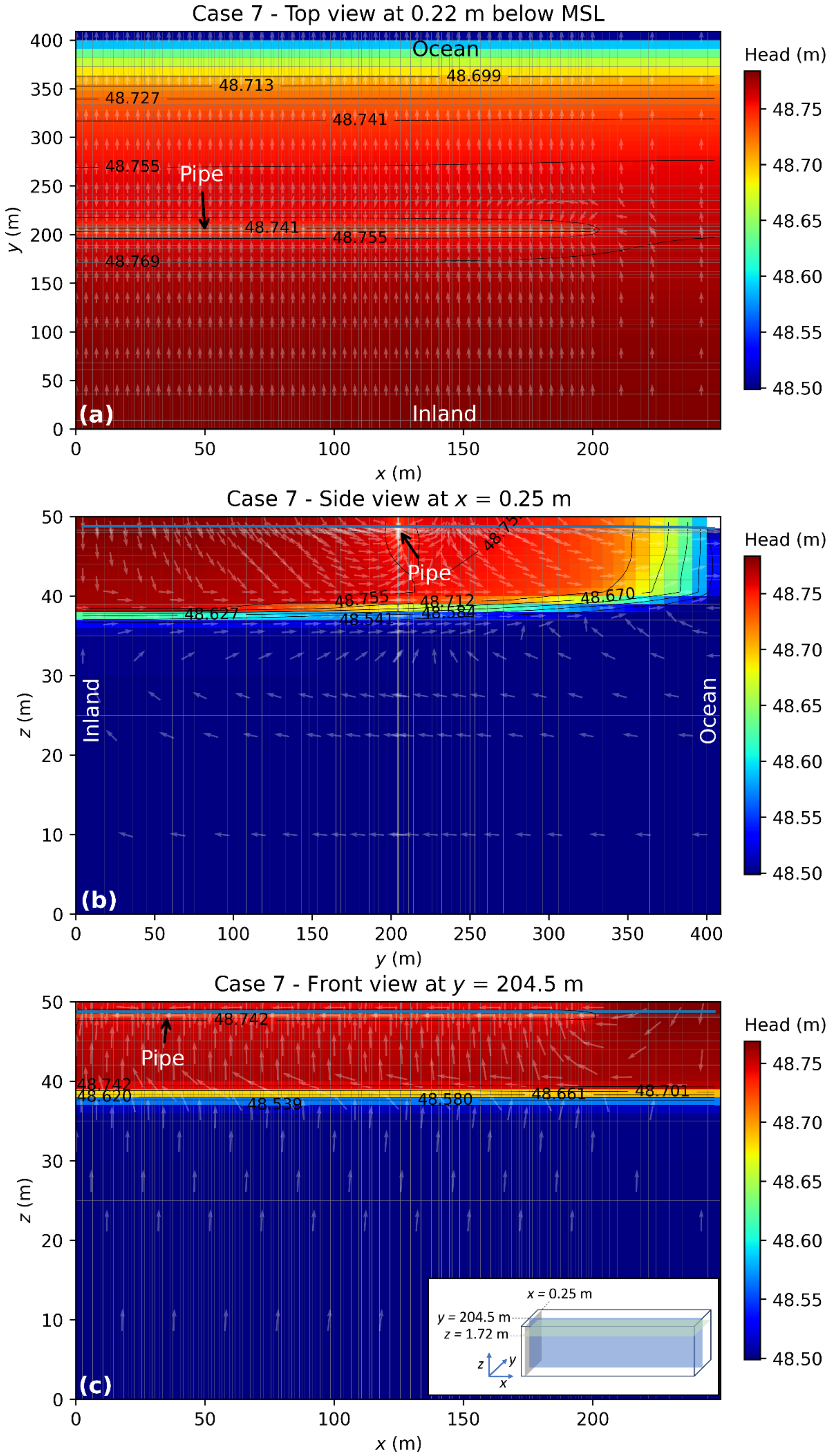

Figure D8. Head distribution for Case 7. Black lines show the head contours, while the blue line indicates the water table. White arrows depict flow vectors (only a portion of vectors is shown).

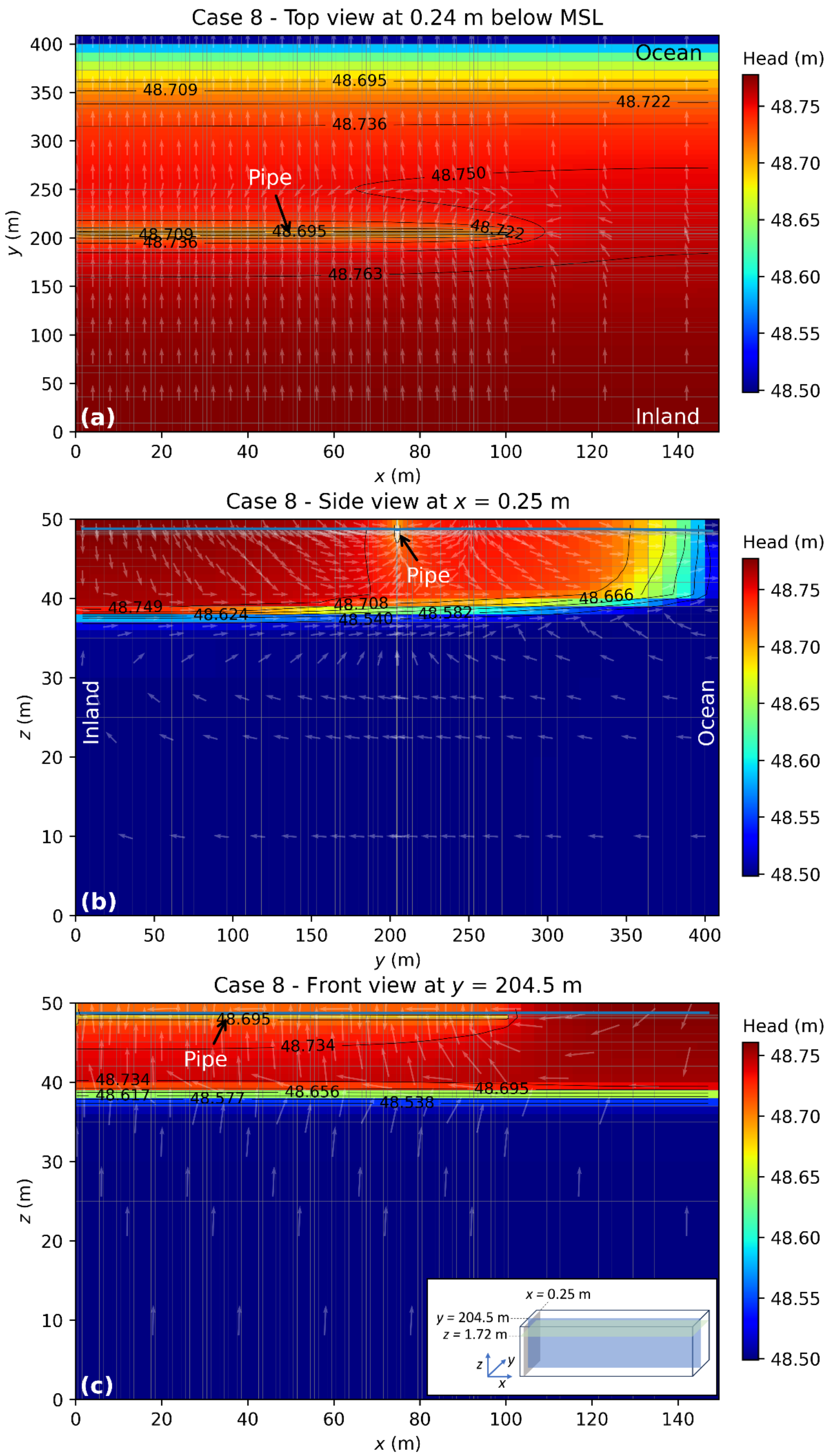

Figure D9. Head distribution for Case 8. Black lines show the head contours, while the blue line indicates the water table. White arrows depict flow vectors (only a portion of vectors is shown).

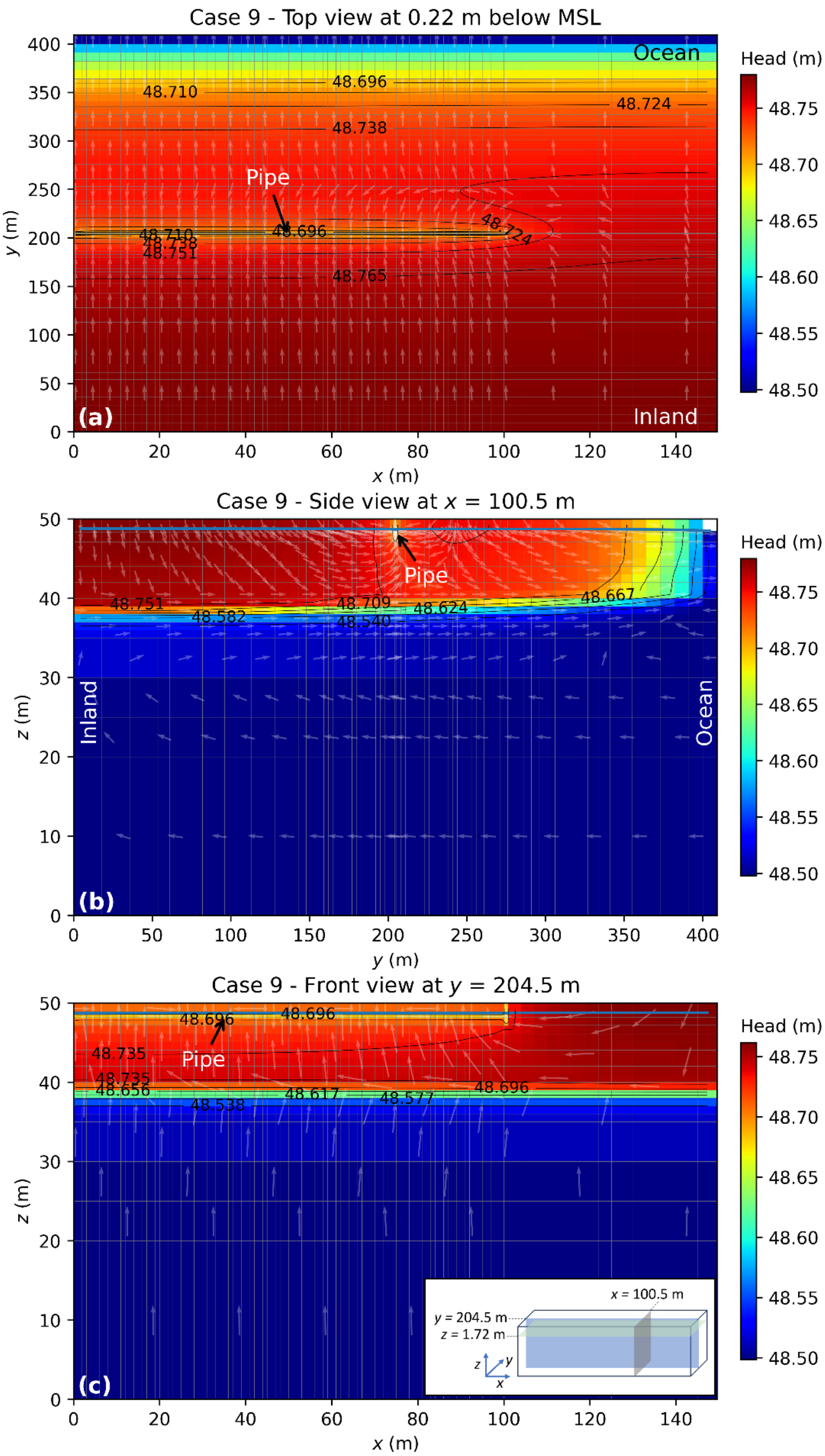

Figure D10. Head distribution for Case 9. Black lines show the head contours, while the blue line indicates the water table. White arrows depict flow vectors (only a portion of vectors is shown).

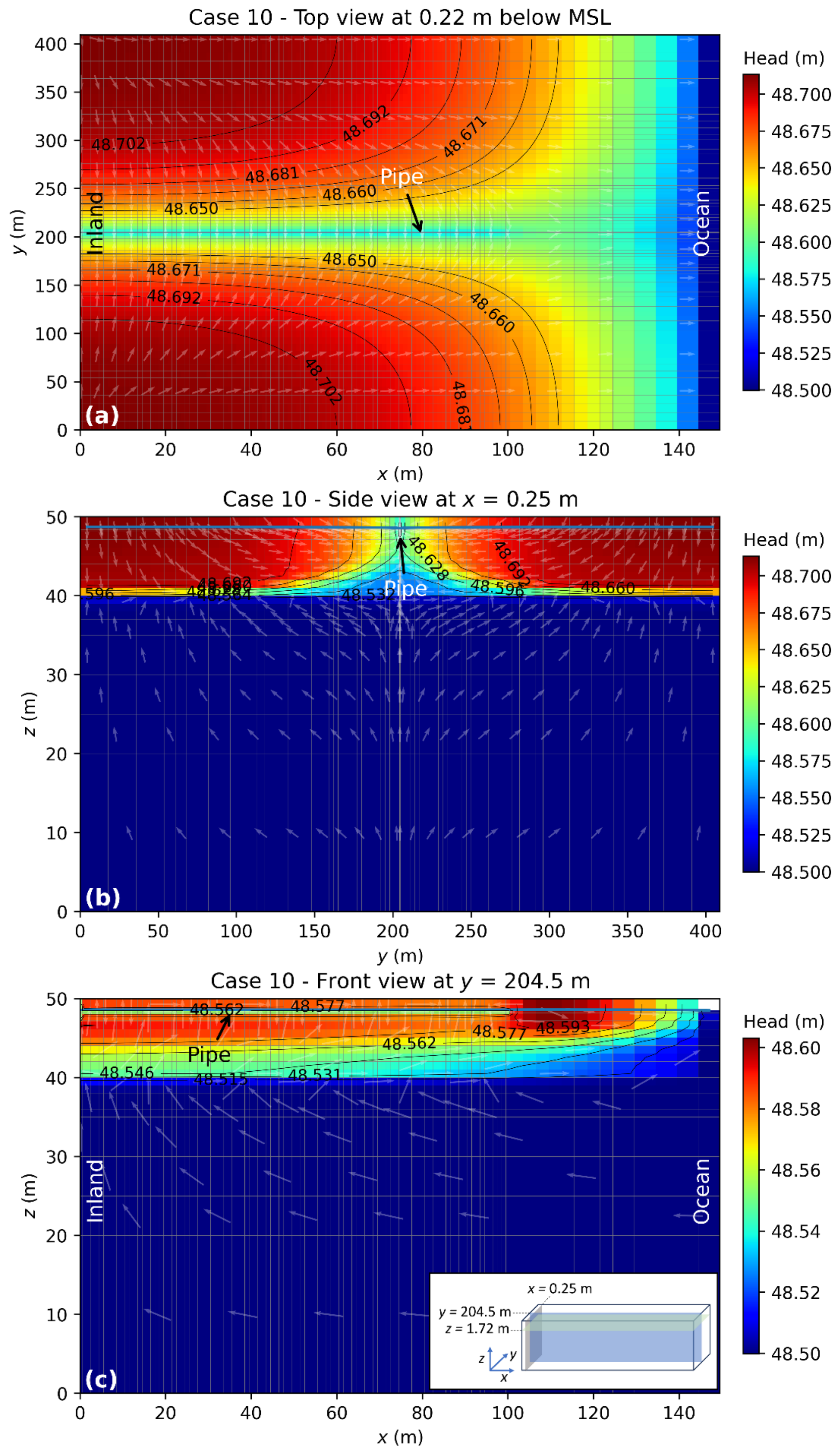

Figure D11. Head distribution for Case 10. Black lines show the head contours, while the blue line indicates the water table. White arrows depict flow vectors (only a portion of vectors is shown).

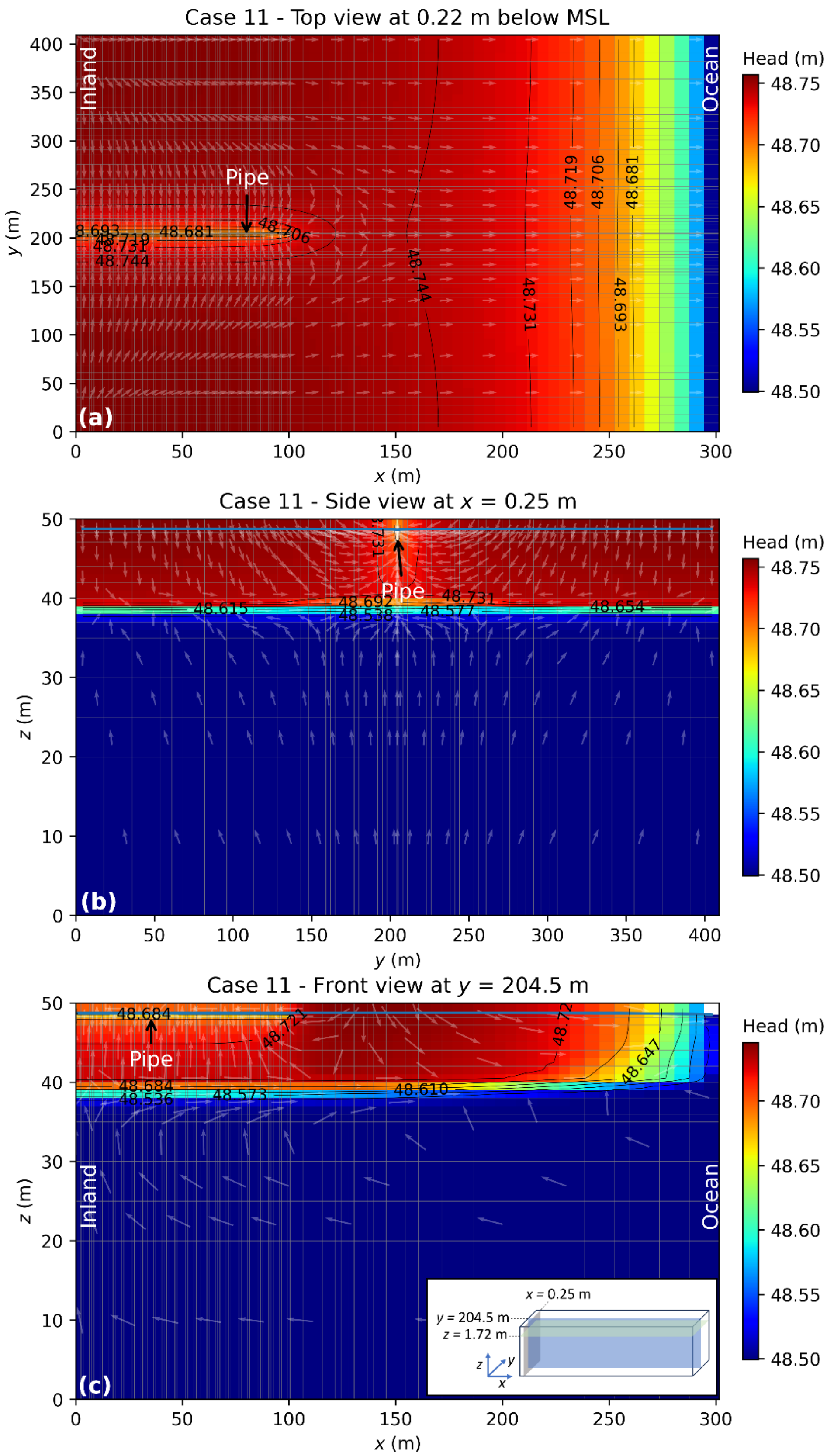

Figure D12. Head distribution for Case 11. Black lines show the head contours, while the blue line indicates the water table. White arrows depict flow vectors (only a portion of vectors is shown).

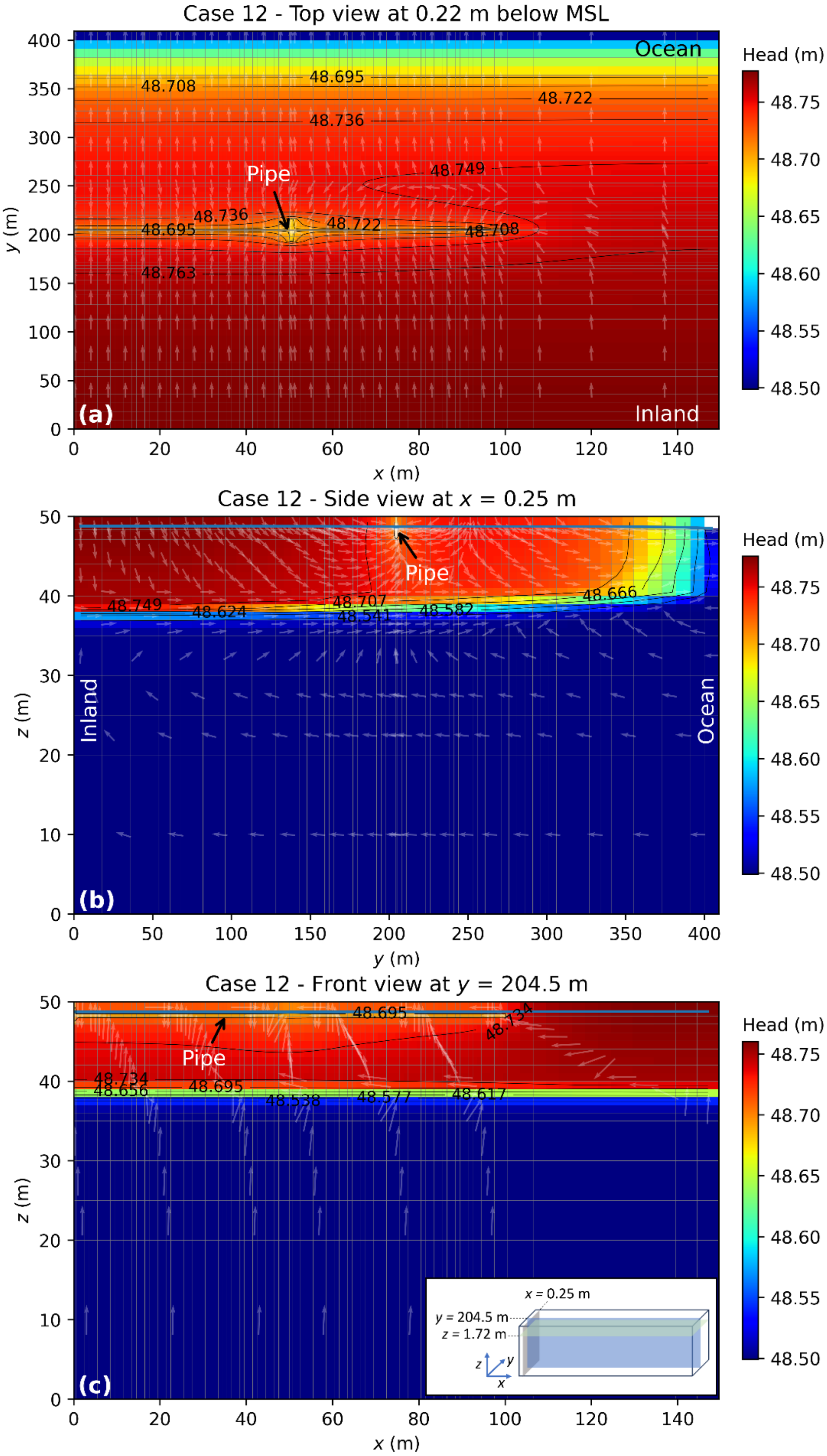

Figure D13. Head distribution for Case 12. Black lines show the head contours, while the blue line indicates the water table. White arrows depict flow vectors (only a portion of vectors is shown).